

A Control-Theoretic Approach to Forced Response System Identification of Rocket Engine Turbopump Cavitation Dynamics

by

Mark Chang

B.S., University of California, San Diego (2017)

Submitted to the Department of Aeronautics and Astronautics
in partial fulfillment of the requirements for the degree of

Master of Science in Aeronautics and Astronautics

at the

MASSACHUSETTS INSTITUTE OF TECHNOLOGY

September 2020

© Massachusetts Institute of Technology 2020. All rights reserved.

Author
Department of Aeronautics and Astronautics
July 14, 2020

Certified by
Zoltán S. Spakovszky
Professor of Aeronautics and Astronautics
Thesis Supervisor

Accepted by
Zoltán S. Spakovszky
Professor of Aeronautics and Astronautics
Chairman, Graduate Program Committee

A Control-Theoretic Approach to Forced Response System Identification of Rocket Engine Turbopump Cavitation Dynamics

by

Mark Chang

Submitted to the Department of Aeronautics and Astronautics
on July 14, 2020, in partial fulfillment of the
requirements for the degree of
Master of Science in Aeronautics and Astronautics

Abstract

High performance turbopumps are used in many rocket propulsion systems to reduce the weight and cost of the system. However, to meet these weight conditions and the demands of the rocket engine, turbopumps must operate at high speeds and low inlet pressures. This can lead to cavitation in the turbopump inducer. There are several distinct types of cavitation dynamics. Of concern to this project is cavitation surge which are planar oscillations in the flow that occur at frequencies usually 0.1 - 0.3 times rotor frequency. Cavitation surge can cause the turbopump to modulate the mass flow into the rocket engine combustion chamber and thus yield variations in engine thrust. This in turn can lead to self excited fluid-structure oscillations and POGO instability which can result in mission failure. Characterization of the cavitating inducer dynamics is critical to the design of the propulsion system so as to guarantee sufficient stability margin.

This thesis introduces a control theoretic modeling framework that captures the free response cavitation dynamics of turbopump inducers. The reduced order framework was then used to guide the design of a forced response experiment. The design of experiment included the placement of sensors, a piston actuator, and an accumulator to ensure high signal to noise ratio and coherence. Forced response experiments were carried out to experimentally validate the model, and to characterize the cavitation surge dynamics. The experiments identified challenges with the test facility, specifically vibrations of the piping and support structure which induced large fluid perturbations. Due to time constraints and COVID-19, a second test was not possible. This thesis provides useful guidelines and best practices paving the way for future forced response system identification experiments.

Thesis Supervisor: Zoltán S. Spakovszky

Title: Professor of Aeronautics and Astronautics

Acknowledgments

Many people have provided me with the motivation, guidance, and support throughout this process. Firstly, I would like to thank my research advisor, Professor Zoltán Spakovszky, for the opportunity to study in the Gas Turbine Lab and to work on this project. I am grateful for the patience afforded to me so that I could fully grasp each of the countless lessons that I will carry on into my professional career.

This project would also not be possible without the financial and technical support of The Aerospace Corporation. I am grateful for the technical support of David Jackson, Andy Mulder, and Jay Schuille from our monthly telecons, and for the opportunity to perform an internship at the Aerospace Corporation in El Segundo.

I would like to thank Dr. Yu Wan for his support in this project. I appreciate how easy it was to talk to and work with, which had spurred many insightful technical discussions.

To my labmates in the Gas Turbine Lab, I am thankful for the friendship and support over my time spent at MIT. Special thanks to Kanika, Geoff, and Laurens. Our camaraderie together made many late night project cram sessions bearable. The numerous Celtics games with Jered and Manny made so many nights worth looking forward to and much more entertaining (Go Lakers!). Trang, your constant enthusiasm always never failed to give me a spike of energy. My friends in FGC Allen, Beldon, Faisal, Jon, Katie, Lena, Maya, and Regina, I am lucky to have so many amazing memories with you guys. But I have regret never making it to a game of block chain. My friends back home Jiarong, Edwin, Cody, Eric, David, and Stephanie, you guys are awesome. Your support and individual drives has helped and inspired me to succeed in my education.

Lastly and most importantly, I would like to thank my parents Michael and Betty, my brother Melvin, and my sister Amanda for their love and support. I would not have gotten to where I am now without it.

Contents

1	Introduction	27
1.1	Background and Motivation	27
1.1.1	Cavitation Instabilities in Inducers	28
1.2	Previous Work	29
1.2.1	Characterization of Cavitation Surge Dynamics	29
1.2.2	Control Theoretical System Identification Approach	31
1.3	Research Goals and Objectives	32
1.4	Thesis Contributions	32
2	Transmission Matrix Modeling	35
2.1	Lumped Parameter Model Derivation	36
2.2	Accumulator Model	40
2.3	Inducer Model	42
2.3.1	Lumped Parameter Inducer Model	42
2.3.2	1D Cavitation Surge Model	44
2.4	Transmission Matrix Stacking	46
2.5	Boundary Conditions	48
2.5.1	Open/Closed Boundary Conditions	48
2.5.2	Periodic Boundary Conditions	50
3	Experimental Analysis and Transmission Matrix Modeling of Cavi- tation Dynamics in the MIT Inducer	51
3.1	Free Response Test Experimental Setup	51

3.2	MIT Inducer	55
3.2.1	MIT Inducer Steady Performance	56
3.2.2	Cavitation Dynamics of The MIT Inducer	57
3.3	Free Response Model Implementation and Verification with Experimental Data	59
3.3.1	Fluid System Component Modeling and Stacking	59
3.3.2	Boundary Condition Selection	63
3.3.3	Modeling Framework Verification through Modification of C and M	65
4	Forced Response Modeling and Transfer Function Identification Methodology	71
4.1	Drive Point Impedance Modeling	71
4.2	Transfer Functions at Arbitrary Locations	74
4.2.1	Piston Actuator Located Upstream of Sensing Location	74
4.2.2	Piston Actuator Located Downstream of Sensing Location . .	75
4.3	Transfer Function and Transmission Matrix Identification	77
5	Model Based Design of Force Response Experiment	81
5.1	Sensor Locations	81
5.2	Example Forced Response Model Implementation	82
5.3	Perturbation Limits	86
5.4	Component Trade Studies	89
5.4.1	Effect of Piston Location on System Transfer Functions	90
5.4.2	Effect of Accumulator Location on System Transfer Functions	93
5.4.3	Effect of Accumulator Compliance on System Transfer Functions	97
5.4.4	Effect of Accumulator Resistance on System Transfer Functions	100
5.5	Recommended Design for Modified Inducer Test Facility	101
6	Cavitating Inducer Forced Response Testing	105
6.1	Forced Response Experimental Setup	105

6.1.1	Sensors	107
6.1.2	Accumulator Design	107
6.1.3	Piston Actuator	108
6.1.4	Forcing Signal	109
6.2	Analysis of Structural Modes	110
6.2.1	Analysis of Forced Response Transfer Functions	112
6.2.2	Analysis of Hammer Tap Test Frequency Response Functions .	114
6.3	Inducer Test Facility Design Guidelines	117
7	Conclusion	125
7.1	Summary	125
7.2	Recommendation for Future Work	126
A	Non-dimensional Compliances and Mass Flow Gain Factors	129
B	Inducer Model Selection	133
C	Transfer Function Bode Plots	139
C.1	Piston Location Trade Study	140
C.2	Accumulator Location Trade Study	142
C.3	Accumulator Compliance Trade Study	144
C.4	Accumulator Resistance Trade Study	147
C.5	Recommended Design	149
C.5.1	Low Cavitation Design	149
C.5.2	High Cavitation Design	151
D	Fiber Film Probe Calibration	153
E	Hammer Tap Test FRF and Modeshapes	157

List of Figures

1-1	Cavitation instability regimes of LE-7 [20]	29
2-1	Accumulator model	40
2-2	Cavitating semi-actuator disk model [23]	44
2-3	Compact duct model	46
2-4	Stacking of accumulator with compact upstream and downstream ducts	47
3-1	Aerospace Corporation's inducer test facility [6]	53
3-2	Schematic of inducer test facility [6]	54
3-3	Close up of inducer test section	55
3-4	MIT inducer test hardware	56
3-5	Measured non-cavitating performance and inferred stagnation pressure loss. Inset shows cavitation performance head loss curve at $\phi = 0.06$ [23]	57
3-6	Cavitation regimes along the inducer knee curve at $\phi = 0.083$ [13]	58
3-7	Time series data of cavitation surge (top) and spectrogram of cavitation surge data (bottom) of MIT inducer at $\phi = 0.06$ [10]	58
3-8	Schematic of inducer test facility	59
3-9	The root locus plots using the lumped parameter inducer model shows very similar estimates for the cavitation surge eigenvalues regardless of the boundary condition	63
3-10	The error percentage between the eigenvalues of the two boundary conditions when using the lumped parameter inducer model is small, indicating that the open-open boundary condition is an appropriate approximation	64

3-11	The root locus plots using the 1D cavitation surge model shows very similar estimates for the cavitation surge eigenvalues regardless of the boundary condition condition	65
3-12	The error percentage between the eigenvalues of the two boundary conditions when using the 1D cavitation surge model is small, indicating that the open-open boundary condition is an appropriate approximation	65
3-13	Cavitation surge frequency model estimation using unmodified CFD C and M does not match measured cavitation surge frequency	67
3-14	Stability trend estimation using unmodified CFD C and M does not match observed stability trend	68
3-15	Cavitation surge frequency model estimation using modified CFD C and M matches measured cavitation surge frequency	69
3-16	Stability trend estimation using modified CFD C and M more closely matches observed stability trend	69
4-1	Schematic of system with arbitrary pulser location	73
4-2	Schematic of a system with pulser located upstream of the desired transfer function location, m . Duct M and station m are located within duct B	74
4-3	Schematic of a system with pulser located downstream of the desired transfer function location, m . Duct M and station m are located within duct A	76
4-4	Schematic of inducer and sensors	78
4-5	Open loop block diagram for system transfer functions	78
5-1	Pressure transducer and fiber film probe locations around the inducer	82
5-2	Schematic for forced response derivation	83
5-3	Velocity measurement captured with a single fiber film probe compared to normalized optical mass flow rate shows good matching between the two sensors [19]	88
5-4	Raw and filtered cavitation surge velocity captured with fiber film probe	88

5-5	Power spectral density plots of raw and filtered cavitation surge velocity data shows surge dynamics were filtered out of fiber film data . .	89
5-6	Cartoon of desired transfer function bode plots: Pressure (left) and Velocity (right)	90
5-7	Weight of the piston requires its placement location to depend on mounting availability on optics table. The lighter weight of the accumulator allows for its larger placement area.	91
5-8	Schematics for piston location trade study: Piston upstream of inducer (right), Piston downstream of inducer (left)	92
5-9	Comparison of upstream pressure transfer function, at $\phi = 0.06$ and $\sigma = 0.03$, shows when piston is placed upstream of inducer, larger magnitude responses are found. Piston placed downstream of inducer (right), Piston placed upstream of inducer (left)	93
5-10	Schematic showing accumulator locations for different possible configurations	94
5-11	Comparison of upstream pressure transfer function, at $\phi = 0.06$ and $\sigma = 0.03$, shows when accumulator is placed near the inducer, the two modes overlap. Placing the accumulator downstream of the piston and inducer results in smaller perturbation magnitudes	96
5-12	Cartoon showing that as piston is moved closer to the accumulator, the zero moves away from the accumulator peak resulting in a larger magnitude	96
5-13	Schematic for accumulator compliance and resistance trade study . .	97
5-14	Accumulator mode natural frequency is inversely proportional to the accumulator compliance: upstream pressure transfer function, $\sigma = 0.03$, $\phi = 0.06$	98
5-15	Cartoon showing that as accumulator volume increases, the accumulator peak moves to lower frequency and the cavitation surge frequency increases in magnitude	99

5-16	Accumulator mode is tuned to similar frequency as inducer cavitation surge mode. The poles are difficult to identify from each other: upstream pressure transfer function, $\sigma = 0.03$, $\phi = 0.06$, $C_{accum} = 2.1$. .	100
5-17	Accumulator resistance, unless nearing the resistance levels of the porous media valve, has little effect on the upstream pressure perturbation transfer function: $\sigma = 0.03$, $\phi = 0.06$, $C_{accum} = 3$	101
5-18	Schematic for recommended modification for inducer test facility . . .	103
5-19	Bode plots of upstream pressure (left) and velocity (right) perturbation transfer functions are within perturbation limits: Recommended configuration of inducer test facility for low cavitation number flows, $\sigma = 0.03 - 0.04$, $\phi = 0.06$	103
5-20	Bode plots of upstream pressure (left) and velocity (right) perturbation transfer functions are within perturbation limits: Recommended configuration of inducer test facility for high cavitation number flows, $\sigma = 0.04 - 0.1$, $\phi = 0.06$	104
6-1	Inducer test facility modified with gas accumulator, stainless steel bellows, piston actuator, and PVC ducting	106
6-2	Schematic of Inducer Test Facility modified with Piston Actuator p_2 , PVC ducting p_3 , Gas Accumulator p_4 , and Stainless Steel Bellows p_5 .	106
6-3	Cartoon of Accumulator Design	108
6-4	Cross section of piston assembly [8]	109
6-5	Pressure transfer function overlaid with hammer tap test data shows similar resonant frequencies. Confirms that the forced response test can measured the structural dynamics of the test facility	111
6-6	Similar measured upstream pressure transfer functions regardless of flow condition indicated that the mode shape is heavily influenced by the structural dynamics: No Flow, static inducer (left); Inducer running at $\phi = 0.06$, $\sigma = 0.05$ (right)	113

6-7	The addition of accumulator compliance did not add a peak, but had shifted the anti-resonance: No Flow, static inducer (left); Inducer running at $\phi = 0.06, \sigma = 0.1$ (right)	114
6-8	Hammer and sensor locations of the hammer tap tests	115
6-9	Both the sensor averaged FRF and overlaid sensor FRFs shows resonant frequencies at 0.05 rotor frequency. Hammer tap location at inducer housing-stainless steel pipe flange	118
6-10	The 0.05 rotor frequency mode shape is generated by obtaining the magnitude of the imaginary portion of the FRF at each sensor location. Each location has the same magnitude and phase.	119
6-11	Measured mode shape overlaid a cartoon of test facility indicated that the 0.05 rotor frequency is caused by the optics table pitch motion . .	119
6-12	The sensor averaged FRF and overlaid sensor FRFs shows resonant frequencies at 0.18, 0.22, 0.38, 0.44, 0.47, 0.50, 0.56 rotor frequency. Hammer location at bellows-accumulator flange	120
6-13	The 0.18 rotor frequency mode shape is generated by obtaining the magnitude of the imaginary portion of the FRF at each sensor location	121
6-14	Measured mode shape overlaid a cartoon of test facility indicated that the 0.18 rotor frequency is a rigid body mode allowed by the flexibility of the bellows	121
6-15	The 0.22 rotor frequency mode shape is generated by obtaining the magnitude of the imaginary portion of the FRF at each sensor location	122
6-16	Measured mode shape overlaid a cartoon of test facility indicated that the 0.22 rotor frequency is a bending mode of the ducting	122
6-17	Fixed support at center of stainless steel pipe corresponds to node in mode shape	123
6-18	The 0.44 rotor frequency mode shape is generated by obtaining the magnitude of the imaginary portion of the FRF at each sensor location	124

6-19	Measured mode shape overlaid a cartoon of test facility indicated that the 0.44 rotor frequency mode is a result of the flexibility of the bellows and accumulator tee support structure	124
A-1	Non-dimensional compliance of storage tank	130
A-2	Non-dimensional compliance of inducer from CFD [10]	130
A-3	Non-dimensional mass flow gain factor of inducer from CFD [10] . . .	131
B-1	Cavitation surge frequency found using the lumped parameter inducer model and the 1D cavitation surge model and CFD derived C and M bound the measured cavitation surge frequency	135
B-2	Neither the lumped parameter model nor the 1D cavitation surge model matched the observed stability behavior. The critical damping percentage is shown; CFD Derived C and M is used	136
B-3	Modifications to the CFD derived C and M yielded simulated frequency content that matched the observed behavior	136
B-4	Modifications to the CFD derived C and M yielded simulated stability trends that matched the observed behavior	137
C-1	Comparison of upstream velocity transfer function, at $\phi = 0.06$ and $\sigma = 0.03$, shows when piston is placed upstream of inducer, larger magnitude responses are found. Piston placed downstream of inducer (right), Piston placed upstream of inducer (left)	140
C-2	Comparison of downstream pressure transfer function, at $\phi = 0.06$ and $\sigma = 0.03$, shows when piston is placed upstream of inducer, larger magnitude responses are found. Piston placed downstream of inducer (right), Piston placed upstream of inducer (left)	141
C-3	Comparison of downstream velocity transfer function, at $\phi = 0.06$ and $\sigma = 0.03$, shows when piston is placed upstream of inducer, larger magnitude responses are found. Piston placed downstream of inducer (right), Piston placed upstream of inducer (left)	141

C-4	Comparison of upstream velocity transfer function, at $\phi = 0.06$ and $\sigma = 0.03$, shows when accumulator is placed near the inducer, the two modes overlap. Placing the accumulator downstream of the piston and inducer results in desired smaller perturbation magnitudes	142
C-5	Comparison of downstream pressure transfer function, at $\phi = 0.06$ and $\sigma = 0.03$, shows when accumulator is placed near the inducer, the two modes overlap. Placing the accumulator downstream of the piston and inducer results in desired smaller perturbation magnitudes	143
C-6	Comparison of downstream velocity transfer function, at $\phi = 0.06$ and $\sigma = 0.03$, shows when accumulator is placed near the inducer, the two modes overlap. Placing the accumulator downstream of the piston and inducer results in desired smaller perturbation magnitudes	143
C-7	Accumulator mode natural frequency is inversely proportional to the accumulator compliance: upstream velocity transfer function, $\sigma = 0.03$, $\phi = 0.06$	144
C-8	Accumulator mode natural frequency is inversely proportional to the accumulator compliance: downstream pressure transfer function, $\sigma = 0.03$, $\phi = 0.06$	144
C-9	Accumulator mode natural frequency is inversely proportional to the accumulator compliance: downstream velocity transfer function, $\sigma = 0.03$, $\phi = 0.06$	145
C-10	Accumulator mode is tuned to similar frequency as inducer cavitation surge mode. The poles are difficult to identify from each other: upstream pressure transfer function, $\sigma = 0.03$, $\phi = 0.06$, $C_{accum} = 2.1$. .	145
C-11	Accumulator mode is tuned to similar frequency as inducer cavitation surge mode. The poles are difficult to identify from each other: upstream pressure transfer function, $\sigma = 0.03$, $\phi = 0.06$, $C_{accum} = 2.1$. .	146
C-12	Accumulator mode is tuned to similar frequency as inducer cavitation surge mode. The poles are difficult to identify from each other: upstream pressure transfer function, $\sigma = 0.03$, $\phi = 0.06$, $C_{accum} = 2.1$. .	146

C-13	Accumulator resistance, unless nearing the resistance levels of the porous media valve, has little effect on the upstream velocity perturbation transfer function: $\sigma = 0.03$, $\phi = 0.06$, $C_{accum} = 3$	147
C-14	Accumulator resistance, unless nearing the resistance levels of the porous media valve, has little effect on the downstream pressure perturbation transfer function: $\sigma = 0.03$, $\phi = 0.06$, $C_{accum} = 3$	147
C-15	Accumulator resistance, unless nearing the resistance levels of the porous media valve, has little effect on the downstream velocity perturbation transfer function: $\sigma = 0.03$, $\phi = 0.06$, $C_{accum} = 3$	148
C-16	Bode plots of upstream velocity perturbation transfer functions: Recommended configuration of inducer test facility for low cavitation number flows	149
C-17	Bode plots of downstream pressure perturbation transfer functions: Recommended configuration of inducer test facility for low cavitation number flows	149
C-18	Bode plots of downstream velocity perturbation transfer functions: Recommended configuration of inducer test facility for low cavitation number flows	150
C-19	Bode plots of upstream velocity perturbation transfer functions: Recommended configuration of inducer test facility for high cavitation number flows	151
C-20	Bode plots of downstream pressure perturbation transfer functions: Recommended configuration of inducer test facility for high cavitation number flows	151
C-21	Bode plots of downstream velocity perturbation transfer functions: Recommended configuration of inducer test facility for high cavitation number flows	152
E-1	The 0.38 rotor frequency mode shape is generated by obtaining the magnitude of the imaginary portion of the FRF at each sensor location	158

E-2	Measured mode shape overlaid a cartoon of test facility indicated that the 0.38 rotor frequency mode is a result of the flexibility of the bellows and accumulator tee support structure	159
E-3	The 0.47 rotor frequency mode shape is generated by obtaining the magnitude of the imaginary portion of the FRF at each sensor location	159
E-4	Measured mode shape overlaid a cartoon of test facility indicated that the 0.47 rotor frequency mode is a result of the flexibility of the bellows and accumulator tee support structure	160
E-5	The 0.56 rotor frequency mode shape is generated by obtaining the magnitude of the imaginary portion of the FRF at each sensor location	161
E-6	Measured mode shape overlaid a cartoon of test facility indicated that the 0.56 rotor frequency mode is a result of the flexibility of the bellows and accumulator tee support structure	162

List of Tables

3.1	Dimensions of MIT Inducer	55
3.2	Inducer test facility components and non-dimensional resistances and inertances	61
3.3	Modified Cavitation Compliance and Mass Flow Gain Factor	66
5.1	Inducer Test Facility Components and Non-Dimensional Resistances and Inertances for Example Forced Response Model Implementation .	84
B.1	Modified Cavitation Compliance and Mass Flow Gain Factor for Lumped Parameter and 1D Cavitation Surge Models	134

Nomenclature

Acronyms

FRF	frequency response function
LPOP	low pressure oxidizer pump
MIT	Massachusetts Institute of Technology
NASA	National Aeronautics and Space Administration
SSME	Space Shuttle main engines

Greek Symbols

α	thermal diffusivity, incidence angle
β	flow angle
γ	ratio of specific heats
ω	inducer rotation rate, oscillation frequency
ϕ	flow coefficient
ψ	head rise coefficient
ρ	density
σ	cavitation number, growth rate
Σ	thermal parameter

τ non-dimensional time, time lag

θ circumferential angle

Roman Symbols

a speed of sound

$A, [A]$ area, transmission matrix

AR area ratio

$[B]$ transmission matrix

C non-dimensional compliance

c input signal

c_p specific heat at constant pressure

DB thermodynamic bubble growth parameter

\dot{f} linear chirp ramp rate

G non-dimensional pump gain, cavitation dynamics

h_f heat of formation

j imaginary unit, $j = \sqrt{-1}$

k spatial wavelength

L non-dimensional inertance

l device length

L_{cav} non-dimensional headloss due to cavitation

L_{ind} non-dimensional inducer headloss

\dot{m} dimensional mass flow rate

$M, [M]$	non-dimensional mass flow gain factor, transmission matrix
n	n-th spatial harmonic
P, p	non-dimensional and dimensional pressure
Q	volumetric flow rate
R	non-dimensional resistance
r_T	tip radius
s	non-dimensional Laplace variable, $s = \sigma + j\omega$
t	time
$T, [T]$	temperature, transmission matrix
U, u	non-dimensional and dimensional velocity
V	volume
x, \vec{x}	axial location, state vector
y	output signal
z	impedance
Z_c	characteristic impedance

Subscript and Superscripts

*	dimensional
1	inlet
2	outlet
-	steady
~	unsteady

C	cavitation
dn	downstream
g	gas
L	per unit length
l	liquid
p	piston
up	upstream

Chapter 1

Introduction

1.1 Background and Motivation

Many of the rocket engine assemblies used today in the space launch industry are turbopump fed systems. The advantage of using turbopump fed systems is that they are capable of delivering high pressure propellants to the rocket engine with a small mass impact relative to the vehicle weight. These systems are able to achieve these results because of the low tank pressures and the high pressure rise from the pumps. However, low inlet static pressure and high rotational speeds establish a regime where cavitation is prevalent. This causes the formation and collapse of gas bubbles which can cause immense structural damage in the pumps. To combat this pump designers have decided to provide an initial static pressure rise by placing a cavitating inducer just upstream of the pump impeller. As a result this limits the cavitation to just the inducer. However, it is critical to design the inducer, so as to ensure that under cavitating conditions, it will tolerate the structural stresses, provide the necessary head rise, and most importantly does not destabilize the overall system.

The major concern is pogo instability. Pogo instability is a self excited oscillation cycle where thrust variations from the propulsion system induce longitudinal vibrations of the vehicle which, through feedback, can lead to instability. This instability can cause structural failures that lead to mission failure for example with the Gemini missions and Titan II [4]. Less severe pogo was also observed in the Apollo missions.

In order to control these instabilities, costly pogo suppression devices, such as accumulators, are typically added to the propulsion system after the fact. To date these issues still persist and are an emphasis in the design process with the Constellation program which was superseded by the Space Shuttle program and then the Artemis program [12].

The characterization of the cavitation dynamics in turbopump inducers is critical during the component design and test process, but current techniques to characterize cavitating inducer dynamics require sophisticated forced response test rigs. Techniques to experimentally assess the dynamics have not changed much since the pioneering work of Caltech in the 70's [3] and only limited data has been collected since that time.

1.1.1 Cavitation Instabilities in Inducers

There are several types of cavitation instabilities each of which depend on the inducer geometry and inlet flow conditions, notably flow coefficient, ϕ , and cavitation number, σ . The different types of instabilities for the LE-7 turbopump inducer can be seen in Figure 1-1. The main instabilities of interest here are cavitation surge, and rotating cavitation.

Rotating cavitation is a local instability caused when the inducer is required to operate at low cavitation numbers. This phenomena appears similar to rotating stall as rotating cavitation has a bubble cavity(s) propagate from blade to blade circumferentially like the stall cell of rotating stall. A key difference is that rotating cavitation is normally supersynchronous to the rotor speed where as rotating stall is subsynchronous. [1]

Cavitation surge, referenced as auto oscillation in literature and the main focus of this thesis, is a system level instability that produces large planar oscillations in pressure and flow rate. This instability is characterized by large regions of backflow which drive the oscillations. Cavitation surge is similar to compressor surge in aero-engines except that the compliance is due to the compressibility of the vapor cavities. However, unlike surge, the cavitation surge frequency is usually dependent on the

rotor frequency usually between 0.1 - 0.3 rotor frequency [1].

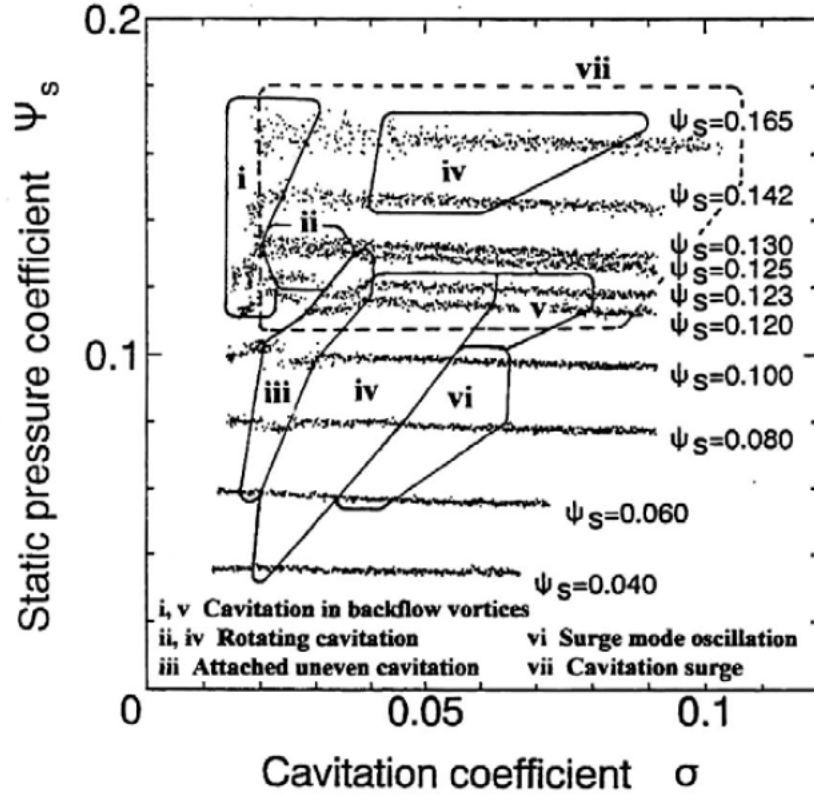


Figure 1-1: Cavitation instability regimes of LE-7 [20]

1.2 Previous Work

1.2.1 Characterization of Cavitation Surge Dynamics

The very first characterization of cavitation dynamics was done so with one-dimensional approximations of the governing equations. Rubin expressed these equations with the lumped parameters inertance, L , resistance, R , pressure gain, G , and cavitation compliance, C [16]. Brennen expanded on this by finding that another key parameter, the mass flow gain factor, M , in addition to cavitation compliance was needed to properly characterize the changing cavitation void volume [2]. The dynamics of the inducer were formulated in the form of a transmission matrix where the elements of the matrix, and the state vectors are all complex values as shown in Eq. (1.1).

$$\begin{bmatrix} \tilde{p}_2 \\ \tilde{u}_2 \end{bmatrix} = \begin{bmatrix} T_{11} & T_{12} \\ T_{21} & T_{22} \end{bmatrix} \begin{bmatrix} \tilde{p}_1 \\ \tilde{u}_1 \end{bmatrix} \quad (1.1)$$

Tsujimoto then built on this, expanding it to model rotating cavitation by extending a non-cavitating semi-actuator disk model with a blade cavitation [22]. He showed that rotating cavitation and rotating stall were different phenomena, and confirmed the existence of forward and backward rotating cavitation. Tsujimoto then merged his two-dimensional cavitating semi-actuator disk model with the one-dimensional modeling theory and created a unified treatment of flow instabilities that defined the instability onset criteria and oscillation frequency of surge, cavitation surge, rotating stall, and rotating cavitation in terms of cavitation compliance and mass flow gain factor [21]. However, the learnings from his unified treatment is of little practical use unless more information on C and M as a function of inlet conditions is available.

C and M can be identified from forced response experiments. These are generally conducted by introducing mass flow fluctuations near the inducer using actuators such as siren valves [3] or piston pulsers, which are used in this thesis. To date, however, there is limited experimental data on the characterization of inducer cavitation dynamics and the work by Brennen et al. at Caltech in the 70s and 80s remains standalone in this regard. As such the state of the art experimental techniques have not changed much since the first experiments were conducted decades ago. Currently, the unsteady upstream and downstream pressure and flow response to the mass flow fluctuations are used to determine the 4 transmission matrix elements. However to do so, this characterization method required at least two sets of linearly independent data sets to determine the 4 complex transmission matrix coefficients. To achieve this, multiple actuators at different locations in the flow loop were pulsed at different magnitudes [3]. These sets of data were then least squares fitted to solve for the transmission matrix coefficients.

Another challenge of these experiments was the dynamic sensing of the mass flow. Early tests by Brennen utilized Laser Doppler Velocimetry (LDV) and later on switched to electromagnetic flow meters to obtain more reliable measurements and

better signal to noise properties. However, the limitation with using these devices is that it restricts the data to only provide insight of one-dimensional oscillations. Though sufficient for characterization of cavitation surge, higher order instabilities cannot be identified. This thesis looks to solve this issue by using fiber film probes, as they are capable of measuring unsteady velocity and are compact enough to be arranged in an array similar in fashion to the pressure transducers used to characterize rotation cavitation and alternate blade cavitation by Lettieri et al. [13].

More recent studies aimed at characterization of C and M were conducted using steady CFD. These properties were found in four bladed inducers at temperatures where thermal suppression effects were dominant [10]. The measured fluid modes were in agreement with the natural frequencies derived the compliance and inline feed system inertance.

1.2.2 Control Theoretical System Identification Approach

While the prior work has provided much insight into the characterization and identification of cavitation dynamics, there is still a need for new experimental data and a simpler approach for determining cavitation dynamics of inducers. Advancements in the identification and control of aero-engine instability can be borrowed in order to determine inducer cavitation dynamics [18]. These advancements present a new approach in forced response testing that utilizes a control theoretical system identification methodology. With knowledge of the system input signal (i.e. piston mass flow/velocity fluctuation), a single set of dynamic measurements, the upstream and downstream pressure and velocity, can be used to determine the 4 transfer functions and the 4 transmission matrix elements.

Each transfer function is the frequency response function of the pressure/velocity measurement to the input signal. The key benefit of transfer functions is that they contain pole-zero information that corresponds to dynamics of the compliance elements (i.e. accumulators, cavitation voids) in the system. They also serve as a mathematical intermediary point to determining the inducer transmission matrix. The 4 transfer functions are determined via spectral analysis and subsequently cast

as a transmission matrix in the form of Eq. (1.1).

1.3 Research Goals and Objectives

The overall goal of this research is to demonstrate the control theoretical system identification method can characterize the cavitation surge dynamics of an inducer with reduced complexity and improved reliability. The objectives are to:

- Leverage off previously developed reduced order models to create a framework that captures the measured free response cavitation dynamics of the MIT inducer
- Modify the reduced order model to create a control theoretical forced response framework to guide the modification of an inducer test facility for forced response testing and design of experiment
- Demonstrate the feasibility of fiber film probes to measure unsteady velocity fluctuations
- Determine the system transfer functions using the unsteady pressure and velocity response, and the input velocity fluctuation
- Extract the transmission matrix and its lumped parameters (pressure gain, impedance, compliance and mass flow gain factor) from the measured transfer functions to characterize the cavitation dynamics.

1.4 Thesis Contributions

This thesis attempted to assess the dynamics of the MIT inducer, but was unable to due to unanticipated fluid-structural dynamics overpowering the cavitation dynamics. The assessment of the structural excitation during the forced response experiments extended the timeline of the project and due to COVID-19 a second test entry was not possible. However, the analysis of these issues lead to valuable guidelines and lessons

learned on the design of forced response inducer test facilities. From a modeling perspective, this thesis introduces a free response reduced order transmission matrix modeling framework that accurately simulates the cavitation dynamics of the MIT inducer. The free response model was validated with experimental data and then extended into a forced response modeling framework. This methodology was used to determine the necessary modifications to the inducer test facility for forced response testing.

Chapter 2

Transmission Matrix Modeling

The first models for characterization of turbopump cavitation dynamics were developed by Brennen [2]. These models were based on reduced order, linearized, one-dimensional transmission matrices requiring the calculation of two key parameters, the cavitation compliance, and the mass flow gain factor. Tsujimoto et al. extended this work by using two dimensional actuator disk theory to propose a unified treatment of flow instabilities [21]. This methodology provided much insight into the onset of surge, cavitation surge, rotating stall, and rotating cavitation. However, this modeling approach lacks flexibility with different pumping configurations because if components are added or removed the entire governing equations need to be rewritten. As such a reduced order transmission matrix modeling framework similar to the one initially developed by Brennen [2] and Rubin [17] was chosen in the present research.

This chapter introduces the modeling framework for an axial duct and a gas accumulator as done in [14], and two different modeling frameworks for cavitating inducers as done in [17, 23]. Then it is demonstrated how these models are combined with boundary conditions to create an eigenvalue problem for the dynamics of the fluid system.

The modeling assumptions are as follows:

- Flow is one dimensional and inviscid outside of the inducer

- Effects of heat transfer are neglected
- Reynolds number effects are neglected
- Flow properties can be decomposed into a steady part and small unsteady perturbations, for example $u(x, t) = \bar{u}(x, t) + \tilde{u}(x, t)$

2.1 Lumped Parameter Model Derivation

The governing equations for a one dimensional inviscid compressible flow through a constant area duct can be represented as follows:

$$\begin{aligned} \frac{\partial \rho}{\partial t} + \frac{\partial(\rho u)}{\partial x} &= 0 \\ \rho \frac{\partial u}{\partial t} + \rho \frac{\partial u^2}{\partial x} + \frac{\partial p}{\partial x} - R_L^* A u &= 0 \end{aligned} \quad (2.1)$$

where R_L^* is the resistance per unit length of the element, A is the area of the duct, ρ is the density of the fluid, p is the pressure and u is the axial velocity.

Decomposing the pressure and velocity into a steady ($\bar{}$) and a small amplitude unsteady perturbation ($\tilde{}$) yields:

$$\begin{aligned} p &= \bar{p} + \tilde{p} \\ u &= \bar{u} + \tilde{u}. \end{aligned} \quad (2.2)$$

Neglecting higher order terms, the linearized governing equations are:

$$\begin{aligned} \frac{\partial \tilde{\rho}}{\partial t} + \bar{u} \frac{\partial \tilde{\rho}}{\partial x} + \bar{\rho} \frac{\partial \tilde{u}}{\partial x} &= 0 \\ \bar{\rho} \frac{\partial \tilde{u}}{\partial t} + \frac{\partial \tilde{p}}{\partial x} - R_L^* A \tilde{u} &= 0 \end{aligned} \quad (2.3)$$

The change in pressure and density can be related using the speed of sound, \bar{a}

$$\bar{a} = \sqrt{\left. \frac{\tilde{p}}{\tilde{\rho}} \right|_s}. \quad (2.4)$$

Assuming that the mean flow velocity, \bar{u} is small compared to the speed of sound, the linearized governing equations can be rewritten as

$$\begin{aligned} \frac{1}{\bar{\rho}\bar{a}^2} \frac{\partial \tilde{p}}{\partial t} + \frac{\partial \tilde{u}}{\partial x} &= 0 \\ \frac{\bar{\rho}}{A} \frac{\partial \tilde{u}}{\partial t} + \frac{1}{A} \frac{\partial \tilde{p}}{\partial x} - R_L^* \tilde{u} &= 0. \end{aligned} \quad (2.5)$$

From here it is beneficial to define the compliance, C_L^* , and the inertance, L_L^* , of the duct (per unit length).

$$\begin{aligned} C_L^* &= \frac{1}{\bar{\rho}\bar{a}^2} \\ L_L^* &= \frac{\bar{\rho}}{A} \end{aligned} \quad (2.6)$$

Combining these definitions with the spatial derivative of the momentum equation and the time derivative of the continuity equation results in the linear wave equation in terms of only velocity or pressure.

$$\begin{aligned} L_L^* C_L^* \frac{\partial^2 \tilde{p}}{\partial t^2} - \frac{\partial^2 \tilde{p}}{\partial x^2} + R_L^* C_L^* \frac{\partial p}{\partial t} &= 0 \\ L_L^* C_L^* \frac{\partial^2 \tilde{u}}{\partial t^2} - \frac{\partial^2 \tilde{u}}{\partial x^2} + R_L^* C_L^* \frac{\partial u}{\partial t} &= 0 \end{aligned} \quad (2.7)$$

Here the linear wave equations in Eq. (2.7) will be non-dimensionalized by scaling with the inducer tip velocity, inducer tip dynamic head, inducer tip radius and inducer angular velocity per Eqs (2.8)

$$\begin{aligned} U &= \frac{u}{\omega r_T} \\ P &= \frac{p - p_0}{\frac{1}{2} \rho_p (\omega r_T)^2} \\ X &= \frac{x}{r_T} \\ \tau &= t\omega \end{aligned} \quad (2.8)$$

where p_0 is a reference pressure, ω is the inducer rotational speed, r_T is the tip radius,

and ρ_p is the fluid density. The non-dimensional wave equation is

$$\begin{aligned} L_L C_L \frac{\partial^2 \tilde{P}}{\partial \tau^2} - \frac{\partial^2 \tilde{P}}{\partial X^2} + R_L C_L \frac{\partial \tilde{P}}{\partial \tau} &= 0 \\ L_L C_L \frac{\partial^2 \tilde{U}}{\partial \tau^2} - \frac{\partial^2 \tilde{U}}{\partial X^2} + R_L C_L \frac{\partial \tilde{U}}{\partial \tau} &= 0 \end{aligned} \quad (2.9)$$

where C_L, R_L, L_L are the non-dimensional compliance, resistance and inertance respectively.

$$\begin{aligned} R_L &= \frac{2}{\rho_p(\omega r_T)} R_L^* \\ L_L &= \frac{2\bar{\rho}A}{\rho_p(\omega r_T)} L_L^* \\ C_L &= \frac{1}{2}\rho_p(\omega r_T)^2 C_L^* \end{aligned} \quad (2.10)$$

Eqs (2.9) are solved in the frequency domain, by applying the Laplace transform and the Laplace variable, $s = \sigma + j\omega$

$$F(s) = \mathcal{L}\{f(t)\} = \int_0^\infty f(\tau) e^{-s\tau} d\tau. \quad (2.11)$$

The solution to the wave equation yields

$$\begin{aligned} \tilde{P}(X, s) &= C_1 e^{kX} + C_2 e^{-kX} \\ \tilde{U}(X, s) &= Z_c (C_1 e^{kX} + C_2 e^{-kX}) \end{aligned} \quad (2.12)$$

where C_1 and C_2 are constants, Z_c is the characteristic impedance, and k is the wave number or spatial frequency of the oscillations.

$$k^2 = C_L s (L_L s + R_L) \quad (2.13)$$

$$Z_c = \frac{C_L s}{k} \quad (2.14)$$

If an initial state at $X = 0$ for pressure and velocity to be $\tilde{P} = \tilde{P}_1$ and $\tilde{U} = \tilde{U}_1$ then

the constants C_1 and C_2 can be found and the solution becomes:

$$\begin{aligned}\tilde{P}(X, s) &= \frac{1}{2}(e^{kX} + e^{-kX})\tilde{P}_1 - Z_c \frac{1}{2}(e^{kX} - e^{-kX})\tilde{U}_1 \\ \tilde{U}(X, s) &= -\frac{1}{2Z_c}(e^{kX} - e^{-kX})\tilde{P}_1 + \frac{1}{2}(e^{kX} + e^{-kX})\tilde{U}_1\end{aligned}\tag{2.15}$$

Rewriting the solution in terms of hyperbolic sine and cosine functions and in matrix notation yields

$$\begin{bmatrix} \tilde{P}(X) \\ \tilde{U}(X) \end{bmatrix} = \begin{bmatrix} \cosh(kX) & -Z_c \sinh(kX) \\ -\frac{1}{Z_c} \sinh(kX) & \cosh(kX) \end{bmatrix} \begin{bmatrix} \tilde{P}_1 \\ \tilde{U}_1 \end{bmatrix}.\tag{2.16}$$

Eq. (2.16) represents a distributed element, however, not all elements (i.e. valves/ accumulators/ short ducts) need to be modeled as distributed systems. A useful simplification can be made when the element is acoustically compact. A device is compact when the wavelength of the flow oscillations, $1/k$, is much larger than the length, l of the device, $kl \ll 1$ allowing for the use of a Taylor series to approximate the hyperbolic sine and hyperbolic cosine terms.

$$\begin{bmatrix} \tilde{P}_2 \\ \tilde{U}_2 \end{bmatrix} = \begin{bmatrix} 1 & -Z_c kl \\ -\frac{kl}{Z_c} & 1 \end{bmatrix} \begin{bmatrix} \tilde{P}_1 \\ \tilde{U}_1 \end{bmatrix}.\tag{2.17}$$

Using the definition of the wave number, characteristic impedance, and converting the per unit resistance, compliance, and inertance to bulk values yields the lumped transmission matrix.

$$\begin{bmatrix} \tilde{P}_2 \\ \tilde{U}_2 \end{bmatrix} = \begin{bmatrix} 1 & -(R + sL) \\ -sC & 1 \end{bmatrix} \begin{bmatrix} \tilde{P}_1 \\ \tilde{U}_1 \end{bmatrix}\tag{2.18}$$

If the fluid is incompressible the non-dimensional governing equations for a constant area element simplifies to

$$\begin{aligned}\tilde{U}_2 &= \tilde{U}_1 \\ \tilde{P}_2 &= \tilde{P}_1 - L \frac{\partial \tilde{U}}{\partial \tau} - R \tilde{U},\end{aligned}\tag{2.19}$$

and the transmission matrix for the compact rigid duct with incompressible flow simplifies to

$$\begin{bmatrix} \tilde{P}_2 \\ \tilde{U}_2 \end{bmatrix} = \begin{bmatrix} 1 & -(R + sL) \\ 0 & 1 \end{bmatrix} \begin{bmatrix} \tilde{P}_1 \\ \tilde{U}_1 \end{bmatrix} \quad (2.20)$$

2.2 Accumulator Model

Accumulators are capacitive devices typically characterized by a large volume. For liquid fluid systems gas accumulators are used to provide compliance into the system. Consider the gas accumulators shown in Figure 2-1.

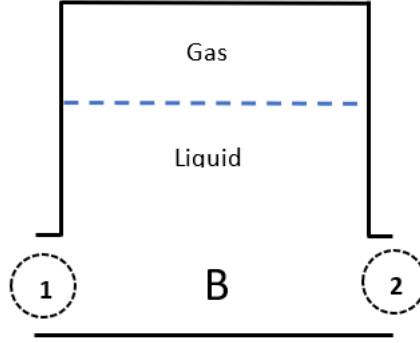


Figure 2-1: Accumulator model

Because of the large volume of the accumulator, the pressure is uniform between the inlet and exit.

$$\tilde{p}_1 = \tilde{p}_2 \quad (2.21)$$

The compliance of the accumulator can be found by conservation of mass across the device, represented dimensionally by

$$\dot{m}_1 - \dot{m}_2 = \frac{\partial(\rho_l V_l^*)}{\partial t} \quad (2.22)$$

where ρ_l denotes the liquid density and V_l^* denotes the dimensional liquid volume. The liquid is incompressible, and the inlet and exit area are assumed to be equal, so

the continuity equation can be reduced to

$$u_1 - u_2 = -\frac{1}{A} \frac{\partial V_g^*}{\partial t}, \quad (2.23)$$

where V_g^* refers to the dimensional gas volume of the accumulator, and A is the area of the inlet or exit. Linearizing the continuity equation and rewriting in terms of pressure yields

$$\tilde{u}_1 - \tilde{u}_2 = \frac{V_g^*}{A\gamma p_g} \frac{\partial \tilde{p}}{\partial t}. \quad (2.24)$$

Taking the Laplace transform of this results in

$$\tilde{u}_2 = -C_{accum}^* s \tilde{p}_1 + \tilde{u}_1 \quad (2.25)$$

where the dimensional compliance of the accumulator is

$$C_{accum}^* = \frac{V_g^*}{A\gamma p_g}. \quad (2.26)$$

Using the the ideal gas law the the compliance can also be written as:

$$C_{accum}^* = \frac{V_g^*}{A\rho_g c_g^2}. \quad (2.27)$$

Non-dimensionalizing the continuity equation results in the following transmission matrix

$$\begin{bmatrix} \tilde{P}_2 \\ \tilde{U}_2 \end{bmatrix} = \begin{bmatrix} 1 & 0 \\ -sC_{accum} & 1 \end{bmatrix} \begin{bmatrix} \tilde{P}_1 \\ \tilde{U}_1 \end{bmatrix}, \quad (2.28)$$

where the non-dimensional compliance is

$$C_{accum} = \frac{1}{2} \rho_p \omega^2 r_T C_{accum}^*. \quad (2.29)$$

The derivation of Eqs (2.28) shows that the dynamics of the accumulator is controlled solely by the compliance. This is because the model assumes no inertance or resistance due to the accumulator generally being short in length, and generally not

having mechanisms that introduce losses to the flow. This model also shows that the compliance is inversely proportional to pressure, which indicates that low cavitation tests could cause difficulty with precise control of the accumulator compliance.

2.3 Inducer Model

Modeling inducers is challenging because the resistance and inertance are functions of frequency, and the compliance of the inducers is a function of the inlet flow conditions. As such multiple approaches for modeling cavitating inducer dynamics have been developed in the past. The research conducted in this thesis considered two different inducer models. The first is a lumped parameter model that has been used since the 1960's for pogo stability analysis [17]. This thesis will refer to this model as the lumped parameter inducer model. The second inducer model has been recently introduced and is based on an analytical model derived from a semi-actuator disk representation extended with a blade cavity model [23]. This thesis will refer to this model as the 1D cavitation surge model.

The inducer used throughout this research is representative of the SSME LPOP inducer and was designed in the Gas Turbine Laboratory (GTL) at MIT. Details can be found in Chapter 3 and in [13].

2.3.1 Lumped Parameter Inducer Model

The lumped parameter model characterizes the dynamics of the inducer based on bulk properties such as: inertance, resistance, pump gain, mass flow gain factor, and cavitation compliance. The last two are properties of the cavitation void volume and are assumed to only affect the mass conservation of the inducer. For steady flow the cavitation void volume depends on the inlet pressure (cavitation number) and mass flow (inducer flow coefficient) so the change in cavitation void volume is:

$$\partial V_C = \partial p \frac{\partial V_C}{\partial p} + \partial \dot{m} \frac{\partial V_C}{\partial \dot{m}}, \quad (2.30)$$

where V_C is the cavitation void volume. Based on this the dimensional compliance and mass flow gain factor can be defined as

$$\begin{aligned} C^* &= \rho \frac{\partial V_C}{\partial p} \\ M^* &= \rho \frac{\partial V_C}{\partial \dot{m}}. \end{aligned} \quad (2.31)$$

From continuity across the inducer

$$\dot{m}_1 - \dot{m}_2 = \rho \frac{\partial V_C}{\partial t} = \rho \frac{\partial V_C}{\partial p} \frac{\partial p}{\partial t} + \rho \frac{\partial V_C}{\partial \dot{m}} \frac{\partial \dot{m}}{\partial t} \quad (2.32)$$

which written in terms of compliance and mass flow gain factor becomes

$$\dot{m}_1 - \dot{m}_2 = C^* \frac{\partial p}{\partial t} + M^* \frac{\partial \dot{m}}{\partial t}. \quad (2.33)$$

Linearizing this equation, non-dimensionalizing it, taking the Laplace transform, and converting mass flow terms into velocity terms results in

$$\tilde{U}_2 = -Cs\tilde{P}_1 + (1 - sM)\tilde{U}_1. \quad (2.34)$$

The pressure rise across the inducer in the frequency domain can be written as [17]

$$\tilde{p}_2 = G^* \tilde{p}_1^* - (R^* + s^* L^*) \dot{\tilde{m}}_2 \quad (2.35)$$

where G^* is the dimensional pump gain. Non-dimensionalizing the pressure rise equation and casting it in matrix form with the continuity equation yields the inducer lumped parameter model

$$\begin{bmatrix} \tilde{P}_2 \\ \tilde{U}_2 \end{bmatrix} = \begin{bmatrix} G + s(R + sL)C & (R + sL)(1 - sM) \\ sC & 1 - sM \end{bmatrix} \begin{bmatrix} \tilde{P}_1 \\ \tilde{U}_1 \end{bmatrix}. \quad (2.36)$$

2.3.2 1D Cavitation Surge Model

A recent study by Yu et al. [23] introduced a new model based identification scheme to experimentally identify the cavitation compliance and mass flow gain factor of a cavitating inducer from a single unsteady pressure measurement. Instead of directly solving an eigenvalue problem to determine the system natural frequency and stability, the identification scheme uses the inducer model to infer the correct cavitation compliance and mass flow gain factor that yields an eigenvalue that matches the measured frequency of rotating cavitation at the cavitation number corresponding to the onset of the instability. The modeling was primarily focused on rotating cavitation, a two dimensional instability, and the approach was reduced for planar oscillations, i.e. cavitation surge, for this thesis.

The model created in [23] adapted an existing semiactuator disk model [18] with a blade cavity model to represent the cavitation void as seen in Figure 2-2.

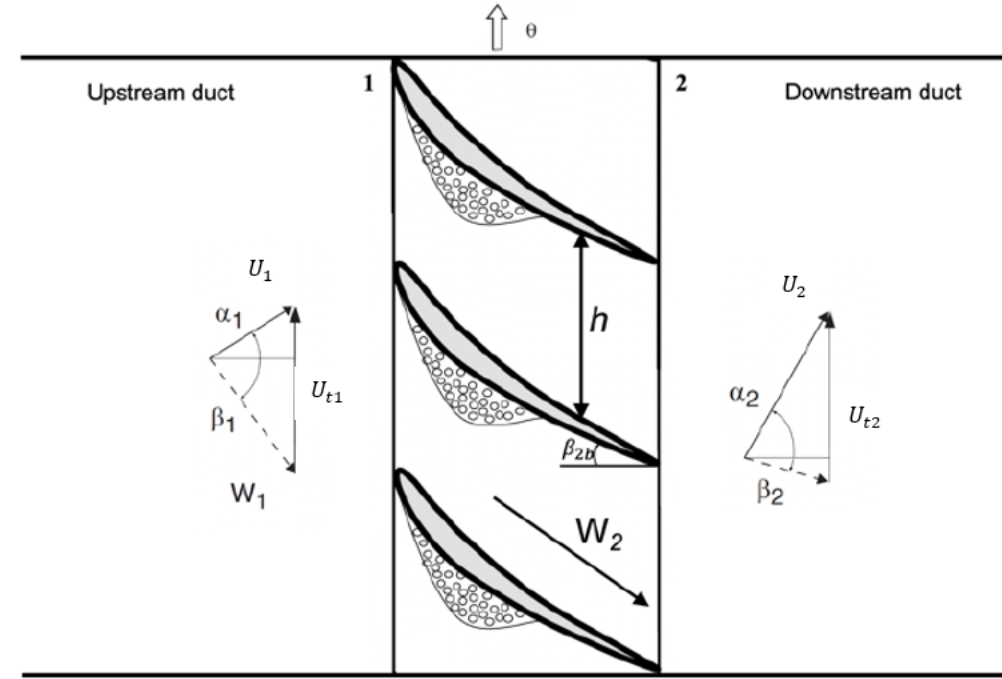


Figure 2-2: Cavitating semi-actuator disk model [23]

The effects of cavitation were represented in the continuity equation by the cavitation void volume, and through additional losses caused by cavitation in the inducer pressure head rise. As such, the matching conditions in two dimensions across the cavitating inducer can be written as

$$A_2 U_{x2} - A_1 U_{x1} = \left(\frac{\partial}{\partial \tau} + \frac{\partial}{\partial \theta} \right) V_C \quad (2.37)$$

$$U_{\theta 2} = U_{x2} \tan \beta_{2b} \quad (2.38)$$

$$P_{t2} - P_{t1} = U_{t2} U_{\theta 2} - U_{t1} U_{\theta 1} - L_{cav} - L_{ind} - L \left(\frac{\partial}{\partial \tau} + \frac{\partial}{\partial \theta} \right) U_1 \quad (2.39)$$

where U_t is the rotor tip velocity, U_θ is the velocity in the circumferential direction, θ refers to the circumferential direction, U_x is the axial velocity, and L_{cav} and L_{ind} are the cavitation and inducer stagnation pressure losses respectively. The cavitation volume is represented as a function of cavitation number, σ and incidence angle, α , and is defined to be in terms of cavitation volume per unit span a_C .

$$a_C(\sigma, \alpha) = \frac{V_C h_1}{A_1} \quad (2.40)$$

Therefore the change in cavitation volume per unit span is related to the velocity and pressure perturbations by

$$\begin{aligned} \partial a_C(\sigma_1, \alpha_1) &= F_1 \partial U_{x1} + F_2 \partial U_{\theta 1} + F_3 \partial P_1 \\ F_1 &= M_L \frac{\sin \beta_1 \cos \beta_1}{\bar{U}_{x1}} \\ F_2 &= -M_L \frac{\cos \beta_1^2}{\bar{U}_{x1}} \\ F_3 &= -2 \frac{C_L}{r_1^2} \end{aligned} \quad (2.41)$$

where the subscript, L , refers to the local compliance or mass flow gain factor, r is the tip radius, and β is the flow angle.

Because cavitation instabilities are observed to be periodic around the annulus, the unsteady perturbations were decomposed into circumferential spatial harmonics. For

example the pressure perturbation can be presented with a Fourier series as

$$\tilde{p}(x, \theta, t) = \sum_{n=0}^{\infty} \text{Re}\{p'_n(x, t)e^{jn\theta}\}, \quad (2.42)$$

where n refers to the spatial harmonic and the superscript $(')$ refers to the spatial Fourier coefficient. In this definition the 0th harmonic represents the planar oscillations, or cavitation surge, and the 1st harmonic represents rotating cavitation. The transmission matrix in two dimensions can be determined by combining the equations (2.37 -2.41), linearizing with small amplitude perturbations, and solving in the frequency domain. The full transmission matrix can be found in [23].

However, to adapt this model to planar oscillations, the circumferential variation of the flow were neglected and $n = 0$ was set for cavitation surge. As a result the transmission matrix for the 1D cavitation surge model is

$$\begin{bmatrix} \tilde{P}_2 \\ \tilde{U}_2 \end{bmatrix} = \begin{bmatrix} 1 - 2\frac{\partial L_{cav}}{\partial \sigma_T} - \frac{AR^2 H_1 F_3 \bar{u}_1}{\cos \beta_{2b}^2} s & \bar{u}_1 \left(1 - \frac{AR^2}{\cos \beta_{2b}}\right) - \left(L + \frac{AR^2}{\cos \beta_{2b}} H_1 F_1\right) s \\ AR H_1 F_3 s & + \frac{\partial L_R^{SS}}{\partial \tan \beta_1} \frac{\tan \beta_1}{\bar{u}_1 (1 + \tau_R s)} \end{bmatrix} \begin{bmatrix} \tilde{P}_1 \\ \tilde{U}_1 \end{bmatrix}. \quad (2.43)$$

2.4 Transmission Matrix Stacking

With all the models now defined, components can be stacked together to build a fluid system. Figure 2-3 illustrates the simplest application of a transmission matrix, incompressible flow through a compact axial duct.

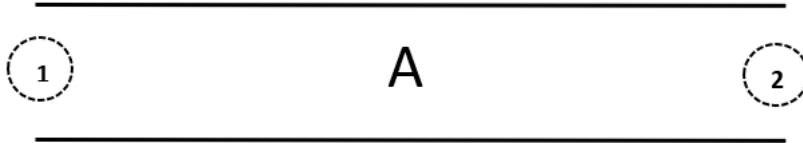


Figure 2-3: Compact duct model

Because the fluid is incompressible, and the duct is rigid, the dynamics of this

device are governed only by fluid inertia and resistance. As such downstream flow perturbations are related to the upstream flow perturbations by the duct transmission matrix as follows

$$\begin{bmatrix} \tilde{P}_2 \\ \tilde{U}_2 \end{bmatrix} = \begin{bmatrix} 1 & -(R_A + sL_A) \\ 0 & 1 \end{bmatrix} \begin{bmatrix} \tilde{P}_1 \\ \tilde{U}_1 \end{bmatrix} \quad (2.44)$$

or

$$\vec{x}_2 = T_A \vec{x}_1 \quad (2.45)$$

where T_A is the duct transmission matrix, and \vec{x} is the state vector comprised of the pressure and velocity perturbations.

The key benefits of transmission matrix modeling, however, is the ease of which it is possible to characterize complex systems and the flexibility with which to change that system. To expand the fluid system a duct, accumulator and duct are placed in series with each other as shown in Figure 2-4.

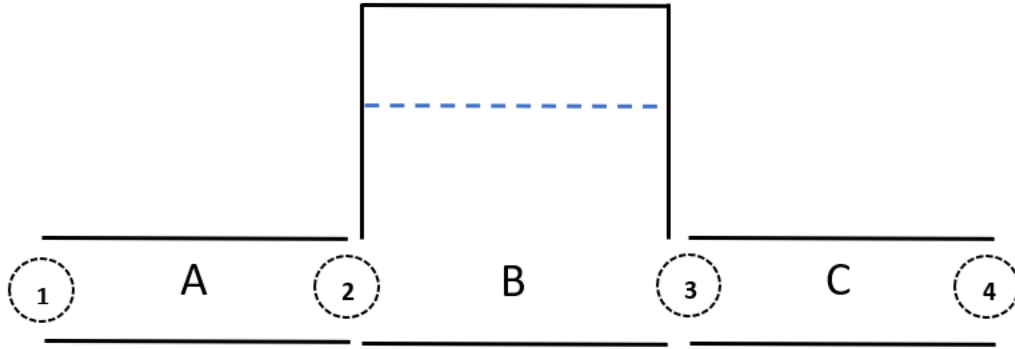


Figure 2-4: Stacking of accumulator with compact upstream and downstream ducts

The perturbations at station 2 going into the accumulator are linked to the initial perturbations at station 1, by the inertia and resistance of duct A captured by the transmission matrix, T_A . The perturbations at station 3 are linked to station 2 by the compliance of the accumulator which is captured in the accumulator transmission matrix, T_B , and the perturbations at station 4 resulted from the dynamics of duct C which is captured in the transmission matrix, T_C . The final transmission matrix

equation relating the inlet perturbations to the exit perturbations is

$$\begin{bmatrix} \tilde{P}_4 \\ \tilde{U}_4 \end{bmatrix} = \begin{bmatrix} 1 & -(R_C + sL_C) \\ 0 & 1 \end{bmatrix} \begin{bmatrix} 1 & 0 \\ -C_B s & 1 \end{bmatrix} \begin{bmatrix} 1 & -(R_A + sL_A) \\ 0 & 1 \end{bmatrix} \begin{bmatrix} \tilde{P}_1 \\ \tilde{U}_1 \end{bmatrix} \quad (2.46)$$

or

$$\vec{x}_4 = T_C \vec{x}_3 = T_C T_B \vec{x}_2 = T_C T_B T_A \vec{x}_1. \quad (2.47)$$

Seen from these examples, modification of the model to the fluid system only requires knowledge of the individual component, and as such models of large and complex systems can be built.

2.5 Boundary Conditions

To close the model, appropriate boundary conditions have to be applied so that an eigenvalue problem can be formed. The eigenvalues are then solved for to determine the system natural frequencies, $s = \sigma + j\omega$, where σ is the growth rate and ω is the frequency of the oscillation. A negative growth rate implies exponential decay so stable oscillations, and a positive growth rate implies exponential growth so unstable oscillations. By imposing boundary conditions on the system transmission matrix equation, one of the two equations will simplify to the form

$$F(s)x = 0 \quad (2.48)$$

where $F(s)$ is a function of s . For any arbitrary x , $F(s)$ must equal to 0.

2.5.1 Open/Closed Boundary Conditions

The open/closed boundary conditions of a fluid system is analogous to the open/closed boundary conditions of an organ pipe. If the boundary is closed, there is a velocity node at the boundary where pressure oscillates, but flow cannot and thus $\tilde{P} \neq 0$ and

$\tilde{U} = 0$. Similarly, if the boundary is open then there is a pressure node, and the opposite is true where $\tilde{P} = 0$ and $\tilde{U} \neq 0$.

For this section, consider the transmission equation:

$$\begin{bmatrix} \tilde{P}_2 \\ \tilde{U}_2 \end{bmatrix} = \begin{bmatrix} T_{11} & T_{12} \\ T_{21} & T_{22} \end{bmatrix} \begin{bmatrix} \tilde{P}_1 \\ \tilde{U}_1 \end{bmatrix}. \quad (2.49)$$

The 4 combinations of boundary conditions and the resulting characteristic equations are:

- Open-Open: If the system is open at both the inlet and exit then $\tilde{P}_1 = \tilde{P}_2 = 0$ which reduces Eq. (2.49) to

$$T_{12}\tilde{U}_1 = 0 \quad (2.50)$$

- Open-Closed: If the system is open at the inlet and closed at the exit then $\tilde{P}_1 = \tilde{U}_2 = 0$ which reduces Eq. (2.49) to

$$T_{22}\tilde{U}_1 = 0 \quad (2.51)$$

- Closed-Open: If the system is closed at the inlet and open at the exit then $\tilde{U}_1 = \tilde{P}_2 = 0$ which reduces Eq. (2.49) to

$$T_{11}\tilde{P}_1 = 0 \quad (2.52)$$

- Closed-Closed: If the system is closed at both the inlet and exit then $\tilde{U}_1 = \tilde{U}_2 = 0$ which reduces Eq. (2.49) to

$$T_{21}\tilde{P}_1 = 0 \quad (2.53)$$

2.5.2 Periodic Boundary Conditions

When the fluid system being model is a closed looped, boundary conditions are periodic.

$$\begin{bmatrix} \tilde{P}_1 \\ \tilde{U}_1 \end{bmatrix} = \begin{bmatrix} T_{11} & T_{12} \\ T_{21} & T_{22} \end{bmatrix} \begin{bmatrix} \tilde{P}_1 \\ \tilde{U}_1 \end{bmatrix} \quad (2.54)$$

Periodic boundary conditions are more complex than open/closed boundary conditions as multiple elements of the transmission matrix are needed to determine the characteristic equation. To determine the characteristic equation, the fluid impedance z is introduced.

$$z = \frac{\tilde{P}}{\tilde{U}} \quad (2.55)$$

The equation relating the downstream pressure perturbation to the upstream perturbations can be rewritten in terms of the impedance as follows:

$$\begin{aligned} \frac{1}{\tilde{U}_1}(\tilde{P}_1 = T_{11}\tilde{P}_1 + T_{12}\tilde{U}_1) \\ z_1 = T_{11}z_1 + T_{12}. \end{aligned} \quad (2.56)$$

And the equation relating the downstream velocity perturbations to the upstream perturbations can be rewritten as follows:

$$\begin{aligned} \frac{1}{\tilde{U}_1}(\tilde{U}_1 = T_{21}\tilde{P}_1 + T_{22}\tilde{U}_1) \\ 1 = T_{21}z_1 + T_{22}. \end{aligned} \quad (2.57)$$

Isolating the impedance of both equations and combining the 2 results in

$$z_1 = \frac{T_{12}}{1 - T_{11}} = \frac{1 - T_{22}}{T_{21}} \quad (2.58)$$

and the characteristic equation for periodic boundary conditions becomes

$$(1 - T_{11})(1 - T_{22}) - T_{12}T_{21} = 0. \quad (2.59)$$

Chapter 3

Experimental Analysis and Transmission Matrix Modeling of Cavitation Dynamics in the MIT Inducer

The MIT inducer was tested in The Aerospace Corporation’s inducer cavitation test facility. The inducer head rise characteristic curve, head fall off curves, and cavitation dynamics can be found in [13]. The steady performance data from these tests were used in the modeling framework to infer the dynamic behaviour of the MIT inducer. This chapter gives an overview of the steady and unsteady performance of the MIT inducer, and uses the observed dynamics to verify the free response modeling framework in terms of cavitation surge onset condition and frequency content.

3.1 Free Response Test Experimental Setup

The Aerospace Corporation in El Segundo, California operates a water test facility for rocket engine turbopump inducer cavitation testing. The test facility was designed to be a flexible, low cost system used to capture the cavitating performance and dynamics of a variety of inducers over a wide range of operating conditions. A

summary of the system's capabilities is presented here, and detailed information of the system's capability can be found in [6]. To properly characterize cryogenic pump performance, the facility carefully controls three non-dimensional scaling parameters: the inlet cavitation number, σ_1 , the inlet flow coefficient, ϕ , and the thermodynamic bubble growth parameter, DB . The control of these parameters allows for the proper simulation of dynamically similar flight operating conditions.

The flow coefficient is a non-dimensional measure of volumetric flow rate as given by

$$\phi = \frac{Q_1}{A_1 r_T \omega}. \quad (3.1)$$

Q_1 is the inlet volumetric flow rate, ω is the pump rotational speed, r_T is the tip radius, and A_1 is the pump inlet area. The cavitation number, also known as the Euler number, is the non-dimensional measure of the inlet pressure. It is given by

$$\sigma = \frac{p_1 - p_v}{\frac{1}{2}\rho(\omega r_T)^2}, \quad (3.2)$$

where p_1 is the pump inlet static pressure, p_v is the vapor pressure of the fluid at the inducer inlet conditions, and ρ is the fluid density. Both the flow coefficient, and cavitation number determine the performance of the pump, represented non-dimensionally as the total to total head coefficient, ψ_{tt}

$$\psi_{tt} = \frac{p_{t2} - p_{t1}}{\frac{1}{2}\rho(\omega r_T)^2}, \quad (3.3)$$

where p_t is the total pressure at pump inlet and outlet.

Though the thermodynamic bubble growth parameter was not used in the experiments or models carried out in this thesis, Ehrlich and Murdock demonstrated its importance in properly characterizing cryogenic pump performance in [5]. The thermodynamic bubble growth parameter is a non-dimensional representation used to account for the thermal effects on cavitation.

$$DB = \frac{r_T \omega^{\frac{3}{2}}}{\sum} \quad (3.4)$$

Σ is the thermal parameter defined by Brennen [1], ρ_l is the liquid density, ρ_g is the vapor gas density, h_{fg} is the heat of formation of the gas, c_{pl} is the specific heat of the liquid, T is the fluid temperature, and α is the thermal diffusivity of the liquid.

$$\Sigma = \frac{\rho_g^2 h_{fg}^2}{\rho_l c_{pl} T \alpha^{1/2}} \quad (3.5)$$

The test facility controls the flow coefficient by opening and closing a porous media throttle valve and the cavitation number is controlled through with a vacuum pump that changes the ullage pressure of the storage tank. The temperature is controlled through a heating element placed inside the storage tank.

In addition to controlling the scaling parameters, the facility also utilizes a series of secondary support systems. Because cavitation is known to be sensitive to impurities in the fluid [1], the water test facility utilizes a helium sparging system and dissolved oxygen sensor to remove dissolved gases. A 1 micron bag filtration system removes any particulates in the system. Images of the system are shown in Figure 3-1 and 3-2.



Figure 3-1: Aerospace Corporation's inducer test facility [6]

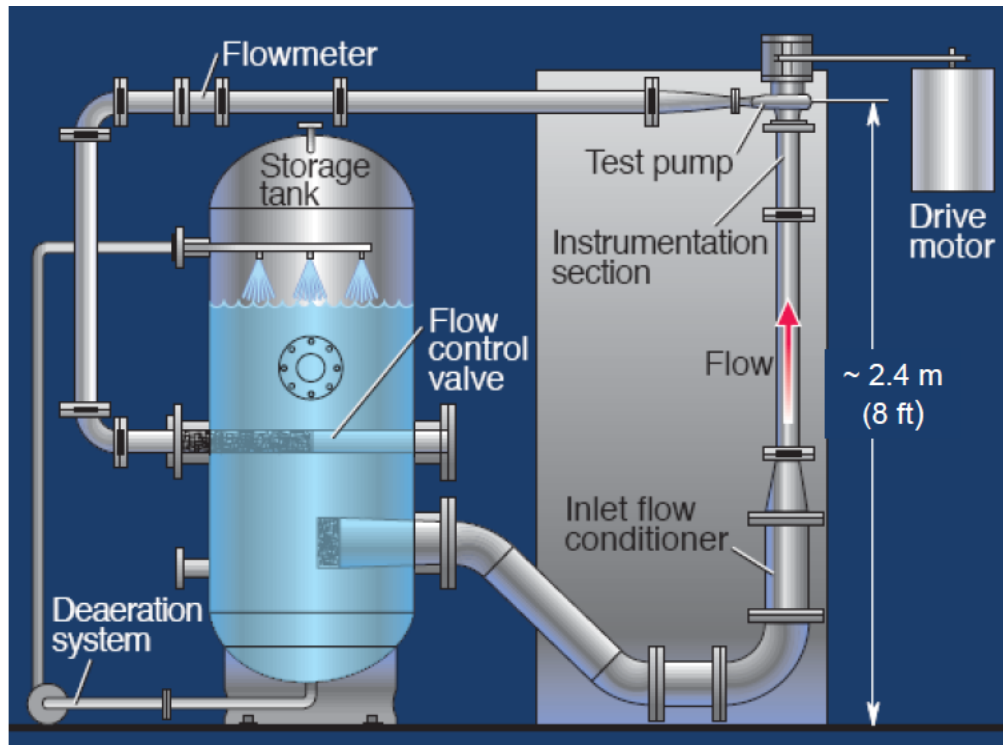


Figure 3-2: Schematic of inducer test facility [6]

The facility can test a variety of inducers up to 76mm in diameter and up to speeds of 5000 rpm. The inducer is mounted vertically to avoid the hydrostatic pressure gradient across the inducer face that is present in horizontal test configurations. To allow for different tip clearances, sensor layouts, and optical view points, the inducer is placed in a modular test section that can be interchanged with different housings.

Operation of the test facility and data collection are interfaced through Labview, and a high speed 32 channel data acquisition system (DAQ). The operational pressures and mass flow are measured with a Druck pressure transducer and a Foxboro electromagnetic flowmeter. The shaft position and rotational rate are determined by a BEI optical shaft encoder. The dynamic pressure and velocity response of the inducer is captured using an 8 bit DEWEsoft high speed DAQ, Entran dynamic pressure transducers, and Dantec fiber film probes. More details about the data acquisition system can be found in [6].

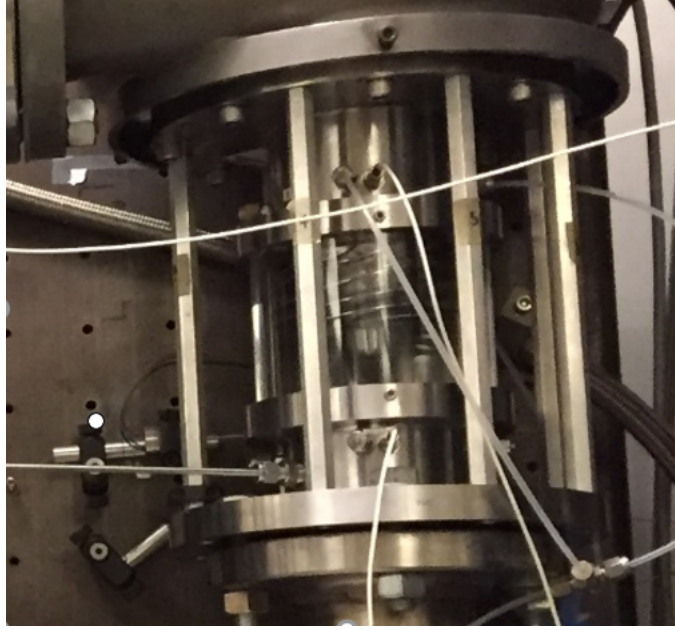


Figure 3-3: Close up of inducer test section

3.2 MIT Inducer

The MIT inducer is unshrouded with backswept leading edges and forward canted blades. The inducer consists of 4 blades and 12 tandem blades. More detailed descriptions of the inducer geometry can be found in [13]. The MIT inducer is shown in Figure 3-4 and the dimensions are summarized in Table 3.1.

Table 3.1: Dimensions of MIT Inducer

	Inducer	Tandem Blades
Inlet Design Flow Coefficient	0.07	0.14
Blades	4	12
Tip radius, mm	37.8	37.8
Inlet hub-to-tip ratio	0.29	0.74
Outlet hub-to-tip ratio	0.72	0.83
Inlet tip angle, deg	82.7	81
Outlet tip angle,	74	60
Backsweep, deg	120	0
Inlet tip gap relative to span, %	1	2.7

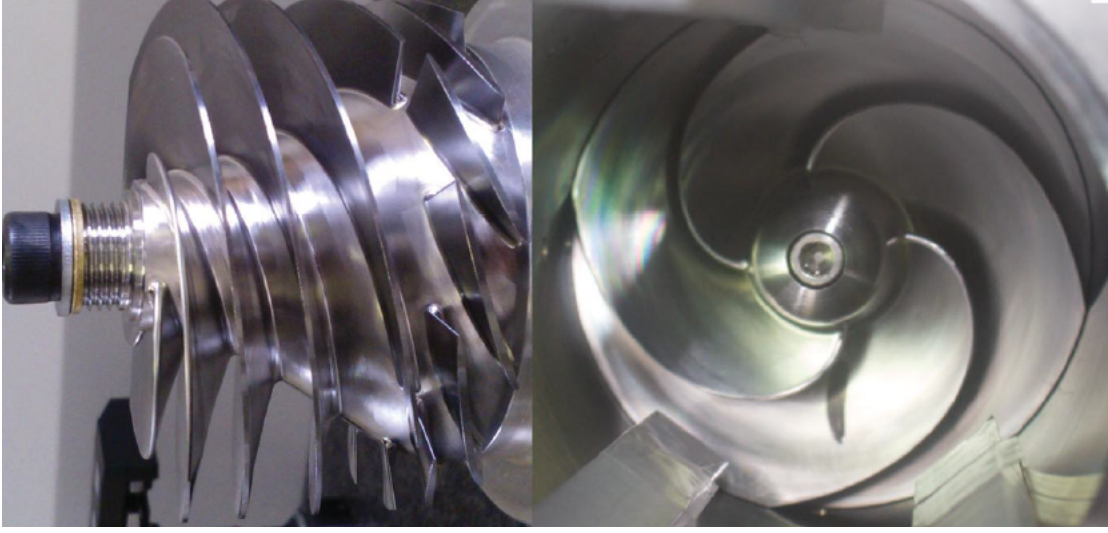


Figure 3-4: MIT inducer test hardware

3.2.1 MIT Inducer Steady Performance

The non-cavitating and cavitating steady state performance of the MIT inducer is needed to properly model the inducer as discussed in Sections 2.3.1 and 2.3.2. The non-cavitating performance is generally captured in a pump head characteristic curve where the pump head rise coefficient is plotted against the inlet flow coefficient. The cavitating performance is captured in a head fall-off curve or "knee curve" where the head rise is plotted against the inlet cavitation number for a given flow coefficient.

The MIT inducer was tested in room temperature water and the performance is shown in Figure 3-5. The blue line labeled, ψ_{ts}^{act} is the measured total to static pressure head rise coefficient. The curve was determined by polynomial fitting the measured data points (red dots). The orange ideal head rise curve was inferred from geometry, ψ_{ts}^{ideal} , and used to find the purple inducer loss curve, L_{ind} . The inset figure is the inducer knee curve at a flow coefficient $\phi = 0.06$.

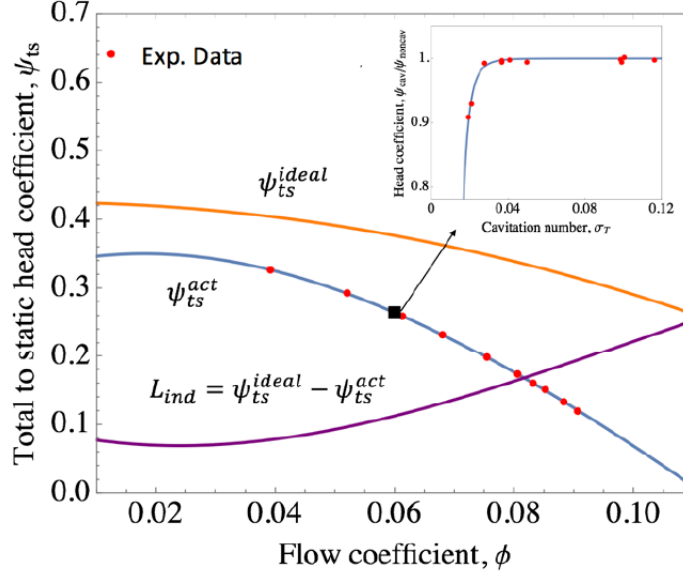


Figure 3-5: Measured non-cavitating performance and inferred stagnation pressure loss. Inset shows cavitation performance head loss curve at $\phi = 0.06$ [23]

3.2.2 Cavitation Dynamics of The MIT Inducer

Dynamic pressure measurements were used to characterize the cavitation dynamics of the MIT inducer. Cavitation surge, rotating cavitation and alternate blade cavitation were observed during the free response experiments. At a flow coefficient, $\phi = 0.083$ all 3 types of cavitation were observed. Figure 3-6 summarizes the regimes of cavitation along the knee curve. Further discussion on the characterization of rotating cavitation can be found in [13, 23].

Cavitation surge was more apparent at lower flow coefficients. Figure 3-7 shows the non-dimensional dynamic pressure measurements versus time in rotor revolutions and the corresponding spectrogram. During this test, the inducer operated at $\phi = 0.06$ as the inlet cavitation number was decreased over time. From Figure 3-7 the magnitude of the perturbations did not consistently increase with the decrease in cavitation number, instead there was an abrupt increase in the magnitudes at $\sigma = 0.03$ and an abrupt decrease in the magnitude at $\sigma = 0.02$. This sharp increase and decrease in magnitude was an onset and termination of cavitation surge instability. The cavitation surge frequency however did change with the cavitation number, until

the onset of the instability. During the instability the cavitation surge frequency was found to be roughly constant at 0.09 of rotor frequency.

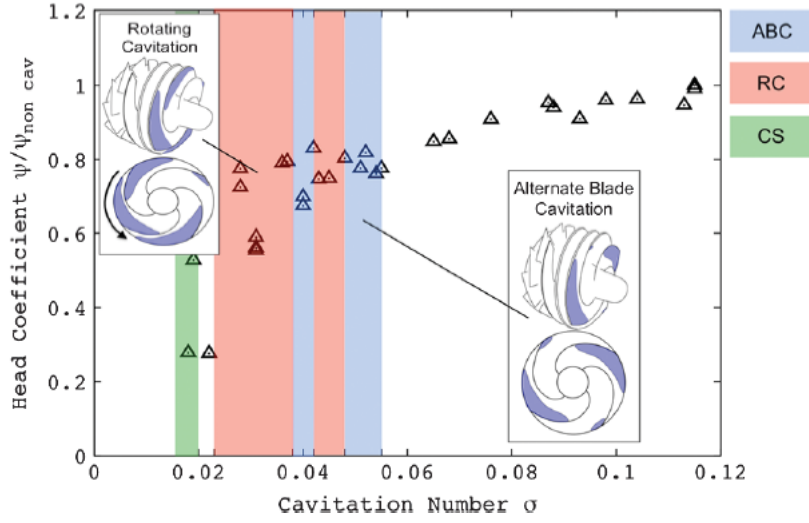


Figure 3-6: Cavitation regimes along the inducer knee curve at $\phi = 0.083$ [13]

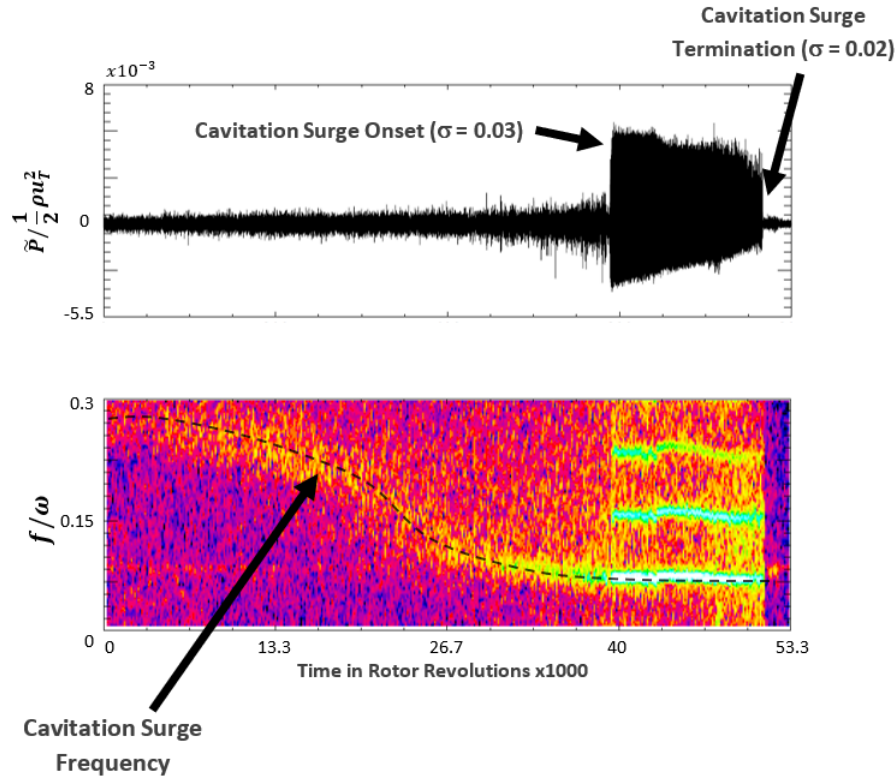


Figure 3-7: Time series data of cavitation surge (top) and spectrogram of cavitation surge data (bottom) of MIT inducer at $\phi = 0.06$ [10]

3.3 Free Response Model Implementation and Verification with Experimental Data

The framework derived in Chapter 2 was used to replicate the measured cavitation surge dynamics summarized in Section 3.2.2. The model was anchored such that the real part of the eigenvalues match the observed stability trends, and such that the imaginary part of the eigenvalues agreed with the measured cavitation surge frequency. The model accounted for the dynamics of each fluid device used in the test facility with a compact lumped transmission matrix. The dynamics of the fluid system was simulated over the cavitation number range $\sigma = 0.02$ to $\sigma = 0.1$ and $\phi = 0.06$.

3.3.1 Fluid System Component Modeling and Stacking

The inducer test facility has a large number of components that need to be modeled. Figure 3-8 shows a schematic of the test facility.

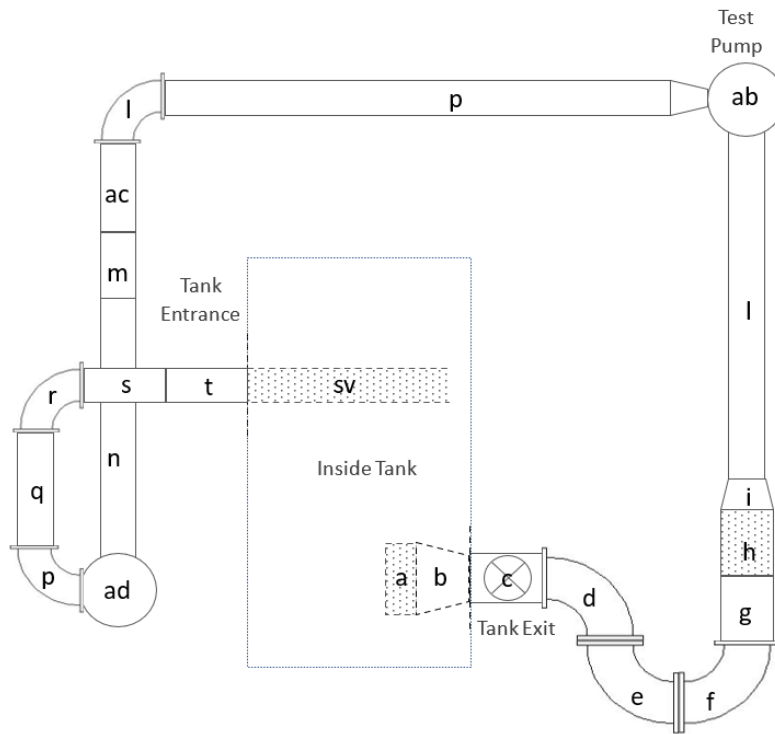


Figure 3-8: Schematic of inducer test facility

Each component except for the inducer and tank were modeled with the compact incompressible duct model, Eq. (2.20). The tank was modeled using the gas accumulator model, Eq. (2.28), and the inducer was modeled using the 1D cavitation surge model. Appendix B illustrates the decision to use the 1D cavitation surge model over the lumped parameter inducer model. The majority of components were able to be modeled using the acoustically compact duct model, Eq. (2.20), because the wavelength of the perturbation was much larger than the sum of the lengths of the components. The wavelength of the flow perturbations was estimated using the cavitation surge frequency and the speed of sound in water, and verified with the simulated eigenvalue natural frequencies. The inertance and resistance of each element in the inducer test facility were empirically measured in [9]. Each component description and its non-dimensional resistance and inertance values can be found on Table 3.2.

Because the inlet cavitation number is controlled through modulation of the storage tank ullage pressure, the compliance of the tank as a function of the pump inlet cavitation number was experimentally determined. The experimentally measured compliance of the tank as a function of cavitation number can be found in Appendix A.

To model the inducer using the 1D cavitation surge model, the MIT inducer loss characteristics presented in Section 3.2.1 were used. The MIT inducer geometry was used to determine the inertance, and a modified version of the the CFD estimated mass flow gain factor and cavitation compliance, from [10], were used. C and M were modified because there was poor matching between the measured and simulated dynamics, using the unaltered CFD mass flow gain factor and cavitation compliance. The modification of the compliance and mass flow gain factor are discussed in Section 3.3.3. The non-dimensionalized compliance and mass flow gain factor from [10] are plotted in Appendix A.

Because the inducer test facility was a closed loop system, a periodic boundary condition is the appropriate condition to apply to this modeling framework. However, since all fluid originates and ends back in the storage tank, which has a large

Table 3.2: Inducer test facility components and non-dimensional resistances and inertances

Element Number	Element	Element Description	Resistance ($\times 10^{-4}$)	Inertance
1	a	Inlet Flow Straightener	2.94	0.19
2	b	Tank Entrance	75.88	0.45
3	c	6" Ball Valve	3.81	4.67
4	d	90 Degree Elbow	20.55	4.87
5	e	90 Degree Elbow	20.55	4.87
6	f	90 Degree Elbow	20.55	4.87
7	g	Bellows	3.06	3.76
8	h	Inlet Flow Conditioner	2054.05	4.25
9	i	Inlet Contraction	822.04	3.02
10	l	Inlet Line Vertical Section	368.04	51.77
11	ab	Pump Housing from Inducer Exit to Discharge Flange	84502.29	25.89
12	p	Discharge Line Horizontal Straight Section	718.22	118.23
13	l	90 Degree Elbow	328.82	8.77
14	ac	Section Between Elbows	113.62	18.70
15	m	45 Degree Elbow	219.21	18.70
16	n	Section Between Elbow and Boost Pump	446.35	73.48
17	ad	90 Degree Elbow	328.81	8.78
18	p	90 Degree Elbow	328.81	8.78
19	q	Section Between 90 Degree Elbow	146.08	8.78
20	r	90 Degree Elbow	328.81	8.78
21	s	Section Between Elbow and sv Ball Valve	109.56	18.04
22	t	Discharge Line Ball Valve Straight Section	64.92	10.69
23	sv	Porous Flow Control Valve	189484.9	8.78

ullage volume, a reasonable approximation would be to assume an open-open boundary condition without the storage tank. This assumption reduces complexity in the free and forced response model. Comparisons of the two boundary conditions in Section 3.3.2 shows that this approximation has little effect on the predicted dynamics and the open-open boundary condition was applied to the forced response modeling framework.

After determining each transmission matrix for each component and the boundary conditions, the matrices were stacked to form the overall model of the inducer test facility. Using open-open boundary conditions in place of the storage tank, the facility transmission matrix equation is

$$\begin{bmatrix} \tilde{0} \\ \tilde{U}_2 \end{bmatrix} = \prod_{n=11}^{23} \begin{bmatrix} 1 & -L_n s - R_n \\ 0 & 1 \end{bmatrix} [T_{inducer}] \prod_{n=1}^{10} \begin{bmatrix} 1 & -L_n s - R_n \\ 0 & 1 \end{bmatrix} \begin{bmatrix} \tilde{0} \\ \tilde{U}_1 \end{bmatrix}. \quad (3.6)$$

The transmission matrix for the inducer test facility including the storage tank and periodic boundary conditions is

$$\begin{bmatrix} \tilde{P}_1 \\ \tilde{U}_1 \end{bmatrix} = \begin{bmatrix} 1 & 0 \\ -sC_{tank} & 1 \end{bmatrix} \prod_{n=11}^{23} \begin{bmatrix} 1 & -L_n s - R_n \\ 0 & 1 \end{bmatrix} [T_{inducer}] \prod_{n=1}^{10} \begin{bmatrix} 1 & -L_n s - R_n \\ 0 & 1 \end{bmatrix} \begin{bmatrix} \tilde{P}_1 \\ \tilde{U}_1 \end{bmatrix}. \quad (3.7)$$

In both transmission matrix equations the subscript n refers to the element number as indexed in Table 3.2. $[T_{inducer}]$ refers to the cavitating inducer transmission matrix model.

The eigenvalue equation of the open-open system was determined from Eq. (2.50), and the eigenvalue equation of the closed loop system was determined from Eq. (2.59). These two eigenvalues predictions were compared to each other to determine if an open-open boundary condition was an appropriate approximation for modeling of the Aerospace Corporation's inducer test facility.

3.3.2 Boundary Condition Selection

In the comparison of the two boundary conditions, this section used both inducer models when comparing the eigenvalues. The compliance and mass flow gain factor were the CFD derived values from Jackson et al. [9]. All simulations occurred at the same flow coefficient as the test data, $\phi = 0.06$.

Using the lumped parameter model, the eigenvalues found using both boundary conditions are shown in Figure 3-9. The root locus plot begins with $\sigma = 0.1$ and decreases to $\sigma = 0.02$. The error percentage between the 2 boundary conditions is shown in Figure 3-10. The average error percentage across the inlet cavitation range was 0.3% and the maximum error was 0.5%. As such with the lumped parameter model, an open-open boundary condition is nearly identical to using a periodic boundary condition.

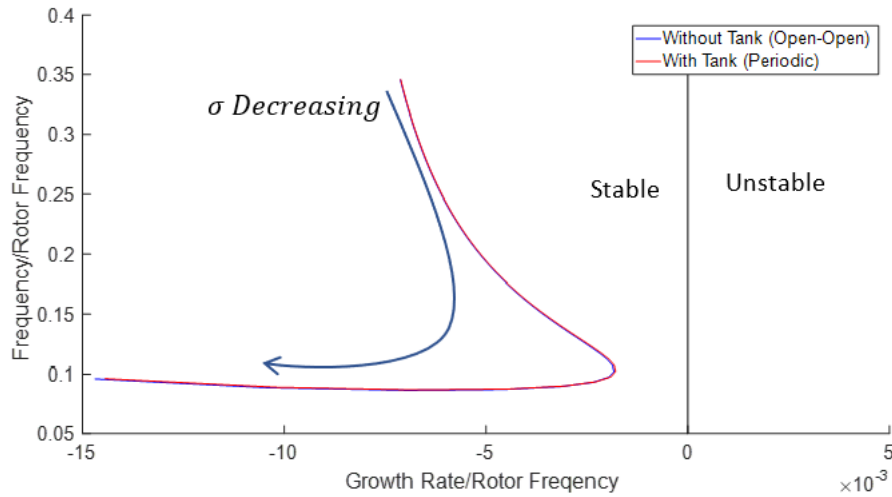


Figure 3-9: The root locus plots using the lumped parameter inducer model shows very similar estimates for the cavitation surge eigenvalues regardless of the boundary condition

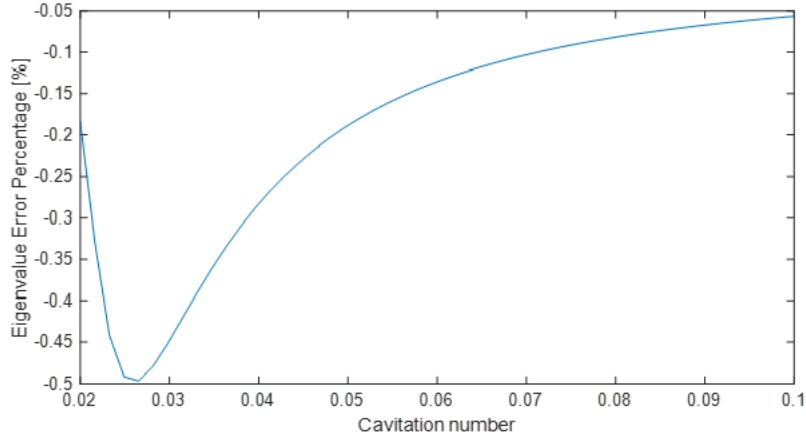


Figure 3-10: The error percentage between the eigenvalues of the two boundary conditions when using the lumped parameter inducer model is small, indicating that the open-open boundary condition is an appropriate approximation

The simulations with the 1D cavitation surge model resulted in a similar conclusion. Figure 3-11 shows the eigenvalues found using the 1D cavitation surge model and the two boundary conditions. Figure 3-12 shows the error percentage between the two boundary conditions.

The error percentage between the 2 condition using the 1D cavitation surge model was higher than with the lumped parameter model, but still on the order of a percentage point. The average error over the cavitation range was 1.8% with a max error percentage of 3.5%.

With both inducer models showing only small errors in eigenvalue estimations, this thesis used an open-open boundary condition for forced response modeling.

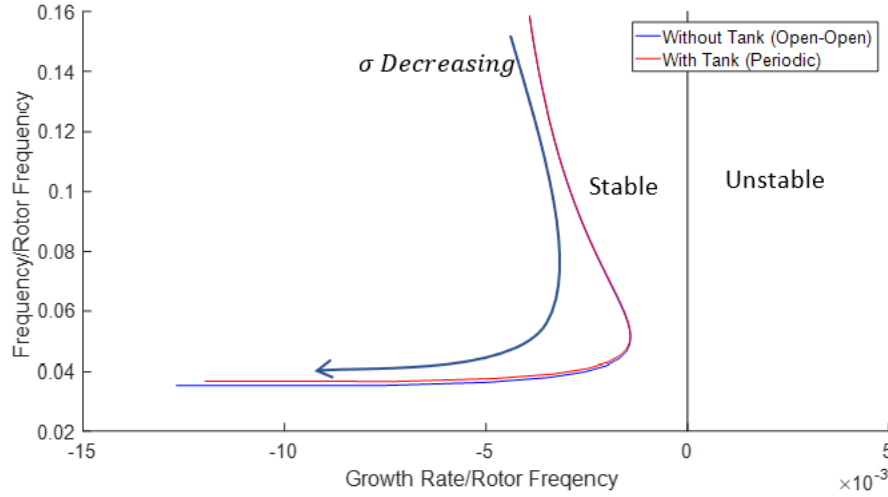


Figure 3-11: The root locus plots using the 1D cavitation surge model shows very similar estimates for the cavitation surge eigenvalues regardless of the boundary condition condition

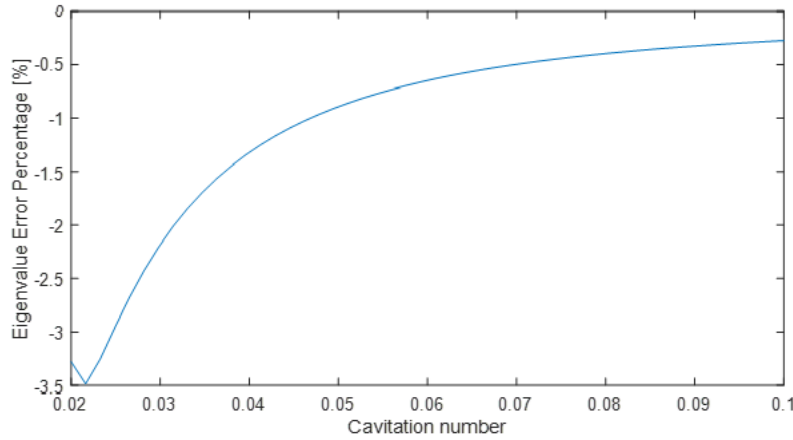


Figure 3-12: The error percentage between the eigenvalues of the two boundary conditions when using the 1D cavitation surge model is small, indicating that the open-open boundary condition is an appropriate approximation

3.3.3 Modeling Framework Verification through Modification of C and M

To match the measured dynamics of the MIT inducer, the modeling framework required modifying the CFD calculated C and M from [9]. Rubin in [17] stated that the cavitation compliance and mass flow gain factor were found to be complex values,

due to the time lag between the response of the cavitation void volume to changes to the operating conditions. Rubin introduced the complex cavitation compliance, and mass flow gain factor in the form of

$$\begin{aligned} C &= \frac{C}{1 + \tau_C} \\ M &= \frac{C}{1 + \tau_M} \end{aligned} \tag{3.8}$$

where τ is a time lag value, he found to be between 0.5 – 3.2. The time lag along with a scaling coefficient was used to modify these parameters until the estimated cavitation surge frequency and stability trends matched the measured data. Table 3.3 shows the modified C and M .

Table 3.3: Modified Cavitation Compliance and Mass Flow Gain Factor

Cavitation Compliance	Mass Flow Gain Factor
$\frac{0.3C}{1+0.5s}$	$\frac{M}{1+0.5s}$

These modifications were added because the frequency content and stability trends found using the unmodified CFD C and M did not matched with the observed data. The cavitation surge frequency using the unmodified CFD C and M was too low when compared to the measured cavitation surge frequency. Like with a helmholtz resonator, the frequency of the cavitation surge instability is inversely proportional to the volume (compliance). As such the comparison between the simulated and measured frequencies indicated that the compliance from CFD was too large, and should be reduced. The frequency comparison is in Figure 3-13.

The model using the unmodified CFD C and M also never predicted the observed onset and termination of cavitation surge instability seen from the test data. To quantify the stability, the critical damping percentage, ζ , is introduced where

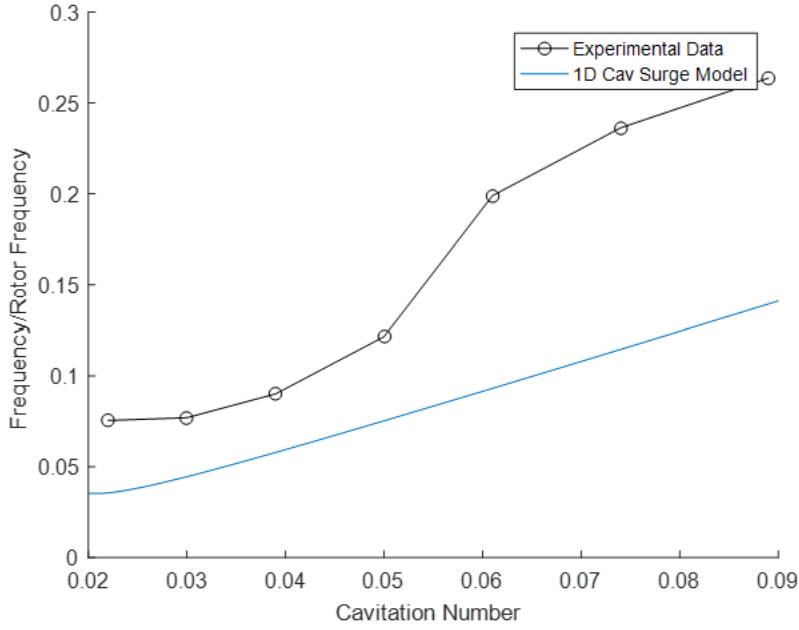


Figure 3-13: Cavitation surge frequency model estimation using unmodified CFD C and M does not match measured cavitation surge frequency

$$\begin{aligned}
 s &= \sigma + j\omega \\
 \omega_n &= \sqrt{\sigma^2 + \omega^2} \\
 \zeta &= \frac{\sigma}{\omega_n} * 100\%.
 \end{aligned}
 \tag{3.9}$$

Figure 3-14 shows the modeled critical damping percentage as a function of cavitation number along with the measured cavitation surge onset and termination points. The stability comparison indicates that there is too much damping in the system and to match the observed behavior the estimated mass flow gain factor needs to also be decreased.

The modified C and M had reflected these observations and matched the measured data more closely. The modified compliance is a smaller value compared to the unmodified CFD compliance due to the added coefficient of 0.3, which increases the cavitation surge frequency such that it matches with the measured frequency as seen in Figure 3-15. Though the addition of the time lag increases the amount of damping within the system, the reduction of the compliance counters the stability increase of

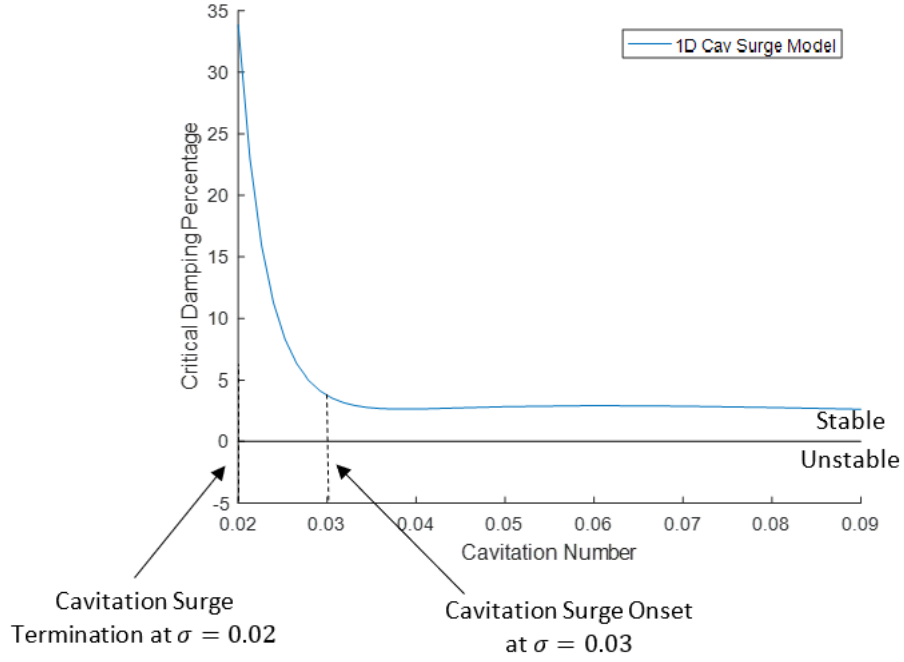


Figure 3-14: Stability trend estimation using unmodified CFD C and M does not match observed stability trend

the time lag. As such there wasn't a need to multiply the mass flow gain factor with a coefficient. These modifications yielded the cavitation surge onset at $\sigma = 0.035$ and cavitation surge termination at $\sigma = 0.027$.

The simulated cavitation surge frequency found with the modified C and M is shown in Figure 3-15 and the modeled stability trend is shown in Figure 3-16.

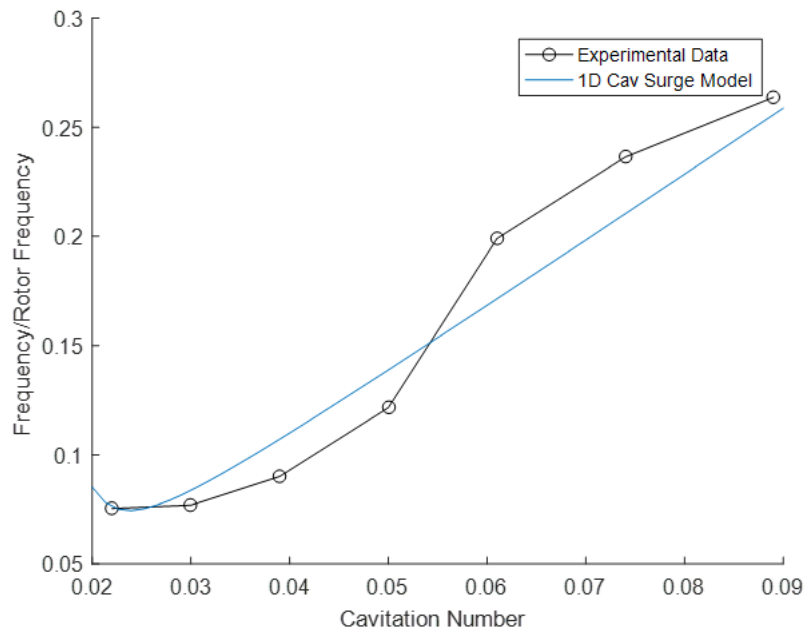


Figure 3-15: Cavitation surge frequency model estimation using modified CFD C and M matches measured cavitation surge frequency

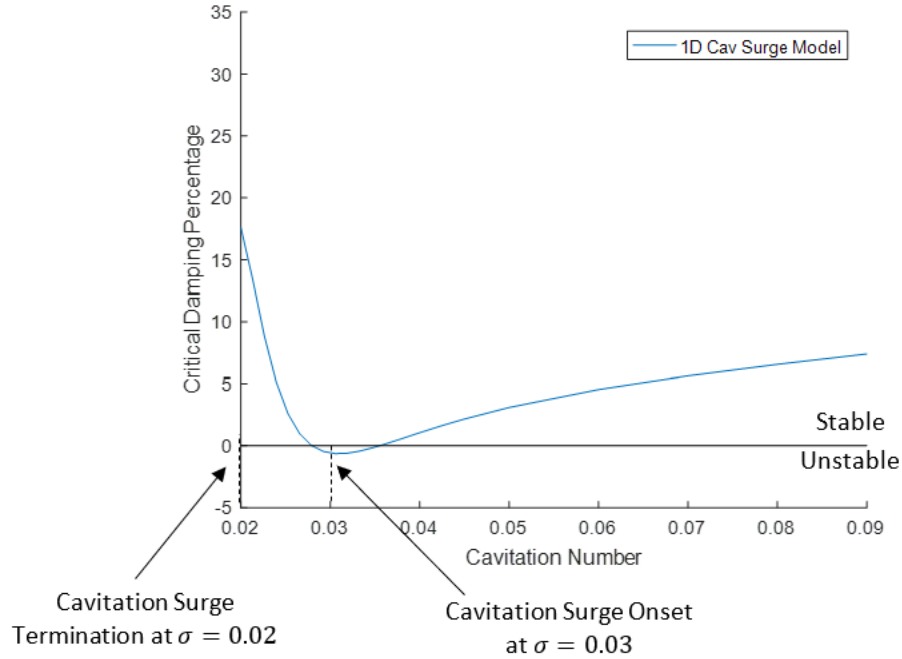


Figure 3-16: Stability trend estimation using modified CFD C and M more closely matches observed stability trend

Chapter 4

Forced Response Modeling and Transfer Function Identification Methodology

To determine the changes to the inducer test facility required for forced response testing, the modeling methodology was extended to guide the design of the experiment. The forced response model consists of determining transfer functions between the piston actuator velocity fluctuations to the pressure and velocity response at different locations in the inducer test facility. This chapter derives the modeling framework used in Chapter 5 and introduces the control theoretical system identification method employed to experimentally determine the inducer transfer function and transmission matrix.

4.1 Drive Point Impedance Modeling

The forced response model utilizes an impedance based modeling approach. The drive point impedance relates the velocity perturbations created by the piston actuator to its pressure perturbations. The drive point impedance is then used to determine the pressure and velocity transfer function at other locations away from the piston using transmission matrices defined in Chapter 2.

The simplest drive point impedance model occurs when the piston actuator is located at a system boundary. For a system described by the transmission matrix, $[T]$, and pulsed at the exit, the transmission matrix equation is as follows:

$$\begin{bmatrix} \tilde{P}_p \\ \tilde{U}_p \end{bmatrix} = \begin{bmatrix} T_{11} & T_{12} \\ T_{21} & T_{22} \end{bmatrix} \begin{bmatrix} \tilde{P}_1 \\ \tilde{U}_1 \end{bmatrix} \quad (4.1)$$

where the subscript (p) refers to the perturbations created by the piston actuator. Using Eq. (2.55), the drive point impedance, z_p of this system is simply

$$z_p = \frac{\tilde{P}_p}{\tilde{U}_p} = \frac{T_{11}\tilde{P}_1 + T_{12}\tilde{U}_1}{T_{21}\tilde{P}_1 + T_{22}\tilde{U}_1}, \quad (4.2)$$

where the boundary conditions will determine the exact form of z_p . If the piston actuator is located at the system inlet, the transmission matrix equation would be defined as follows:

$$\begin{bmatrix} \tilde{P}_2 \\ \tilde{U}_2 \end{bmatrix} = \begin{bmatrix} T_{11} & T_{12} \\ T_{21} & T_{22} \end{bmatrix} \begin{bmatrix} \tilde{P}_p \\ \tilde{U}_p \end{bmatrix}. \quad (4.3)$$

The inverse of the transmission matrix is taken to isolate the piston perturbation so that the transmission matrix equation is

$$\begin{bmatrix} \tilde{P}_p \\ \tilde{U}_p \end{bmatrix} = \frac{1}{|T|} \begin{bmatrix} T_{22} & -T_{12} \\ -T_{21} & T_{11} \end{bmatrix} \begin{bmatrix} \tilde{P}_2 \\ \tilde{U}_2 \end{bmatrix}, \quad (4.4)$$

where $|T|$ refers to the determinant of the matrix. The resulting drive point impedance with the piston actuator at the system inlet is

$$z_p = \frac{\tilde{P}_p}{\tilde{U}_p} = \frac{T_{22}\tilde{P}_2 - T_{12}\tilde{U}_2}{-T_{21}\tilde{P}_2 + T_{11}\tilde{U}_2}. \quad (4.5)$$

Again the boundary conditions will determine the exact form of z_p .

If the boundary conditions are open/closed conditions, then placing the actuator at a system boundary places it on a node of the system. To avoid this the driving point impedance at arbitrary locations is needed. Consider the system shown in

Figure 4-1.

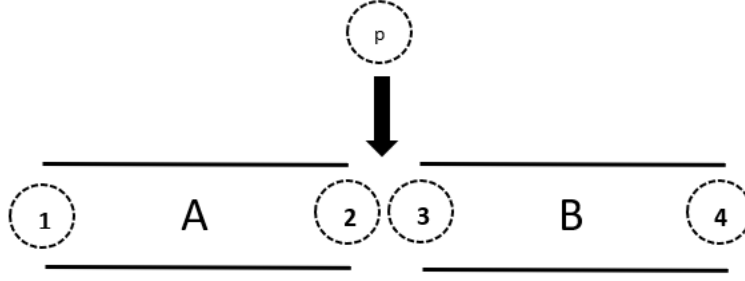


Figure 4-1: Schematic of system with arbitrary pulser location

Figure 4-1, is divided into 2 sections by the piston actuator, one of which the actuator is pulsing at the exit of section A and the other where the actuator is pulsing at the inlet of section B. The impedance from station 1 to station 2, z_a , is the same as the impedance derived in Eq. 4.2. Similarly the impedance from station 4 to station 3, z_b , is the impedance derived in Eq. 4.5.

$$z_a = \frac{A_{11}\tilde{P}_1 + A_{12}\tilde{U}_1}{A_{21}\tilde{P}_1 + A_{22}\tilde{U}_1} \quad (4.6)$$

$$z_b = \frac{B_{22}\tilde{P}_4 - B_{12}\tilde{U}_4}{-B_{21}\tilde{P}_4 + B_{11}\tilde{U}_4} \quad (4.7)$$

At the junction, the pressure perturbations are uniform, and the flow perturbations follows continuity such that

$$\tilde{P}_2 = \tilde{P}_3 = \tilde{P}_p \quad (4.8)$$

$$\tilde{U}_3 = \tilde{U}_2 + \tilde{U}_p. \quad (4.9)$$

Using Eqs. (4.8), (4.9), and (2.55) the drive point impedance can be represented in terms of z_a and z_b .

$$\frac{\tilde{U}_3}{\tilde{P}_3} = \frac{\tilde{U}_2}{\tilde{P}_2} + \frac{\tilde{U}_p}{\tilde{P}_p} \quad (4.10)$$

$$\frac{1}{z_b} = \frac{1}{z_a} + \frac{1}{z_p}$$

$$z_p = \frac{z_a z_b}{z_a - z_b} \quad (4.11)$$

Eqs. (4.6) and (4.7) are true for a system with open/closed boundary conditions,

but not for one with periodic boundary conditions. For a closed loop system the impedances found from Section 2.5.2 can be applied such that the impedances are:

$$z_a = \frac{T_{12}}{1 - T_{11}} \quad (4.12)$$

and

$$z_b = \frac{-T_{12}}{|T| - T_{22}}, \quad (4.13)$$

where T is the transmission matrix of the fluid system.

$$\begin{bmatrix} \tilde{P}_4 \\ \tilde{U}_4 \end{bmatrix} = \begin{bmatrix} \tilde{P}_1 \\ \tilde{U}_1 \end{bmatrix} = [T] \begin{bmatrix} \tilde{P}_1 \\ \tilde{U}_1 \end{bmatrix} \quad (4.14)$$

4.2 Transfer Functions at Arbitrary Locations

To determine the transfer functions at arbitrary locations, the drive point impedance is related to those locations with the system transmission matrices.

4.2.1 Piston Actuator Located Upstream of Sensing Location

Consider the system in Figure 4-2 where the transfer functions are desired at m , located somewhere in the downstream section, B.

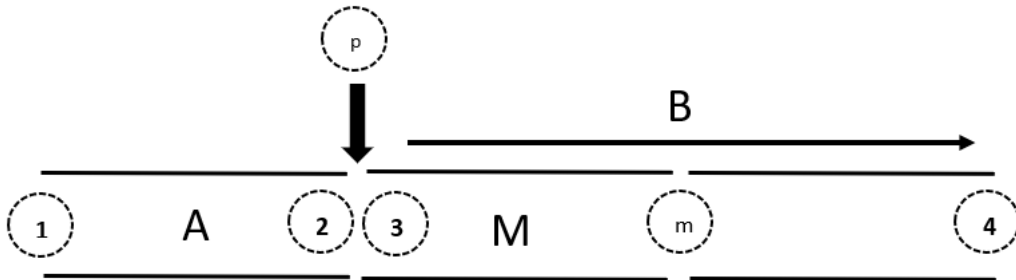


Figure 4-2: Schematic of a system with pulser located upstream of the desired transfer function location, m . Duct M and station m are located within duct B

The perturbations just downstream of the forcing location at station 3 can be related to station m with the transmission matrix as follows:

$$\begin{bmatrix} \tilde{P}_m \\ \tilde{U}_m \end{bmatrix} = \begin{bmatrix} M_{11} & M_{12} \\ M_{21} & M_{22} \end{bmatrix} \begin{bmatrix} \tilde{P}_3 \\ \tilde{U}_3 \end{bmatrix}. \quad (4.15)$$

Using the equations in this matrix, the transfer functions relating the perturbations at m to station 3 are

$$\begin{aligned} \frac{\tilde{P}_m}{\tilde{U}_3} &= M_{11}z_b + M_{12} \\ \frac{\tilde{P}_m}{\tilde{P}_3} &= M_{11} + \frac{M_{12}}{z_b} \\ \frac{\tilde{U}_m}{\tilde{U}_3} &= M_{21}z_b + M_{22} \\ \frac{\tilde{U}_m}{\tilde{P}_3} &= M_{21} + \frac{M_{22}}{z_b} \end{aligned} \quad (4.16)$$

in terms of $z_b = \frac{\tilde{P}_3}{\tilde{U}_3}$. These equations can then be used to find the transfer functions in terms of z_p where

$$\begin{aligned} \frac{\tilde{P}_m}{\tilde{U}_p} &= \frac{\tilde{P}_m}{\tilde{P}_3} z_p = z_p \left(M_{11} + \frac{M_{12}}{z_b} \right) \\ \frac{\tilde{U}_m}{\tilde{U}_p} &= \frac{\tilde{U}_m}{\tilde{P}_3} z_p = z_p \left(M_{21} + \frac{M_{22}}{z_b} \right). \end{aligned} \quad (4.17)$$

The poles of these transfer functions are the same as the eigenvalues found in Chapter 3 and represents the dynamic behavior of each compliance element in the system.

4.2.2 Piston Actuator Located Downstream of Sensing Location

The process to determine the transfer function when the sensor is located in the upstream section, A is similar to when the sensor location is in section B. Consider the system in Figure 4-3.

The perturbations created by the piston actuator are related to the sensing loca-

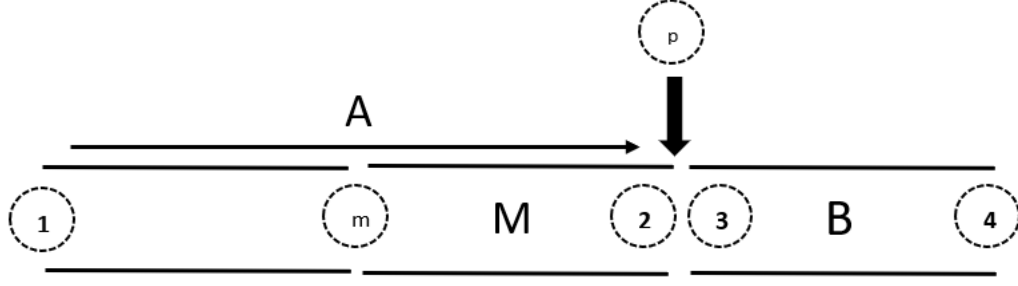


Figure 4-3: Schematic of a system with pulser located downstream of the desired transfer function location, m . Duct M and station m are located within duct A

tion with the transmission matrix, $[M]$ as follows:

$$\begin{bmatrix} \tilde{P}_2 \\ \tilde{U}_2 \end{bmatrix} = \begin{bmatrix} M_{11} & M_{12} \\ M_{21} & M_{22} \end{bmatrix} \begin{bmatrix} \tilde{P}_m \\ \tilde{U}_m \end{bmatrix}. \quad (4.18)$$

With this transmission matrix equation, $[M]$ is inverted to yield

$$\begin{bmatrix} \tilde{P}_m \\ \tilde{U}_m \end{bmatrix} = \frac{1}{|M|} \begin{bmatrix} M_{22} & -M_{12} \\ -M_{21} & M_{11} \end{bmatrix} \begin{bmatrix} \tilde{P}_2 \\ \tilde{U}_2 \end{bmatrix} \quad (4.19)$$

The 4 equations of this matrix in terms of $z_a = \frac{\tilde{P}_2}{\tilde{U}_2}$ are

$$\begin{aligned} \frac{\tilde{P}_m}{\tilde{U}_2} &= \frac{1}{|M|} (M_{22} z_a - M_{12}) \\ \frac{\tilde{P}_m}{\tilde{P}_2} &= \frac{1}{|M|} (M_{22} - \frac{M_{12}}{z_a}) \\ \frac{\tilde{U}_m}{\tilde{U}_2} &= \frac{1}{|M|} (-M_{21} z_a + M_{11}) \\ \frac{\tilde{U}_m}{\tilde{P}_2} &= \frac{1}{|M|} (-M_{21} + \frac{M_{11}}{z_a}). \end{aligned} \quad (4.20)$$

Finally the transfer function for an arbitrary point upstream of the piston actuator in terms of z_p are

$$\begin{aligned} \frac{\tilde{P}_m}{\tilde{U}_p} &= \frac{\tilde{P}_m}{\tilde{P}_2} z_p = \frac{z_p}{|M|} (M_{22} - \frac{M_{12}}{z_a}) \\ \frac{\tilde{U}_m}{\tilde{U}_p} &= \frac{\tilde{U}_m}{\tilde{P}_2} z_p = \frac{z_p}{|M|} (-M_{21} + \frac{M_{11}}{z_a}). \end{aligned} \quad (4.21)$$

Again the poles these transfer functions are the same as the free response eigenvalues and represent the dynamic behavior of each compliance element.

4.3 Transfer Function and Transmission Matrix Identification

Experimental characterization is necessary to validate the models. Instead of taking a similar approach to Brennen [3], this thesis leveraged off the work done in the "smart engine project" in the 1990's by the GTL at MIT. This project demonstrated a variety of actuation and sensing schemes which extended the stable operating range of axial compressors (see [18] for examples). The outcome of the smart engine project resulted in a control theoretical approach to the characterization of the dynamics of axial compressors. This approach is extended for characterization of the cavitation dynamics of the MIT inducer.

To characterize the one-dimensional inducer cavitation dynamics, the control theoretical approach only required a single set of upstream and downstream pressure and velocity data, and replaced the second linearly independent data set required in Brennen's approach with measurements of the unsteady velocity fluctuations by the piston actuator. This data set is used to determine four transfer functions which are then used to determine the inducer cavitation dynamics transmission matrix. The transfer functions show the dynamics cavitating inducer along with the dynamics of the rest of the test facility, whereas the transmission matrix only represents the dynamics of the inducer.

To illustrate this method, an example schematic for the implementation of sensors is shown in Figure 4-4 and an open loop block diagram representing the plant dynamics is shown in Figure 4-5.

The velocity perturbations created by the actuator are assumed to be known and represented by the input signal, $c(s)$. The cavitation dynamics of the fluid system is represented by $G(s)$, and the output signals, $y(s)$, is the inducer dynamic response

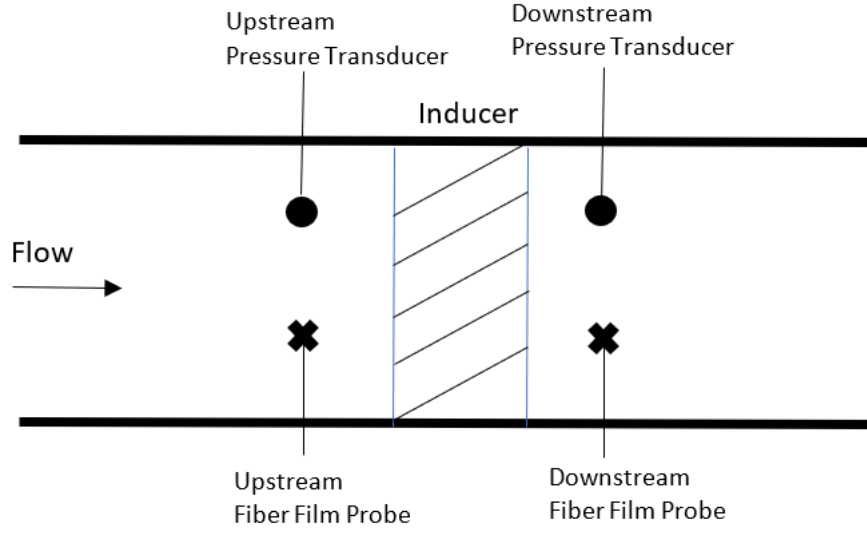


Figure 4-4: Schematic of inducer and sensors

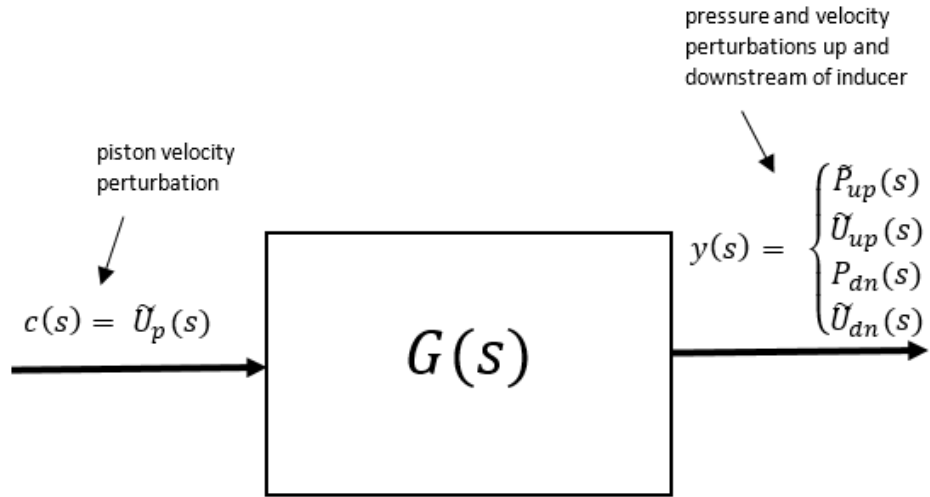


Figure 4-5: Open loop block diagram for system transfer functions

to the forcing. The inducer response is comprised of the upstream and downstream pressure and velocity perturbations, meaning that there are 4 components to the cavitation dynamics, $G(s)$ as shown in Eq. (4.22).

$$\begin{aligned}
\tilde{P}_{up}(s) &= G_{P_{up}U_p}(s)\tilde{U}_p(s) \\
\tilde{P}_{dn}(s) &= G_{P_{dn}U_p}(s)\tilde{U}_p(s) \\
\tilde{U}_{up}(s) &= G_{U_{up}U_p}(s)\tilde{U}_p(s) \\
\tilde{U}_{dn}(s) &= G_{U_{dn}U_p}(s)\tilde{U}_p(s)
\end{aligned} \tag{4.22}$$

The subscript *up* refers to the perturbations upstream of the inducer, *dn* refers to the perturbations downstream of the inducer, and *p* refers to the input forcing perturbations.

To determine the transfer functions of system dynamics, the cross spectrum of the measured input, $c(s)$, and output signal, $y(s)$, is divided by the power spectrum of $c(s)$.

$$G(s) = \frac{\Phi_{yc}(s)}{\Phi_{cc}(s)} \tag{4.23}$$

where Φ represents the Fourier transform of the correlation function and the subscripts are the signals in the correlation function.

The last step of this approach is to determine the transmission matrix. To do so, the perturbations of the inlet velocity and pressure are related to the outlet velocity and pressure. Eliminating the piston actuator velocity from Eqs. 4.22 yields:

$$\begin{aligned}
\tilde{P}_{dn}(s) &= G_{P_{dn}U_P}(s)G_{P_{up}U_p}^{-1}(s)\tilde{P}_{up}(s) \\
\tilde{P}_{dn}(s) &= G_{P_{dn}U_P}(s)G_{U_{up}U_p}^{-1}(s)\tilde{U}_{up}(s) \\
\tilde{U}_{dn}(s) &= G_{U_{dn}U_P}(s)G_{P_{up}U_p}^{-1}(s)\tilde{P}_{up}(s) \\
\tilde{U}_{dn}(s) &= G_{U_{dn}U_P}(s)G_{U_{up}U_p}^{-1}(s)\tilde{U}_{up}(s)
\end{aligned} \tag{4.24}$$

where the plant dynamics of the inducer are

$$\begin{aligned}
G_{P_{dn}P_{up}}(s) &= G_{P_{dn}U_P}(s)G_{P_{up}U_P}^{-1}(s) \\
G_{P_{dn}U_{up}}(s) &= G_{P_{dn}U_P}(s)G_{U_{up}U_P}^{-1}(s) \\
G_{U_{dn}P_{up}}(s) &= G_{U_{dn}U_P}(s)G_{P_{up}U_P}^{-1}(s) \\
G_{U_{dn}U_{up}}(s) &= G_{U_{dn}U_P}(s)G_{U_{up}U_P}^{-1}(s).
\end{aligned} \tag{4.25}$$

Notice that $G_{P_{dn}P_{up}}, G_{P_{dn}U_{up}}, G_{U_{dn}P_{up}}, G_{U_{dn}U_{up}}$ are similar to the pressure gain, impedance, compliance, and mass flow gain terms defined by Brennen [3]. As such the transmission matrix of a cavitating inducer can be expressed as

$$\begin{bmatrix} \tilde{P}_{dn} \\ \tilde{U}_{dn} \end{bmatrix} = \begin{bmatrix} G_{P_{dn}P_{up}}(s) & G_{P_{dn}U_{up}}(s) \\ G_{U_{dn}P_{up}}(s) & G_{U_{dn}U_{up}}(s) \end{bmatrix} \begin{bmatrix} \tilde{P}_{up} \\ \tilde{U}_{up} \end{bmatrix}. \quad (4.26)$$

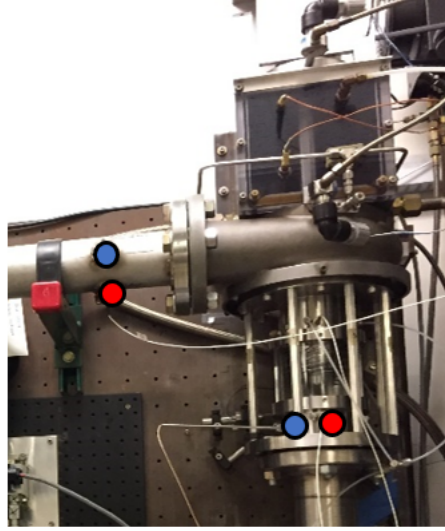
Chapter 5

Model Based Design of Force Response Experiment

The necessary modifications such that the inducer test facility was suitable for forced response testing included the addition of a gas accumulator, the addition of a piston actuator, and the determination of the sensor locations. The gas accumulator was used to ensure that the inducer pressure and velocity response to the piston pulse velocity remained linear, but with a sufficiently high signal to noise ratio. The effect of each modification, i.e. accumulator size and location, were determined by performing several parametric studies using the forced response model. These trade studies were then used with manufacturing timelines and physical constraints to determine a recommended test facility design.

5.1 Sensor Locations

Figure 5-1 shows the location of the sensors in the inducer test facility. The upstream fiber film probe was placed 1.14 inducer diameters upstream of the inducer tip plane while pressure transducer was placed 1 diameter upstream of the inducer tip plane. For ease of manufacturing the downstream sensors were placed 1.7 inducer tip diameters downstream of the pump housing instead of immediately downstream of the inducer. Because this downstream sensor location also measured the dynamics of the



● Pressure Transducer ● Fiber Film Probe

Figure 5-1: Pressure transducer and fiber film probe locations around the inducer

inducer housing, simulated transfer functions at this location were compared with the transfer functions located at a point upstream of the housing, but downstream of the inducer. It was found that there was minimal difference between the transfer functions of these two locations.

5.2 Example Forced Response Model Implementation

Because multiple trade studies were conducted, there were multiple implementations of the forced response model that simulated the inducer test facility dynamic behavior. As such this section provides an example walk through on how to determine the four pressure and velocity transfer functions. The configuration of the test facility in this walk through is shown in Figure 5-2 where the accumulator was placed downstream of the discharge duct and the piston was placed at the midpoint of the discharge duct. The upstream sensors were assumed to be placed immediately upstream of the inducer, and the downstream sensors were assumed to be immediately downstream

of the pump housing. Table 5.1 is a modified version of Table 3.2 that reflects these changes.

Because the piston is located downstream of the inducer, the appropriate transfer function equations were derived in Section 4.2.2. The same nomenclature (matrices A , B , and M as in Figure 4-3) is carried through, however, since both the upstream and downstream sensor locations are desired, there are 2 sets of transfer function equations and thus 2 M matrices. M^{up} is used to find the upstream perturbations and M^{dn} is used to find the downstream perturbations. Figure 5-2 illustrates which components belong to matrix A , M^{up} , M^{dn} and B .

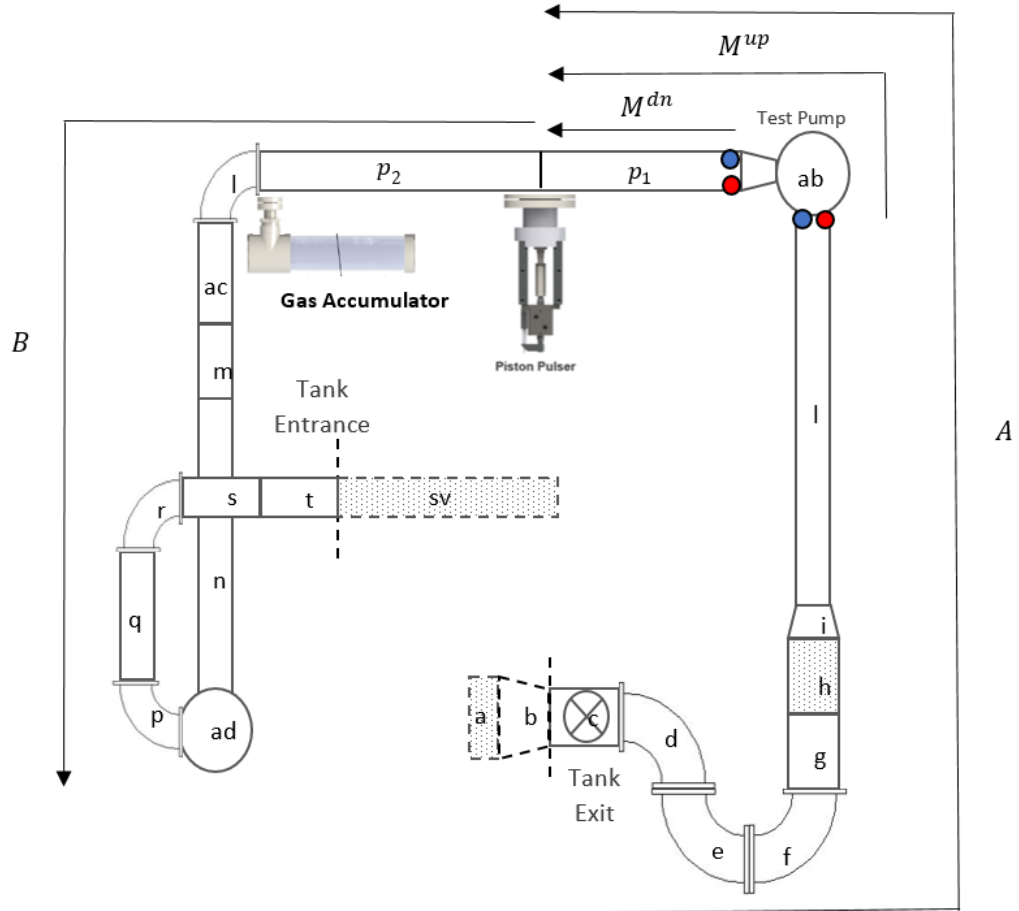


Figure 5-2: Schematic for forced response derivation

Table 5.1: Inducer Test Facility Components and Non-Dimensional Resistances and Inertances for Example Forced Response Model Implementation

Element Number	Element	Element Description	Resistance ($\times 10^{-4}$)	Inertance
1	a	Inlet Flow Straightener	2.94	0.19
2	b	Tank Entrance	75.88	0.45
3	c	6" Ball Valve	3.81	4.67
4	d	90 Degree Elbow	20.55	4.87
5	e	90 Degree Elbow	20.55	4.87
6	f	90 Degree Elbow	20.55	4.87
7	g	Bellows	3.06	3.76
8	h	Inlet Flow Conditioner	2054.05	4.25
9	i	Inlet Contraction	822.04	3.02
10	l	Inlet Line Vertical Section	368.04	51.77
11	ab	Pump Housing from Inducer Exit to Discharge Flange	84502.29	25.89
12	p1	Discharge Line Horizontal Straight Section Upstream of Piston Actuator	359.11	59.12
13	p2	Discharge Line Horizontal Straight Section Downstream of Piston Actuator	359.11	59.12
14	l	90 Degree Elbow	328.82	8.77
15	ac	Section Between Elbows	113.62	18.70
16	m	45 Degree Elbow	219.21	18.70
17	n	Section Between Elbow and Boost Pump	446.35	73.48
18	ad	90 Degree Elbow	328.81	8.78
19	p	90 Degree Elbow	328.81	8.78
20	q	Section Between 90 Degree Elbow	146.08	8.78
21	r	90 Degree Elbow	328.81	8.78
22	s	Section Between Elbow and sv Ball Valve	109.56	18.04
23	t	Discharge Line Ball Valve Straight Section	64.92	10.69
24	sv	Porous Flow Control Valve	189484.9	8.78

Each section of the test facility is stacked together such that

$$[A] = \prod_{n=11}^{12} \begin{bmatrix} 1 & -L_n s - R_n \\ 0 & 1 \end{bmatrix} [TF]_{inducer} \prod_{n=1}^{10} \begin{bmatrix} 1 & -L_n s - R_n \\ 0 & 1 \end{bmatrix} \quad (5.1)$$

$$[B] = \prod_{n=14}^{24} \begin{bmatrix} 1 & -L_n s - R_n \\ 0 & 1 \end{bmatrix} \begin{bmatrix} 1 & 0 \\ -sC_{accum} & 1 \end{bmatrix} \prod_{n=13}^{13} \begin{bmatrix} 1 & -L_n s - R_n \\ 0 & 1 \end{bmatrix} \quad (5.2)$$

$$[M^{up}] = \prod_{n=11}^{12} \begin{bmatrix} 1 & -L_n s - R_n \\ 0 & 1 \end{bmatrix} [TF]_{inducer} \quad (5.3)$$

$$[M^{dn}] = \prod_{n=12}^{12} \begin{bmatrix} 1 & -L_n s - R_n \\ 0 & 1 \end{bmatrix}. \quad (5.4)$$

Applying these matrices to Equations 4.21, the pressure and velocity transfer functions upstream of the inducer are

$$\begin{aligned} \frac{\tilde{P}_m}{\tilde{U}_p} &= \frac{\tilde{P}_m}{\tilde{P}_2} z_p = \frac{z_p}{|M^{up}|} (M_{22}^{up} - \frac{M_{12}^{up}}{z_a}) \\ \frac{\tilde{U}_m}{\tilde{U}_p} &= \frac{\tilde{U}_m}{\tilde{P}_2} z_p = \frac{z_p}{|M^{up}|} (-M_{21}^{up} + \frac{M_{11}^{up}}{z_a}) \end{aligned} \quad (5.5)$$

and the transfer functions for the location of downstream of the inducer are

$$\begin{aligned} \frac{\tilde{P}_m}{\tilde{U}_p} &= \frac{\tilde{P}_m}{\tilde{P}_2} z_p = \frac{z_p}{|M^{dn}|} (M_{22}^{dn} - \frac{M_{12}^{dn}}{z_a}) \\ \frac{\tilde{U}_m}{\tilde{U}_p} &= \frac{\tilde{U}_m}{\tilde{P}_2} z_p = \frac{z_p}{|M^{dn}|} (-M_{21}^{dn} + \frac{M_{11}^{dn}}{z_a}). \end{aligned} \quad (5.6)$$

z_p is the drive point impedance

$$z_p = \frac{z_a z_b}{z_a - z_b} \quad (5.7)$$

and with an open-open boundary condition

$$\begin{aligned} z_a &= \frac{A_{12}}{A_{22}} \\ z_b &= -\frac{B_{12}}{B_{11}} \end{aligned} \tag{5.8}$$

5.3 Perturbation Limits

Because the modeling framework of this thesis assumed that higher order terms were negligible, careful consideration was taken to ensure that the forced response magnitudes were in the linear regime. Ng had shown that if the amplitude of the fluctuating mass flow rate was larger than 5-6% of the mean flow, the velocity responses would fall out of the linear regime. At this forcing amplitude, the velocity response amplitudes were found up to 3% of the mean flow rate [15]. That value was adopted as the upper limit for the velocity perturbations of this thesis.

Similarly, an upper bound was needed for the inlet pressure perturbation as the modeling effort does not account for the effect of the inducer inlet pressure perturbations on the inlet cavitation number. As such the model set the limit of the inlet pressure perturbation to be no more than 30% of the steady cavitation number as that is the same value found by Ng in the experiments carried out at Caltech [15].

To convert these limits to a form similar to the output of the forced response model, in Eqs (5.5), the limits were divided by the piston velocity fluctuations. The piston actuator was set to create velocity perturbations with a magnitude of 5% of the mean flow velocity, thus the non-dimensional velocity perturbation of the piston is

$$\tilde{U}_p = 0.05\phi \tag{5.9}$$

where ϕ is the steady non-dimensional flow rate. With an inlet pressure perturbation that cannot exceed 30% of steady cavitation number, $\bar{\sigma}$,

$$\begin{aligned}
\tilde{P} &= 0.3\bar{\sigma} \\
\frac{\tilde{P}}{\tilde{U}_p} &= \frac{0.3\bar{\sigma}}{0.05\phi} \\
\frac{\tilde{P}}{\tilde{U}_p} &= 6\frac{\bar{\sigma}}{\phi}
\end{aligned} \tag{5.10}$$

and with $\phi = 0.06$ the upper limit inlet pressure perturbation is

$$\frac{\tilde{P}}{\tilde{U}_p}/\bar{\sigma} = 100. \tag{5.11}$$

Because inlet velocity perturbation cannot exceed 3% of the steady flow rate,

$$\begin{aligned}
\tilde{U} &= 0.03\phi \\
\frac{\tilde{U}}{\tilde{U}_p} &= \frac{0.03\bar{\sigma}}{0.05\phi}
\end{aligned} \tag{5.12}$$

the velocity perturbation upper limit is

$$\frac{\tilde{U}}{\tilde{U}_p} = 0.6. \tag{5.13}$$

Due to the lack of experience using fiber film probes in water, prior tests were conducted to ensure that the fiber film probes could capture the dynamic velocity measurements. The fiber film probes were used to measure the velocity perturbations during cavitation surge and showed good agreement in terms of phase with the mass flow measurements captured optically¹ as seen in Figure 5-3. To ensure that the same performance was observed in the forced response experiments, a lower limit was set for the velocity perturbations using this data.

The lower velocity perturbation limit was found by determining the background noise of cavitation surge velocity measurements. The data was collected at a volumetric flow coefficient of $\phi = 0.06$. The surge mode as well as its second and third harmonics were digitally filtered out using bandstop filter between 0.045 and 0.420 rotor frequency. The lower limit was determined by taking the difference between

¹Cavitation surge oscillations were derived from time accurate optical data (video recordings) analyzing the number of pixels inside the vapor cavities

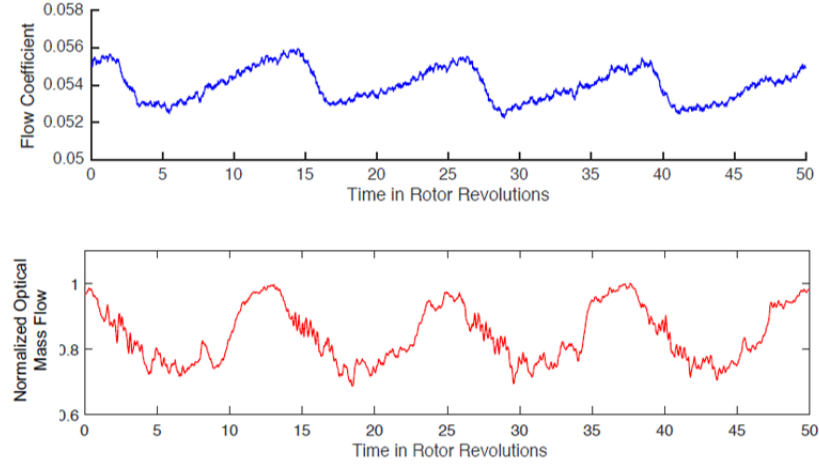


Figure 5-3: Velocity measurement captured with a single fiber film probe compared to normalized optical mass flow rate shows good matching between the two sensors [19]

the filtered velocity data's RMS value from the averaged filtered velocity. The found perturbation limit relative to the piston perturbation strength is

$$\frac{\tilde{U}}{\tilde{U}_p} = 0.2. \quad (5.14)$$

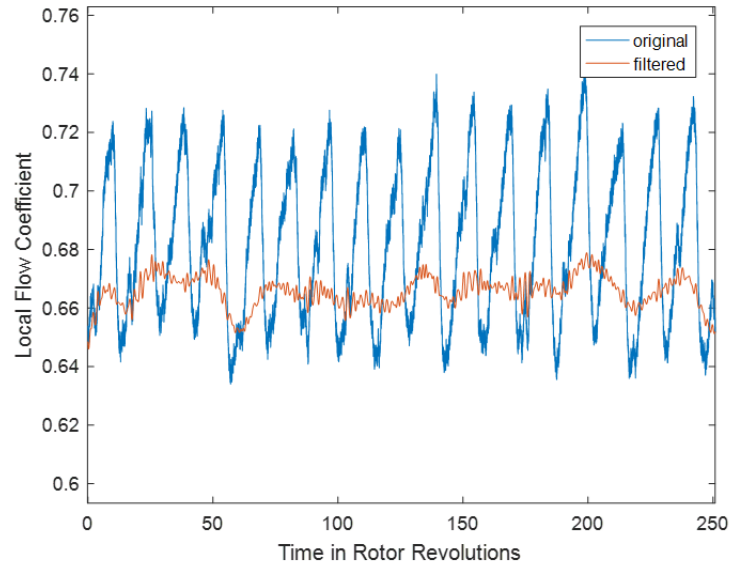


Figure 5-4: Raw and filtered cavitation surge velocity captured with fiber film probe

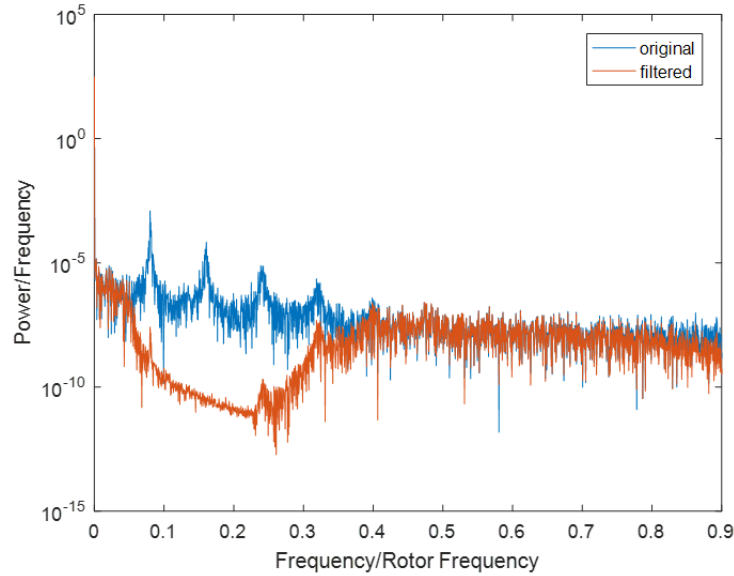


Figure 5-5: Power spectral density plots of raw and filtered cavitation surge velocity data shows surge dynamics were filtered out of fiber film data

5.4 Component Trade Studies

Figure 5-9 shows that without an accumulator the magnitude of the cavitation surge mode was much larger than what was allowed by the linearity requirement. To reduce this, an accumulator was added to increase the damping of the system. The addition of the accumulator added a pair of complex poles and zeros into the model of the test facility, where the frequency and damping of these poles and zeros determined the exact effect it had on the cavitation surge poles. To create a transfer function where the poles of both the accumulator and cavitation surge dynamics are within the perturbation limits, but also produces 2 identifiable peaks required careful placement of the pole zero pairs. Tuning of these poles and zeros was done by controlling physical parameters relating the accumulator size, and location. To determine how the accumulator will interact with the dynamics of the rest of the test facility this thesis performed trade studies on the:

- Piston location
- Accumulator location

- Accumulator compliance
- Accumulator resistance and inertance

The results of these studies were used to determine the recommended configuration of the test facility. The desired transfer functions would have bode plots similar to the cartoon in Figure 5-6 over the test conditions $\phi = 0.06$ and $\sigma = 0.02 - 0.1$. The red dashed line refers to the upper limits, and the black dashed lines refers to the lower limit.

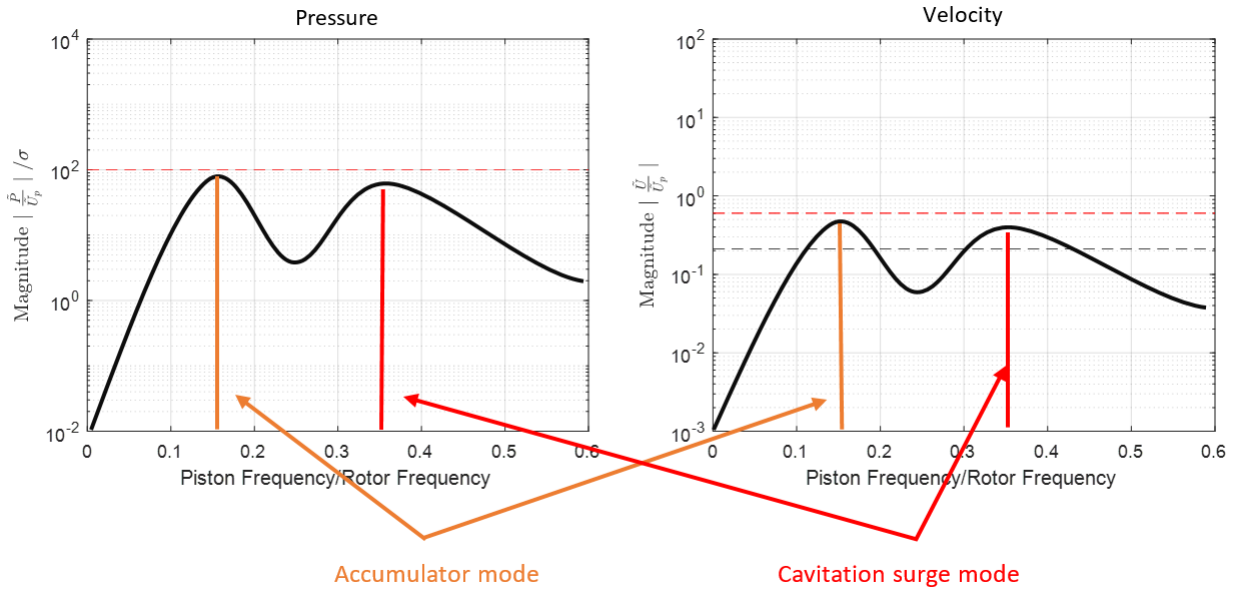


Figure 5-6: Cartoon of desired transfer function bode plots: Pressure (left) and Velocity (right)

5.4.1 Effect of Piston Location on System Transfer Functions

The first key design choice of the forced response model was determining the location of the piston relative to the inducer. Physical limitation of the inducer test facility only allowed for the piston to be placed between 0-12 inducer diameters upstream of the inducer tip plane and between 0-8 diameters downstream of the inducer housing. This restriction was set because of the available mounting surface of the optics table as shown in Figure 5-7.

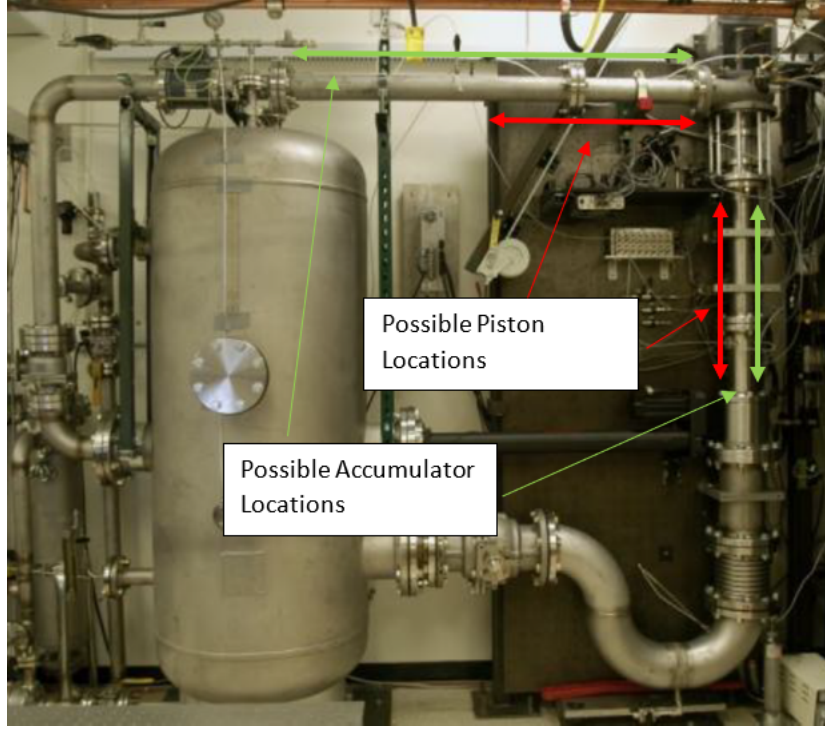


Figure 5-7: Weight of the piston requires its placement location to depend on mounting availability on optics table. The lighter weight of the accumulator allows for its larger placement area.

Simulations using the forced response model showed that placing the piston upstream of the inducer resulted in larger perturbation magnitudes, and an additional zero as compared to placing the piston downstream of the inducer. A more detailed system mode shape can be created with the former configuration, however, because the goal of the forced response experiment is to identify the pole corresponding to the cavitation surge mode the additional zero was not desired. As such the configuration with the piston downstream of the inducer was carried forward, as it had overall smaller amplitude perturbations and had a larger design space for the accumulator where the transfer functions would fit within the perturbation limits.

To illustrate these effects, the transfer functions for two different piston configurations were found. Both configurations had the piston located 8 diameters away from the inducer, one downstream of the inducer housing, and the other upstream. Figure 5-8 shows the schematics of two configurations with the sensor locations.

Simulated at $\phi = 0.06$ and $\sigma = 0.03$, the bode plots of the upstream pressure

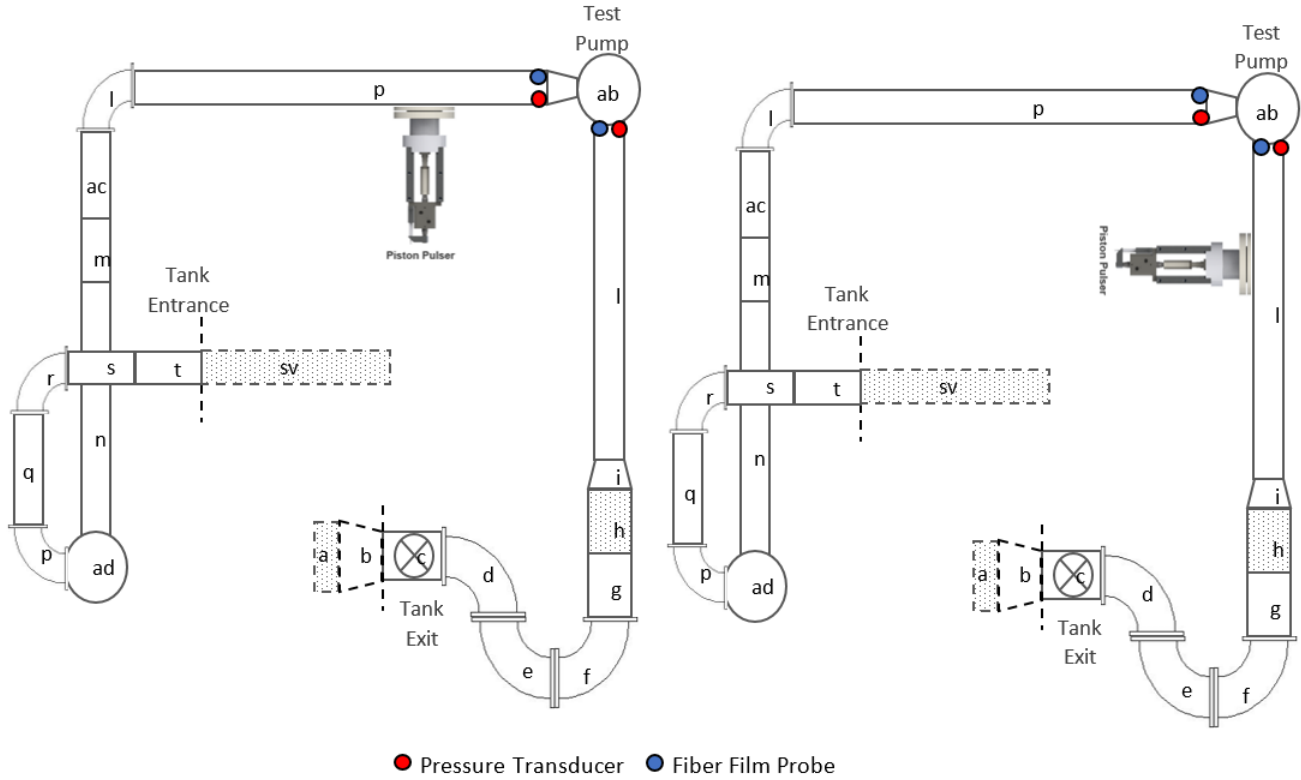


Figure 5-8: Schematics for piston location trade study: Piston upstream of inducer (right), Piston downstream of inducer (left)

perturbation transfer function are shown in Figure 5-9. The bode plots for the velocity and downstream pressure transfer functions similarly show the larger perturbation magnitudes and additional zero when the piston was placed upstream of the inducer. Those plots are located in Appendix C. The peak of the bode plots represents the cavitation surge mode, the red dashed lines are the upper perturbation limits, and the black dashed lines are the lower perturbation limits.

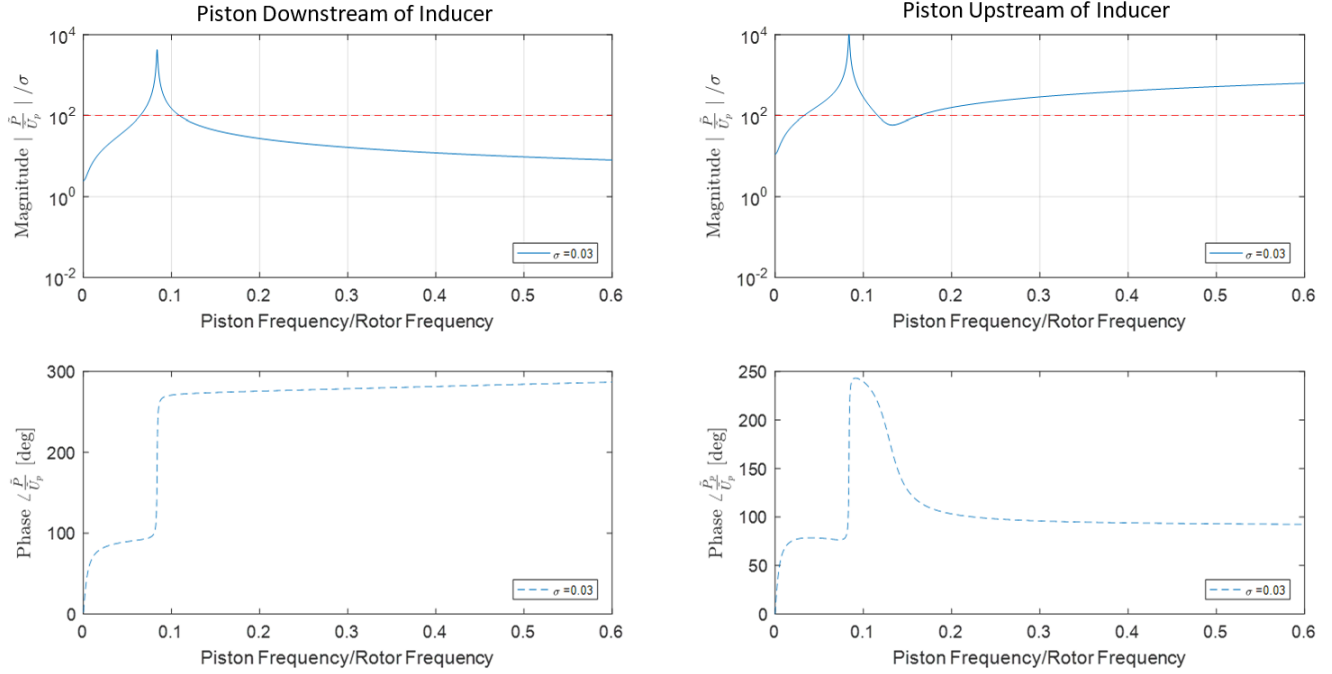


Figure 5-9: Comparison of upstream pressure transfer function, at $\phi = 0.06$ and $\sigma = 0.03$, shows when piston is placed upstream of inducer, larger magnitude responses are found. Piston placed downstream of inducer (right), Piston placed upstream of inducer (left)

5.4.2 Effect of Accumulator Location on System Transfer Functions

After anchoring the location of the piston to be downstream of the inducer, the location of the accumulator was determined. There were several possible accumulator locations of interest to investigate. Three configurations were considered:

1. Accumulator upstream of the inducer, in the inlet ducting
2. Accumulator downstream of the inducer, but upstream of the piston
3. Accumulator downstream of the inducer, and downstream of the piston

The three locations of the accumulator are shown in Figure 5-10.

Because the piston was limited where it can be placed downstream of the inducer, the configuration with the accumulator located between the inducer and the piston

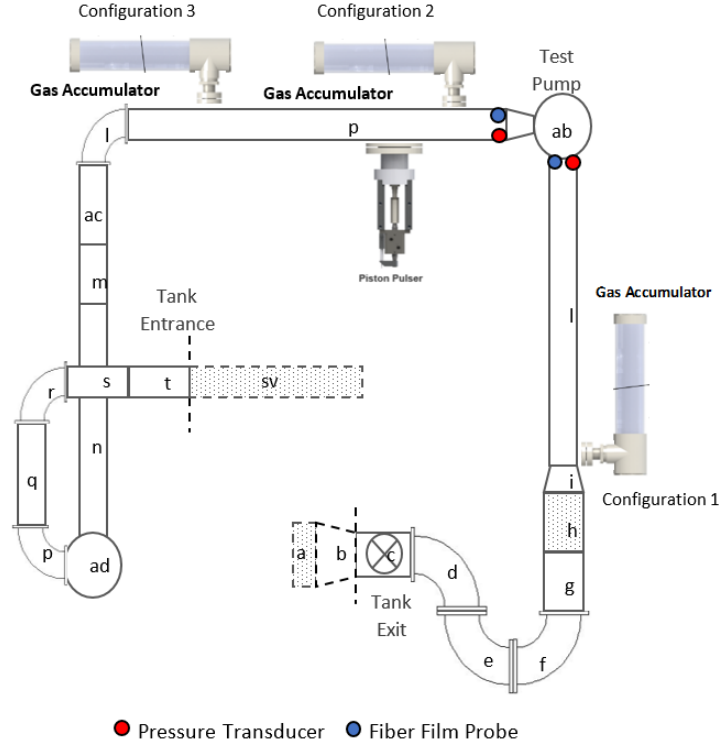


Figure 5-10: Schematic showing accumulator locations for different possible configurations

required the two compliance elements be physically close together. Additionally because the minimum measurable volume of the accumulator was much larger than the cavitation void volume, the dynamics of accumulator compliance dominated the cavitation surge mode in the forced response plots. This effect is seen in Figure 5-11 as there is only one observable peak for this configuration as opposed to two for the other configurations. This co-location of modes would make it difficult to experimentally identify separately and as such this configuration was not suggested.

Because other two configurations had the two compliance elements separated further apart, they both had an easily identifiable accumulator mode. Both accumulator locations also successfully increased the damping of the cavitation surge mode, thus reducing its magnitude. However, because of the accumulator's relative location to the piston and the amount of inertance separating the inducer with the accumulator, the two configurations have different effects on the cavitation surge mode, accumulator natural frequencies, and accumulator damping ratios for the same compliance.

These differences caused configuration 3 to have overall smaller magnitudes which allowed for more flexibility with accumulator sizing. Placing the accumulator downstream of the inducer housing and piston actuator also required less modifications in terms of new ducting, tees, and mounting supports. As such this configuration was recommended.

To illustrate these effects, Figure 5-11 contains the bode plots of the upstream pressure transfer function of all the 3 configurations. For the all 3 configurations the piston was held at the same location, 8 diameters downstream of the inducer. The first configuration placed the accumulator 12 diameters upstream of the inducer, the maximum distance allowed by physical constraints. The second configuration placed the accumulator equidistant between the inducer housing and accumulator, 4 diameters downstream of the inducer housing. The last configuration placed the accumulator 18 diameters downstream of the inducer housing, the maximum distance allowed by size constraints. The accumulator had the same compliance value of $C = 3.3$ for each configuration.

Within configuration 3, it was found that changing ratio of the distance between the piston with the accumulator against the distance between the piston with the inducer moved the zero in the forced response transfer functions. As the ratio changed such that the accumulator was closer to the piston then the accumulator peak increased in magnitude. The opposite was also found where as the ratio was changed such that the inducer was closer to the piston, the inducer peak was increased. A cartoon is shown in Figure 5-12.

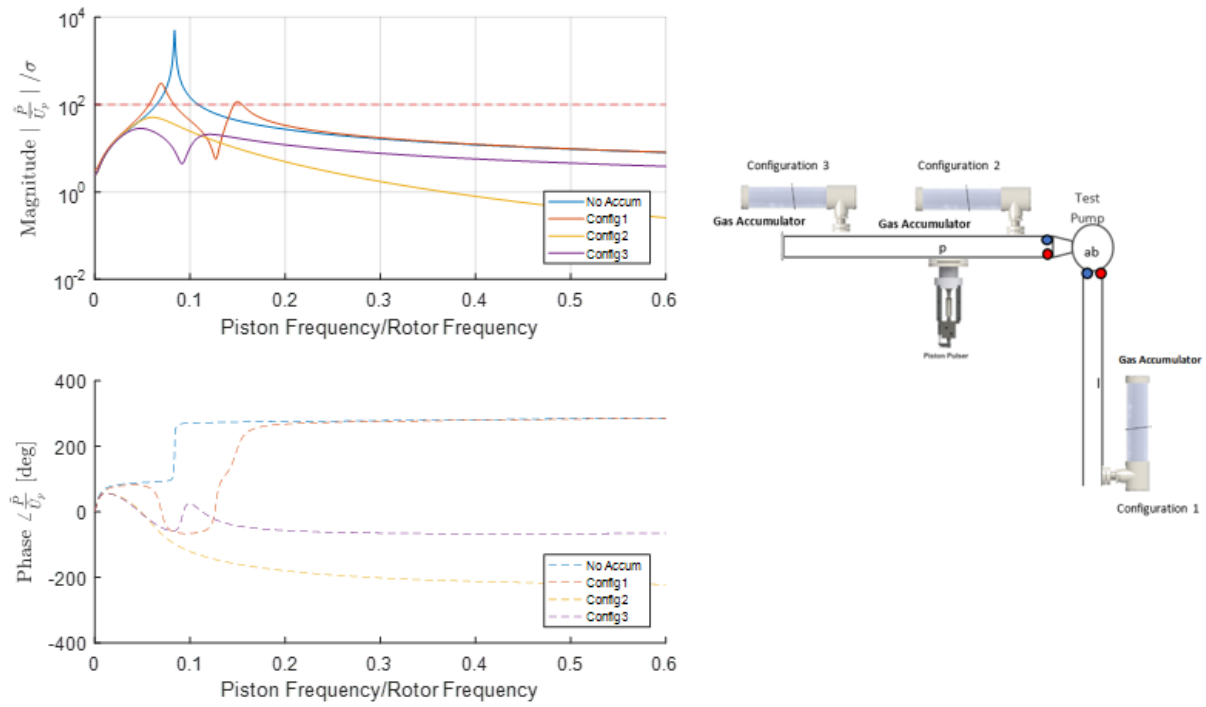


Figure 5-11: Comparison of upstream pressure transfer function, at $\phi = 0.06$ and $\sigma = 0.03$, shows when accumulator is placed near the inducer, the two modes overlap. Placing the accumulator downstream of the piston and inducer results in smaller perturbation magnitudes

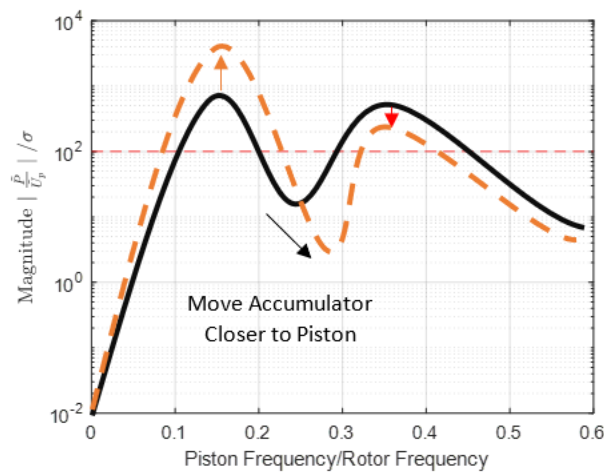


Figure 5-12: Cartoon showing that as piston is moved closer to the accumulator, the zero moves away from the accumulator peak resulting in a larger magnitude

5.4.3 Effect of Accumulator Compliance on System Transfer Functions

The natural frequency of an accumulator is inversely related to its compliance, and as such the accumulator can be tuned such that it has a large or little influence on the cavitation surge mode based on how close the accumulator frequency is to the cavitation surge frequency. However, as the accumulator poles near the cavitation surge poles, the peaks two compliance elements would overlap, and identification of each pole becomes difficult.

To illustrate how the compliance of the accumulator affects the system dynamics, a simulation using the forced response model was performed that placed the accumulator 18 inducer diameters downstream of the inducer housing and placed the piston 8 diameters downstream of the housing. The configuration of the test facility for this study is shown in Figure 5-13. The simulation had operated the test facility at $\sigma = 0.03$ and at $\phi = 0.06$ as the accumulator had its non-dimensional compliance varied from 0.2 to 18.6.

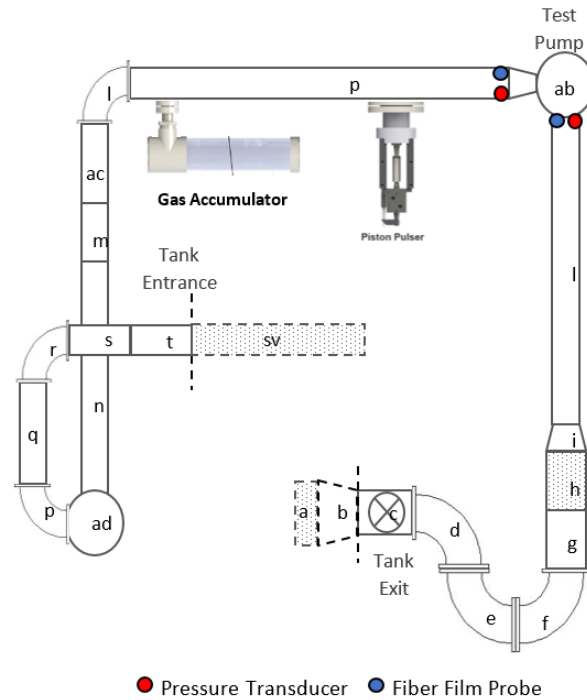


Figure 5-13: Schematic for accumulator compliance and resistance trade study

Figure 5-14 shows the simulation results and shows that as the compliance of the accumulator was increased, the accumulator pole's frequency decreased. The figure also shows that as the accumulator pole moved to frequencies much larger or smaller than the cavitation surge pole the less effect the accumulator had on dampening the cavitation surge mode. This agrees with intuition, as a very small accumulator would act as a duct with nearly no compliance, and a large compliance would effectively shorten the system by appearing to be an open boundary. However, an interesting takeaway from this study was that as the accumulator pole approached the cavitation surge pole, it "repelled" the cavitation surge pole, by causing the cavitation surge frequency to change. Figure 5-15 summarizes these effects in an cartoon.

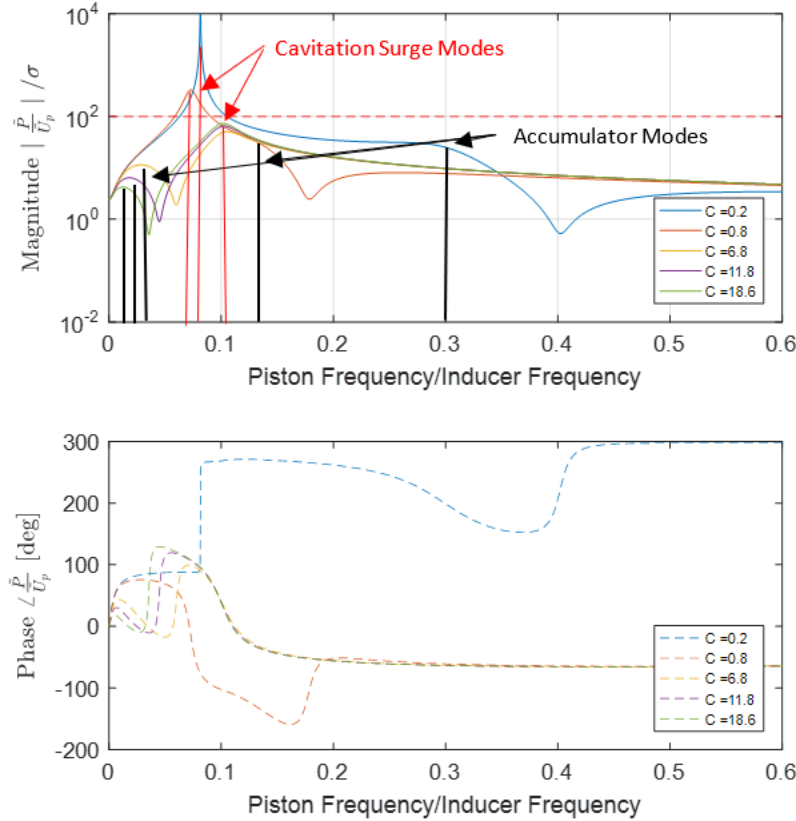


Figure 5-14: Accumulator mode natural frequency is inversely proportional to the accumulator compliance: upstream pressure transfer function, $\sigma = 0.03$, $\phi = 0.06$

Though the cavitation surge pole moves as the as the accumulator frequency was changed, the two frequencies still overlapped for some accumulator compliance values.

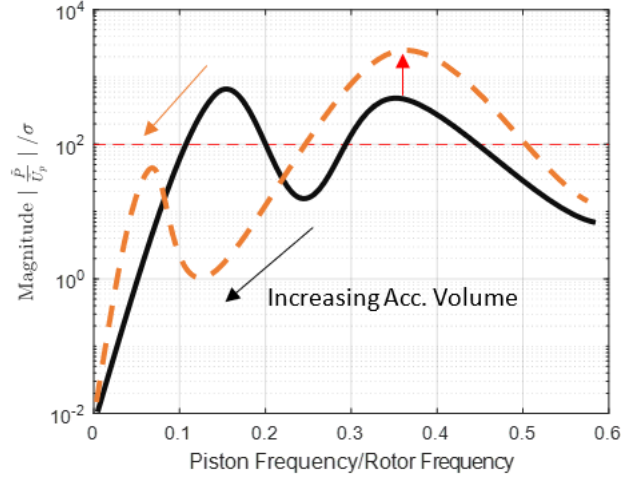


Figure 5-15: Cartoon showing that as accumulator volume increases, the accumulator peak moves to lower frequency and the cavitation surge frequency increases in magnitude

In the instance where the two poles co-locate one large peak will be seen. The forced response model can identify the corresponding poles, but to do so experimentally would be difficult. As such the value of the accumulator compliance was chosen to avoid this overlapping. Figure 5-16 illustrates the co-located compliance modes for the upstream pressure transfer function.

For the recommended design, the compliance of the accumulator was chosen such that it would sufficiently dampen the cavitation surge amplitude, but not such that the accumulator frequency overlapped with the cavitation surge frequency.

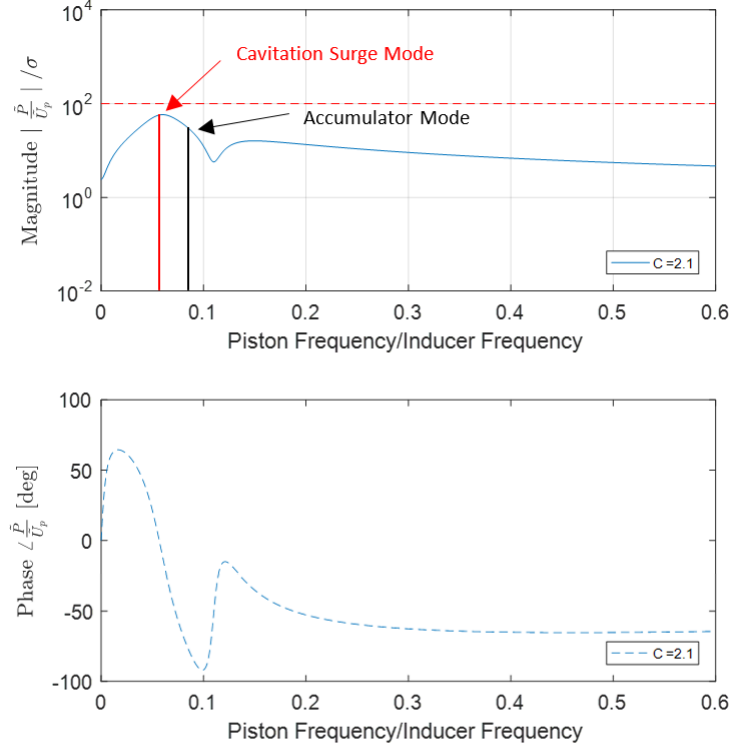


Figure 5-16: Accumulator mode is tuned to similar frequency as inducer cavitation surge mode. The poles are difficult to identify from each other: upstream pressure transfer function, $\sigma = 0.03$, $\phi = 0.06$, $C_{accum} = 2.1$

5.4.4 Effect of Accumulator Resistance on System Transfer Functions

The accumulator used in this thesis was assumed to be a gas accumulator teed off of the main flow. Because the length of the device parallel with the mean flow was small, and because there was no mechanism to slow the flow it was assumed that the accumulator had no resistance. However, this would not reflect reality, so to verify that some resistance would not greatly affect the modeling effort, a trade study varying the accumulator resistance was performed. The configuration of the test facility in this study was the same as with the compliance trade study, but the compliance was fixed to be $C = 3$, and accumulator resistance was added.

Figure 5-17 shows bode plots of the upstream pressure transfer function for this study. The resistance was varied between 0 and 18 where the value of 18 corresponds to the resistance of the porous media valve, the largest resistance value in the test

facility. This value was chosen since it would represent an unrealistically large upper bound for the accumulator as the porous media valve controls the mean flow through the entire facility.

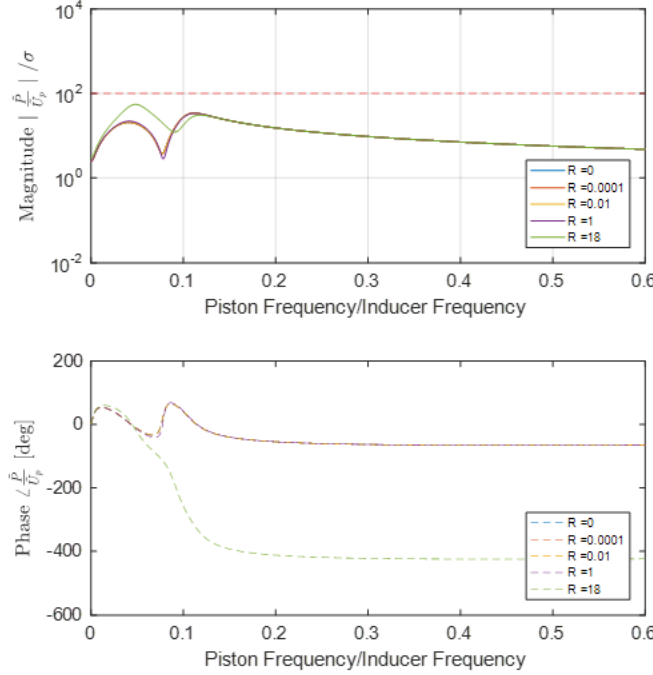


Figure 5-17: Accumulator resistance, unless nearing the resistance levels of the porous media valve, has little effect on the upstream pressure perturbation transfer function: $\sigma = 0.03$, $\phi = 0.06$, $C_{accum} = 3$

The result of this trade study shows that as long as the accumulator had a resistance in the same order of magnitude as a duct or an elbow and not in the order of magnitude to that of the porous media valve, the accumulator resistance would not affect the overall model.

5.5 Recommended Design for Modified Inducer Test Facility

The trade studies presented illustrated how the size and placement of the accumulator and piston changed the poles and zeros of the forced response model. Because this thesis is interested in the cavitation dynamics over a range of cavitation numbers

the learning from these trade studies were used to design the inducer test facility over the inlet conditions of $\sigma = 0.02 - 0.1$ and $\phi = 0.06$. However, due to the large cavitation surge frequency over this cavitation number range, a single configuration could not be proposed that satisfied both the pressure and velocity perturbation limits. Instead two configurations were suggested, one for low cavitation numbers ($\sigma = 0.03 - 0.04$), and another for higher cavitation numbers ($\sigma = 0.04 - 0.1$). To reduce the amount of manufacturing required, the difference between the two recommended configurations was chosen to be only be the accumulator compliance, where the accumulator of the low cavitation configuration had a compliance of $C = 8.25 - 8.67$, and the accumulator of the high cavitation configuration had a compliance of $C = 2.9 - 3.3$. The compliance value varied because the accumulator was designed such that the volume remained constant. However, since the static pressure of the accumulator must match the static pressure of the test facility, and that static pressure of the test facility varies with cavitation number the compliance cannot be constant. A schematic of the recommended test facility is shown in Figure 5-18. The accumulator is located 18 diameters downstream of the inducer housing, and the piston is located 8 downstream of the inducer housing.

Figure 5-19 contains the bode plots of the pressure and velocity transfer functions upstream of the inducer using the low cavitation number configuration. Cavitation numbers between $\sigma = 0.03 - 0.04$ are within the perturbation magnitude limits. An additional configuration can be used with even smaller compliance values such that there would be sufficiently high signal to noise ratio for cavitation numbers below $\sigma = 0.03$, but the dimensional volume associated with those compliance values are physically difficult to set.

Figure 5-20 contains the bode plots of pressure and velocity transfer functions upstream of the inducer using the high cavitation number configuration. This configuration's transfer functions are within or at the perturbation limits for the cavitation numbers $\sigma = 0.04 - 0.1$.

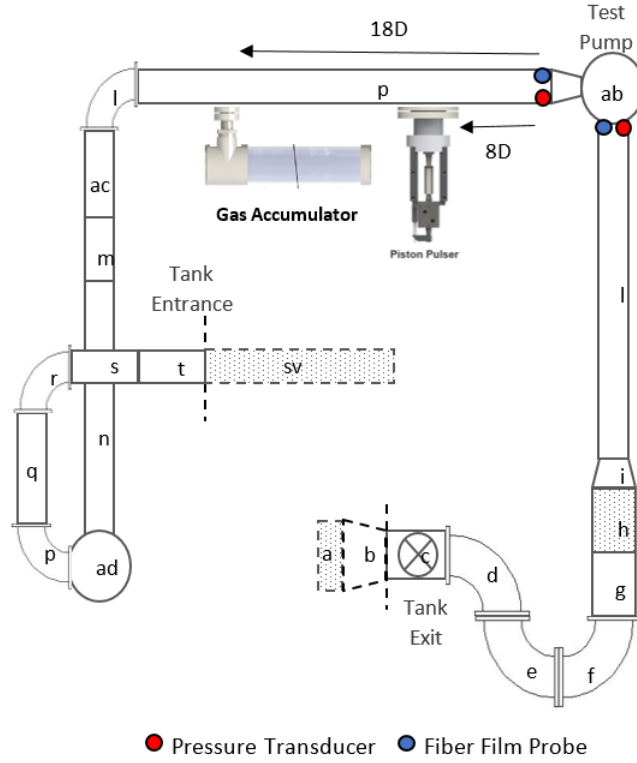


Figure 5-18: Schematic for recommended modification for inducer test facility

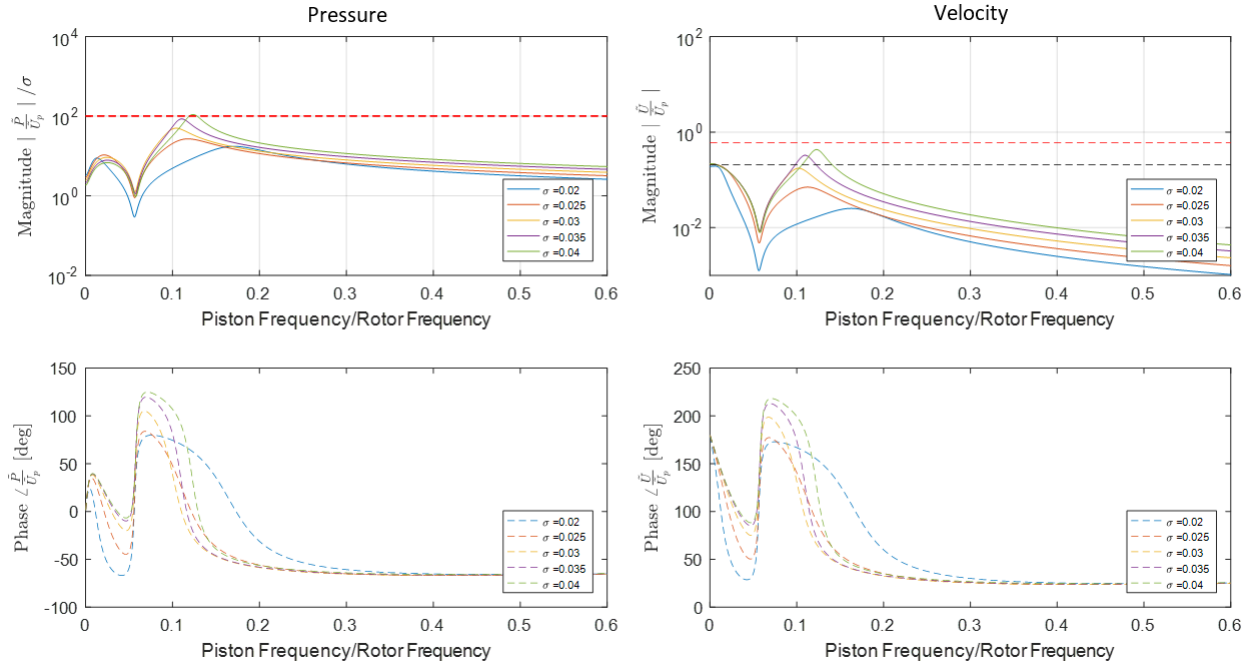


Figure 5-19: Bode plots of upstream pressure (left) and velocity (right) perturbation transfer functions are within perturbation limits: Recommended configuration of inducer test facility for low cavitation number flows, $\sigma = 0.03 - 0.04$, $\phi = 0.06$

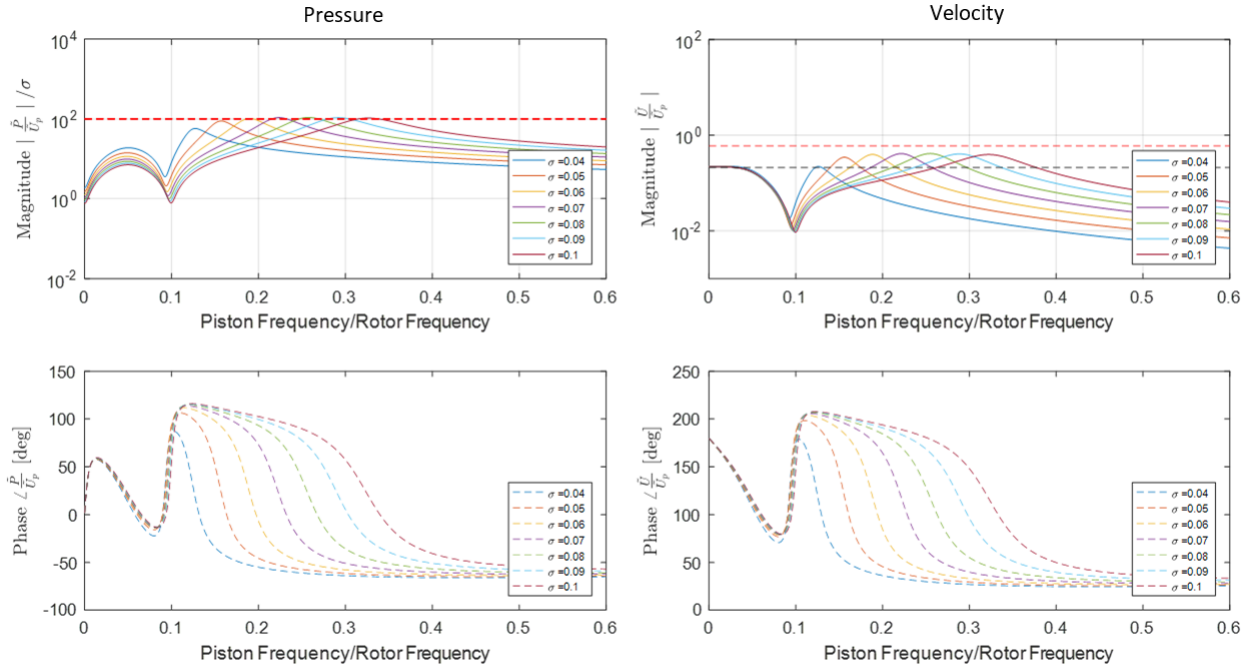


Figure 5-20: Bode plots of upstream pressure (left) and velocity (right) perturbation transfer functions are within perturbation limits: Recommended configuration of inducer test facility for high cavitation number flows , $\sigma = 0.04 - 0.1$, $\phi = 0.06$

Chapter 6

Cavitating Inducer Forced Response Testing

The first set of forced response tests excited the structural modes of the inducer test facility and thus the transfer functions captured both the cavitation and structural dynamics. The structural modes observed in the forced response tests were corroborated with acceleration data collected from impact hammer testing of the inducer test facility. Modal analysis of this acceleration data indicated that the sources of these modes arose from flexible structural components. This chapter describes how changes to the test facility created unintended vibrations of the piping and support structure. It then provides guidelines on how to avoid these vibrations and valuable lessons learned.

6.1 Forced Response Experimental Setup

The inducer test facility described in Chapter 3 was modified for forced response testing using the designs recommended in Section 5.5. A gas accumulator and piston actuator were added downstream of the inducer by cutting the downstream duct and adding stainless steel tees. However, to reduce the required manufacturing tolerances needed for the tees and ducting pieces, a stainless steel bellows was added downstream of the gas accumulator. Additionally to increase the manufacturing speed, the section

of ducting connecting the piston tee with the accumulator tee was made from PVC components. Figure 6-1 and 6-2 shows an image of the modified test facility along with a schematic with the divided downstream duct.

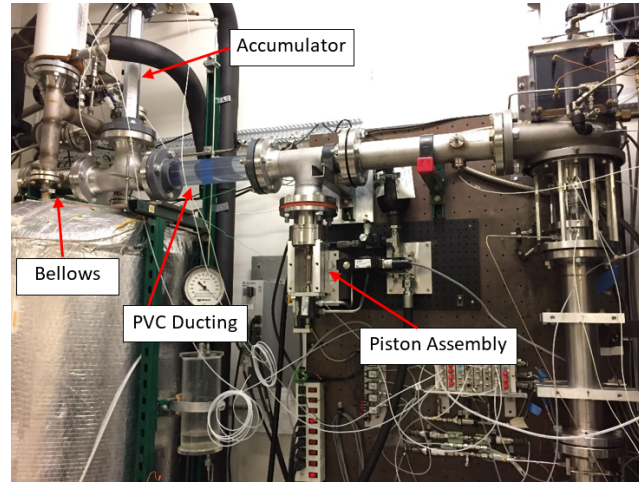


Figure 6-1: Inducer test facility modified with gas accumulator, stainless steel bellows, piston actuator, and PVC ducting

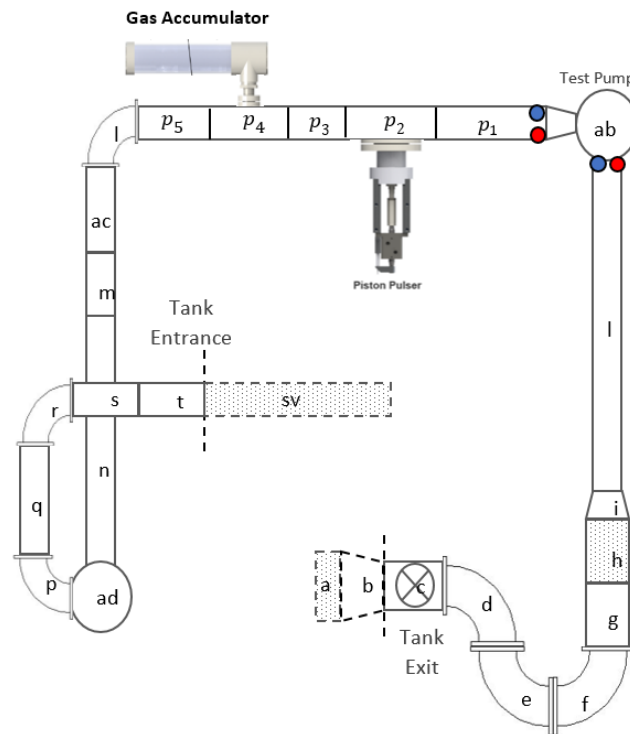


Figure 6-2: Schematic of Inducer Test Facility modified with Piston Actuator p_2 , PVC ducting p_3 , Gas Accumulator p_4 , and Stainless Steel Bellows p_5

6.1.1 Sensors

As with the free response testing, the forced response tests utilized dynamic pressure transducers to measure the pressure response and used fiber film probes to measure the velocity response. As mentioned in Section 5.1, the upstream fiber film probes were placed 1.14 inducer diameter upstream of the tip plane, whereas the upstream pressure transducers were placed 1 diameter upstream. The downstream pressure and fiber film probes were placed 1.7 diameters downstream of the inducer volute.

The pressure transducers were Entran diaphragm pressure transducers. They had a 3.8mm diameter pressure sensitive area and were flush mounted to the test facility. The transducers were externally calibrated to determine their voltage output sensitivity to changes in the pressure. However, these pressure transducers were also sensitive to the fastening torque, so there is low confidence in the steady portion of pressure measurement.

The Dantec fiber film probes are able to measure the local flow velocity based on the convective cooling of a thin heated wire through the working principle of constant temperature anemometry. Assuming a constant fluid temperature and uniform medium, the heat transfer is controlled by the film temperature and the fluid velocity. Thus the measured temperature and power input is used to calculate the velocity. However, due to the lack of a water tunnel, the probes needed to be calibrated in-situ before every test. A detailed explanation on the calibration and operation of the fiber film probes is shown in Appendix D.

6.1.2 Accumulator Design

The forced response modeling indicated that multiple accumulator compliances were required to cover the large test envelope. A water-gas column design was used for the accumulator. The column was connected to a vacuum pump and a compressed air source, so that the volume of the accumulator can be varied. Figure 6-3 shows a sketch of this design. The accumulator was connected to the test rig using a stainless steel tee, but the accumulator itself was made from PVC components. The accumulator

was made from 2" diameter schedule 40 piping, which caused the accumulator to be long and skinny. The accumulator tee was simply supported such that the weight of the tee was supported, but was allowed to oscillate in the other directions.

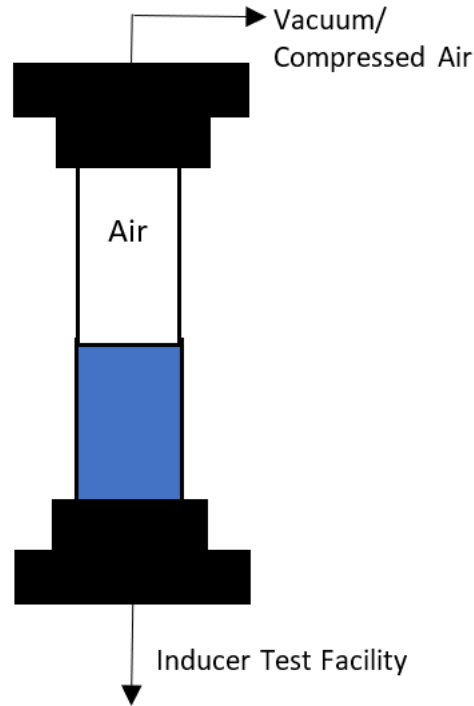


Figure 6-3: Cartoon of Accumulator Design

6.1.3 Piston Actuator

The piston actuator used for the forced response experiments was purchased commercially from Parker Hannifin. A hydraulic power unit powered the piston. A proportional valve was used to controlled the piston operation. The signal input of the proportional valve and the measurement of the cylinder stroke position was interfaced through a Delta motion controller. The stroke position was measured using an LVDT and was captured by a high speed DEWEsoft DAQ. The piston head was 76.2mm (3in) in diameter and had a stroke length of 17mm (0.67in). A cutout of the piston assembly is shown in Figure 6-4. The piston assembly was fixed to the optics table with custom stainless steel mounts, and the piston tee was supported by resting

on a crossbar that was attached to the optics table.

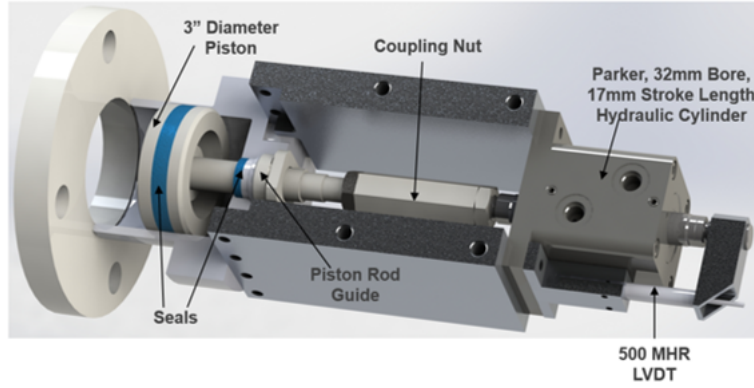


Figure 6-4: Cross section of piston assembly [8]

6.1.4 Forcing Signal

A linear chirp signal was used as the fluctuating velocity pulse. The signal had a non-dimensional frequency range from 0 to 0.6 rotor frequency. This range was chosen as it spanned the simulated cavitation surge frequency, and accumulator natural frequency. The piston velocity perturbation magnitude was set at 5% of the mean flow velocity. This value was chosen because Ng [15] had found that linearity assumption for their mass flow fluctuations only allowed a maximum piston perturbation magnitude of 6%, and that smaller amplitudes would have weaker signal to noise ratios. The 5% magnitude was chosen as a compromise between the two requirements, however, if given more time further testing could have taken place such that this amplitude was tuned to optimize the signal to noise ratio, while avoiding exciting undesired responses. The rate at which the frequency of the linear chirp signal increased was set using the recommended ramp rate found by Hackenberg and Hartung [7]. They found that to properly excite any mode of the system with a transient sweep, the maximum ramp rate of the sweep, \dot{f} , should not exceed

$$\dot{f} \leq \zeta^2 \omega_n^2 \quad (6.1)$$

where ζ is the critical damping coefficient of the pole, and ω_n is the natural

frequency of the pole. The poles corresponding to cavitation surge found in the recommended test facility designs were used to determine the appropriate ramp rate. During the forced response experiment, the chirp signal was repeated 5 times. This was done so that the unsteady pressure and velocity response to the forcing signal can be time averaged to reduce noise.

6.2 Analysis of Structural Modes

The forced response test was thought to have had excited structural modes of the test facility, and induced perturbations that were measured with the sensors. This was hypothesized because transfer functions with multiple poles and a zero were measured no matter the test facility setup or test conditions. The forced response test results are shown in more detail in Section 6.2.1. The hypothesis was corroborated with hammer tap tests that identified the structural dynamics of the test facility and identified the source for each structural mode. The findings from the hammer tap tests are covered in detail in Section 6.2.2.

Figure 6-5 compares data between the forced response test and the hammer tap test and shows that the pressure transfer function had captured the same structural dynamics found in the hammer tap test. The transfer function was measured with the pressure transducer upstream of the inducer and is overlaid with the magnitude of the imaginary portion of the frequency response functions (FRF) found from hammer tap tests. The FRFs were determined using accelerometers placed on the outside of the test facility. The pressure transfer function and the hammer tap test FRFs were collected under the same operating conditions, zero flow at atmospheric pressure, and no gas in the accumulator. There are two FRFs shown in Figure 6-5 which were collected from two separate tests. One with the hammer and sensor located at the inducer housing - stainless steel ducting flange, and another with the hammer and sensor located at the bellows - accumulator tee flange. See Figure 6-8. This was necessary as the two hammer locations had excited different modes of the test facility.

At the lower frequency range of Figure 6-5, the forced response transfer function

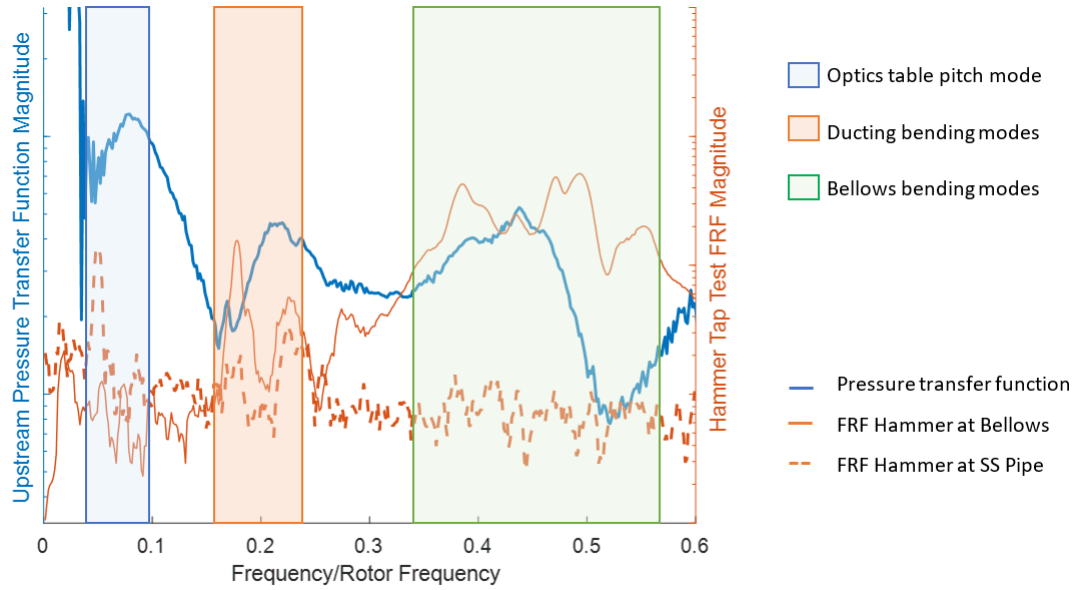


Figure 6-5: Pressure transfer function overlaid with hammer tap test data shows similar resonant frequencies. Confirms that the forced response test can measure the structural dynamics of the test facility

and the hammer tap test data both measured the optics table pitch mode, at 0.05 rotor frequency for the hammer tap tests and at 0.08 rotor frequency for the forced response test. Both also measured ducting bending modes at 0.18 and 0.22 rotor frequency for the hammer tap test, and at 0.17 and 0.21 rotor frequency for the forced response test. This mismatch in frequencies was thought to be because the hammer tap test data required two different tests to see these two modes. As such the hammer tap test FRFs do not capture the interaction between these modes and thus could have different frequencies. This effect also explains why there was an anti-resonance in the the pressure transfer function at 0.16 rotor frequency, but not in the hammer tap test data. Lastly, the higher frequency range from 0.3 to 0.6 rotor frequency was also captured between the two data sets. The hammer tap test had found a number of modes in this range, where as the pressure transfer function had found a single mode in this range. Because the forced response test had a pulsating sweep, it was thought that multiple modes were excited simultaneously and caused the structural modes to manifest in a single peak in the transfer function.

6.2.1 Analysis of Forced Response Transfer Functions

Pressure and velocity data was collected during a series of forced response experiments where the dynamics of the test facility was changed. The different experiments included tests where the inducer spun at 4000 rpm or in remained a static position, and with and without compliance in the accumulator. During these tests the upstream and downstream pressures along with the upstream velocity was measured. The transfer functions were determined from this data, but none of the fluid modes predicted in Chapter 5 were observed. The measured transfer functions were hypothesized to have been influenced by structural dynamics, because the different experiments resulted in transfer functions with similar shapes. Additionally as the experiments were altered, the transfer functions did not respond as expected. For instance the addition of compliance into the accumulator did not create an additional response peak. This hypothesis was further supported as the forced response transfer function of a static system was shown to have measured the structural modes of the test facility, in Figure 6-5.

Figure 6-6 compares the measured pressure transfer function of the test facility operating in a static configuration, zero mean flow at atmosphere with a static inducer, with the transfer function of the test facility operating in a cavitating configuration, $\phi = 0.06$ and $\sigma = 0.05$ with the inducer spinning at 4000 rpm. The accumulator was completely full such that there was no accumulator compliance for both tests.

Figure 6-6 indicates that the structural dynamics were being measured with a some influence from the cavitation dynamics. The transfer function for the static configuration is the same as in Figure 6-5 in Section and was shown to have captured the structural dynamics as measured by the hammer tap tests. As the inducer was spun up, and the test facility began to operate in cavitation conditions, the profile of the transfer function remained similar. The optics table mode at 0.08 rotor frequency and the anti-resonance at 0.16 rotor frequency remained in both tests, but there were more measured dynamics at frequencies greater than 0.2 rotor frequency. This was thought to have been caused by the cavitation dynamics as that was the only variable

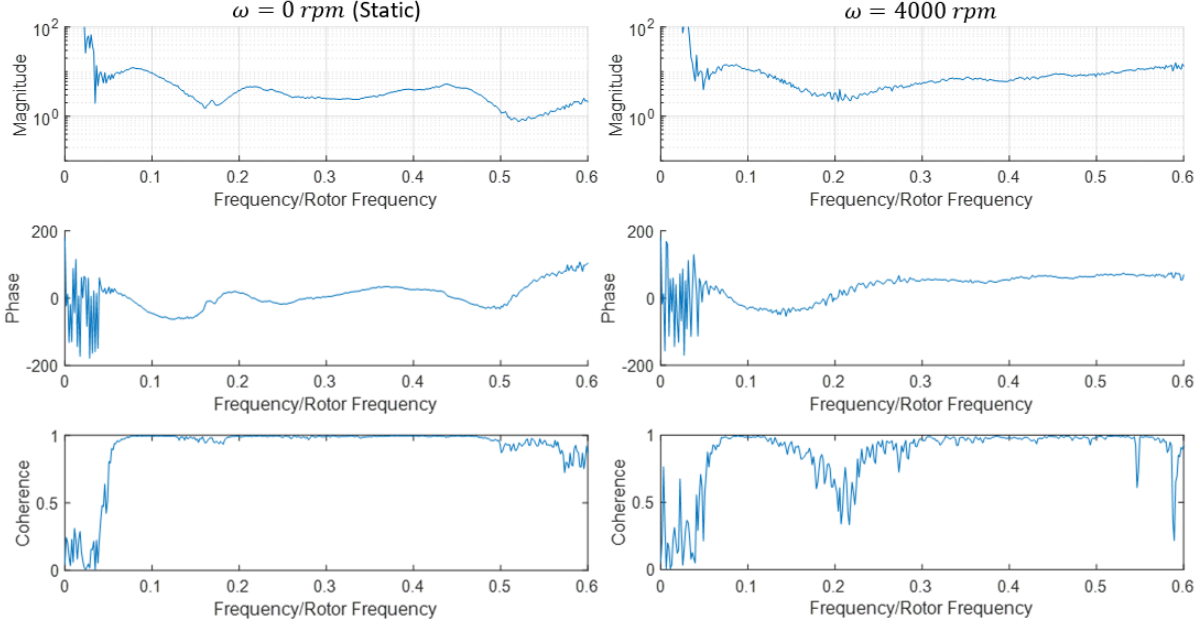


Figure 6-6: Similar measured upstream pressure transfer functions regardless of flow condition indicated that the mode shape is heavily influenced by the structural dynamics: No Flow, static inducer (left); Inducer running at $\phi = 0.06, \sigma = 0.05$ (right)

changed between the two tests. However, because there were also structural dynamics in that frequency range, peaks were difficult to identify.

Figure 6-7 compares the pressure transfer functions of the test facility operating in a static configuration, zero mean flow at atmosphere with a static inducer, and operating at a cavitating configuration, $\phi = 0.06$ and $\sigma = 0.1$ with the inducer spinning at 4000 rpm. For this comparison, the accumulator had a gas volume and thus had compliance.

Again the cavitation dynamics were seen, possibly as a highly damped pole at 0.3 rotor frequency similar to the simulated pole at 0.34 rotor frequency. However, when compared to Figure 6-6 both transfer functions in Figure 6-7 reacted in an unexpected manner to the addition of accumulator compliance. Both had shifted the zero to a lower frequency instead of adding an additional peak. This effect was thought to be caused by the accumulator dynamics interacting with the structural dynamics.

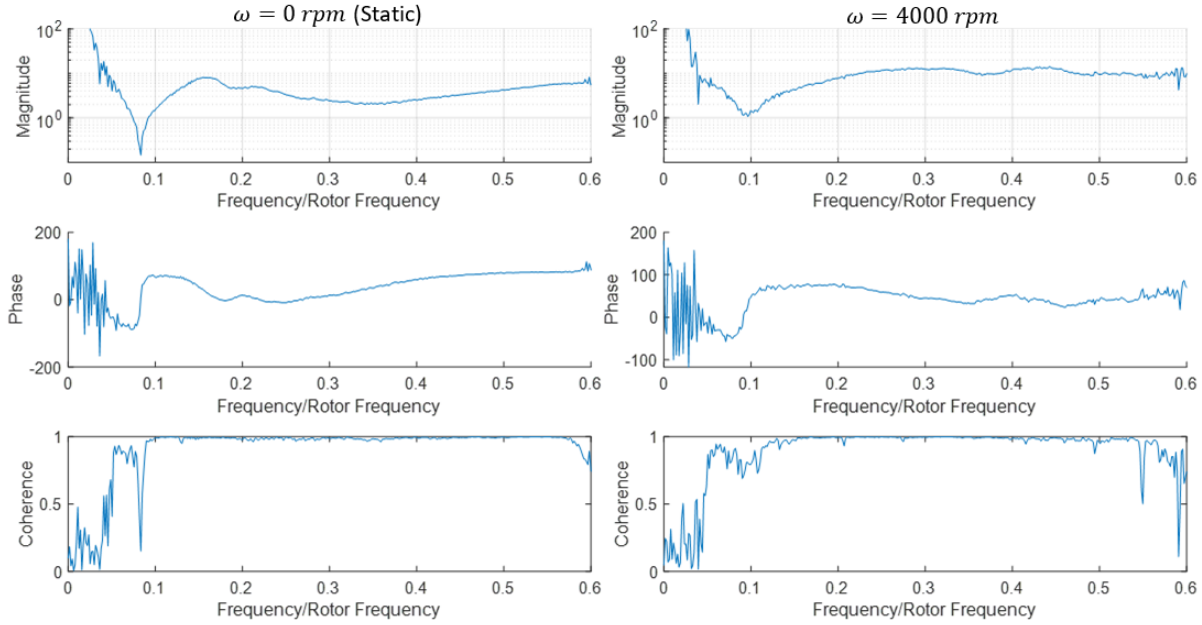


Figure 6-7: The addition of accumulator compliance did not add a peak, but had shifted the anti-resonance: No Flow, static inducer (left); Inducer running at $\phi = 0.06, \sigma = 0.1$ (right)

6.2.2 Analysis of Hammer Tap Test Frequency Response Functions

A series of hammer tap tests were conducted where the hammer and sensor locations were on the flanges of the bellows, accumulator tee, piston tee, and stainless steel pipe in the downstream section of the inducer test facility. Figure 6-8 shows the the locations on a picture of the test facility.

Because hammer tap tests are susceptible to having the forcing signal damped out due to the structure, two sets of tests were used to determine the resonant frequencies, FRFs, and mode shapes. From these two sets of data similar resonant frequencies to the ones found from the pressure and velocity forced response transfer functions were identified and the causes of each frequency were sourced to the flexibility of structural components. The two hammer tap test data sets differ by the location of hammer tap location, where the first test occurred at the stainless steel pipe-inducer housing flange, and the second occurred at the bellows-accumulator tee flange.

The imaginary portion of each sensors' FRF and sensor location the averaged FRF

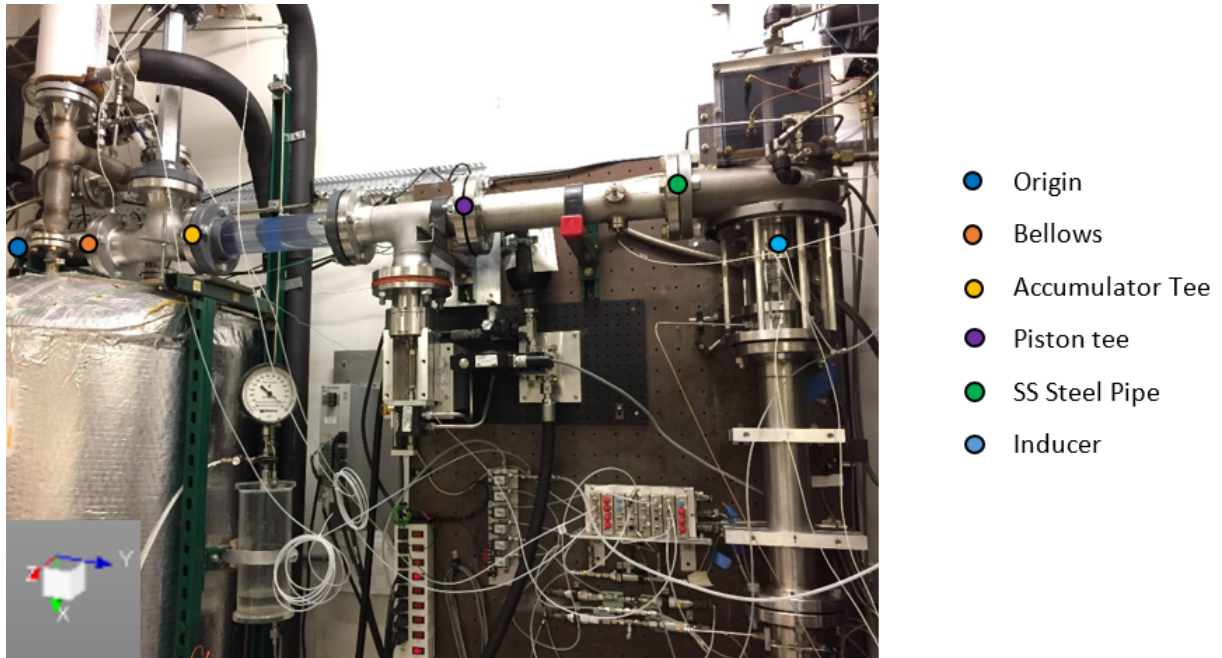


Figure 6-8: Hammer and sensor locations of the hammer tap tests

are shown in Figure 6-9. A resonant frequency at 0.05 rotor frequency was observed in both FRFs, so the mode shape for this frequency was found from the FRFs at each sensor location as shown in Figure 6-10. The mode shape overlaid a cartoon of the downstream portion of the test facility is shown in Figure 6-11.

From Figure 6-11, the deflection at all sensor locations are the same magnitude and phase except for a node at the flange connecting the bellows with the pipe that connects to the storage tank. At this location, there is a steel fixture connected to the storage tank that supports the piping, and it was thought that this support kept this sensor location rigid. The other sensor locations either had supports that were fixed to the optics table or were not supported at all. Because of the support configuration and that the measured mode shape had deflections in phase of the same magnitude it was concluded that this structural mode was the result of the optics table pitch motion (motion in the Z direction from Figure 5-1). This was further supported with prior measurements of the pitch mode frequency. The 0.05 rotor frequency dimensionalized is 3.3Hz which is similar to the value of 2Hz that Ehrlich had found for the unmodified inducer test facility [6]. Modifications to the structure and test

facility for forced response testing was assumed to cause the difference between the two measurements.

The data from the bellows-accumulator flange hammer location was used in a similar manner to the previous data. The different sensor FRF's were averaged and overlaid each other to determine the resonant frequencies, shown in Figure 6-12. From the sensor overlaid plots, resonant frequencies were found at 0.18, 0.22, 0.38, 0.44, 0.47, 0.50, and 0.56 rotor frequency.

The mode shapes for the 0.18 and 0.22 resonant frequencies showed profiles that were not easily identified to a structural element of the system. These mode shapes appeared to be bending or rigid body modes of the ducting, however these frequencies are smaller than what one would expect from the natural vibration frequency of a fixed-fixed duct. As such it was hypothesized that the structural flexibility of the bellows, and along with the multiple fixtures resulted in the complicated mode shapes. This hypothesis was corroborated by some evidence, as there was only one location in the downstream portion of the test facility where the ducting was restricted from moving, and that location was found to have a node within all the mode shapes, Figure 6-17. The mode shape found for the resonant frequency 0.18 is shown in Figure 6-13, and the mode shape for the 0.22 resonant frequency is shown in Figure 6-15. These mode shapes overlaid a cartoon of the test facility are shown in Figures 6-14 and 6-16.

The 0.38, 0.44, 0.47, 0.50, and 0.56 resonant frequency mode shapes all indicated that the source of these modes was the flexibility of the bellows and accumulator tee support. The mode shape for the 0.44 frequency is shown in Figure 6-18 and is plotted over a cartoon of the test facility in Figure 6-19. The other resonant frequencies are found in Appendix E.

From Figures 6-19, there were large deflections on the unsupported side of the bellows, and the accumulator-PVC ducting flange while the deflection magnitudes were zero on the stainless steel structural components and the supported side of the bellows. This indicates that the bulk of the motion is caused by the flexibility of the bellows, and the simply supported accumulator tee.

6.3 Inducer Test Facility Design Guidelines

From the comparison of the pressure and velocity transfer functions with the FRF captured from the hammer tap tests, it was found that the structural dynamics of the test facility were inducing fluid perturbations measured by the pressure transducers and fiber film probes. These structurally induced perturbations had distorted the transfer functions and made characterization of the inducer cavitation behaviour not possible. It was found that these perturbations were the result of motion caused by the optics table, bellows, and accumulator tee. As such the most beneficial modification for the test facility is to replace the bellows with a stainless steel pipe. This would reduce and remove many of the resonant frequencies above 0.18 rotor frequency, and limit the pitching motion of the optics table. Additionally, it is advised that the support of the accumulator tee be modified such that it fixes the tee in place, a support be applied to the accumulator such that it is not allowed to oscillate during the forced response experiment, and a support is applied to the optics table to further limit its pitching motion.

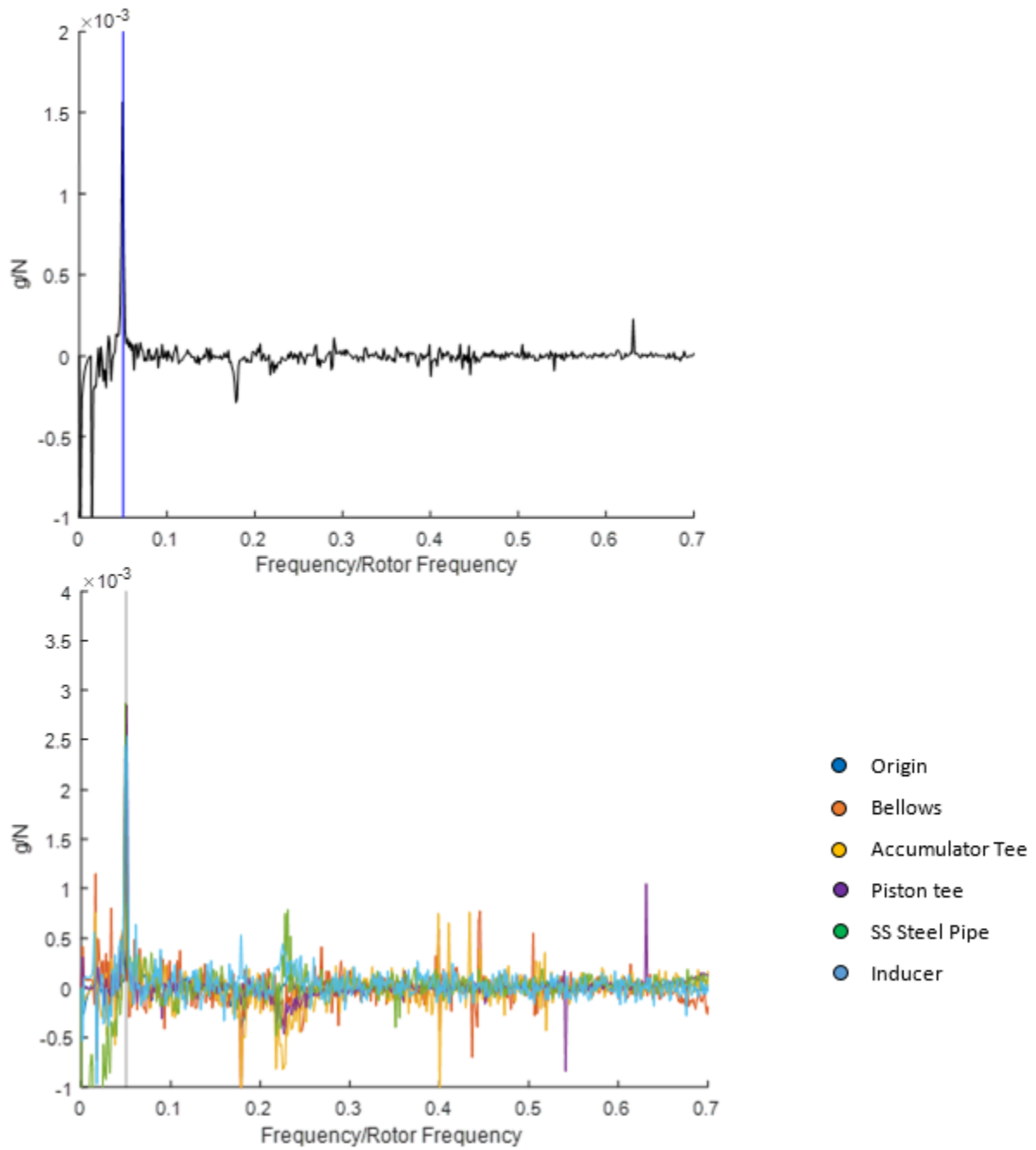


Figure 6-9: Both the sensor averaged FRF and overlaid sensor FRFs shows resonant frequencies at 0.05 rotor frequency. Hammer tap location at inducer housing-stainless steel pipe flange

Optics Table Pitch mode

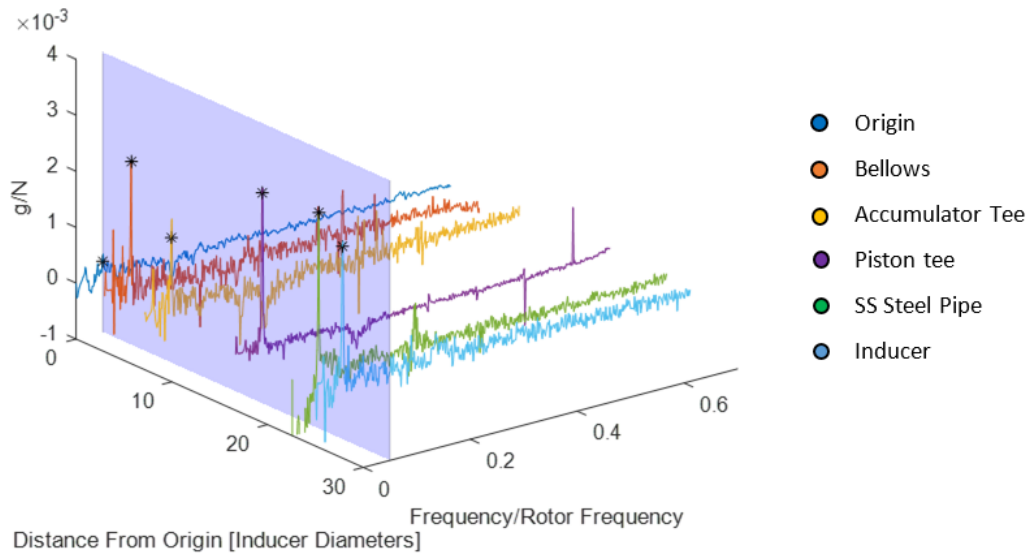


Figure 6-10: The 0.05 rotor frequency mode shape is generated by obtaining the magnitude of the imaginary portion of the FRF at each sensor location. Each location has the same magnitude and phase.

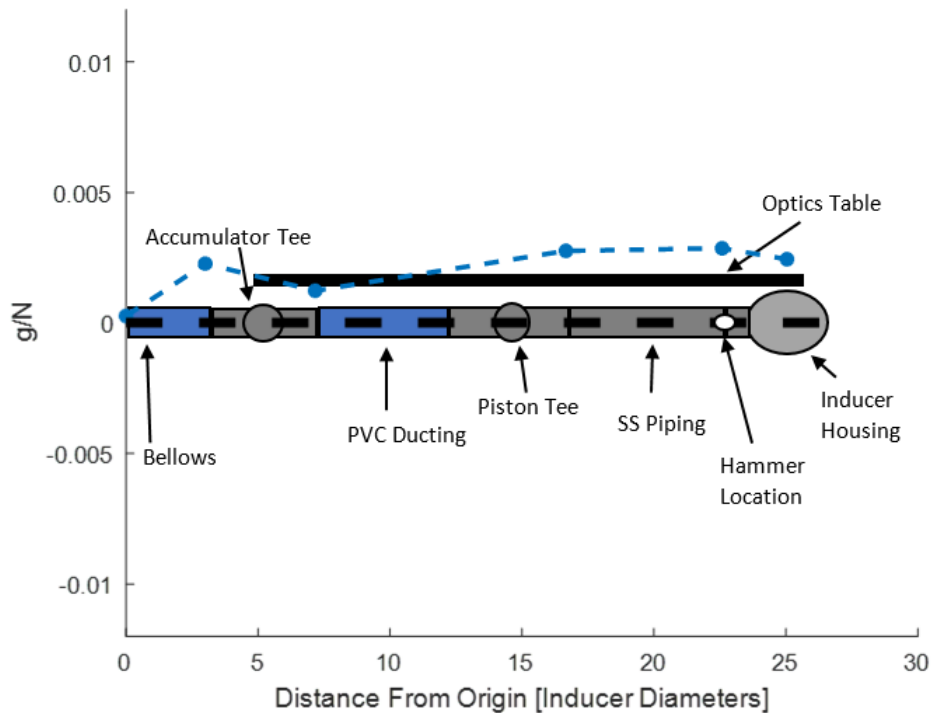


Figure 6-11: Measured mode shape overlaid a cartoon of test facility indicated that the 0.05 rotor frequency is caused by the optics table pitch motion

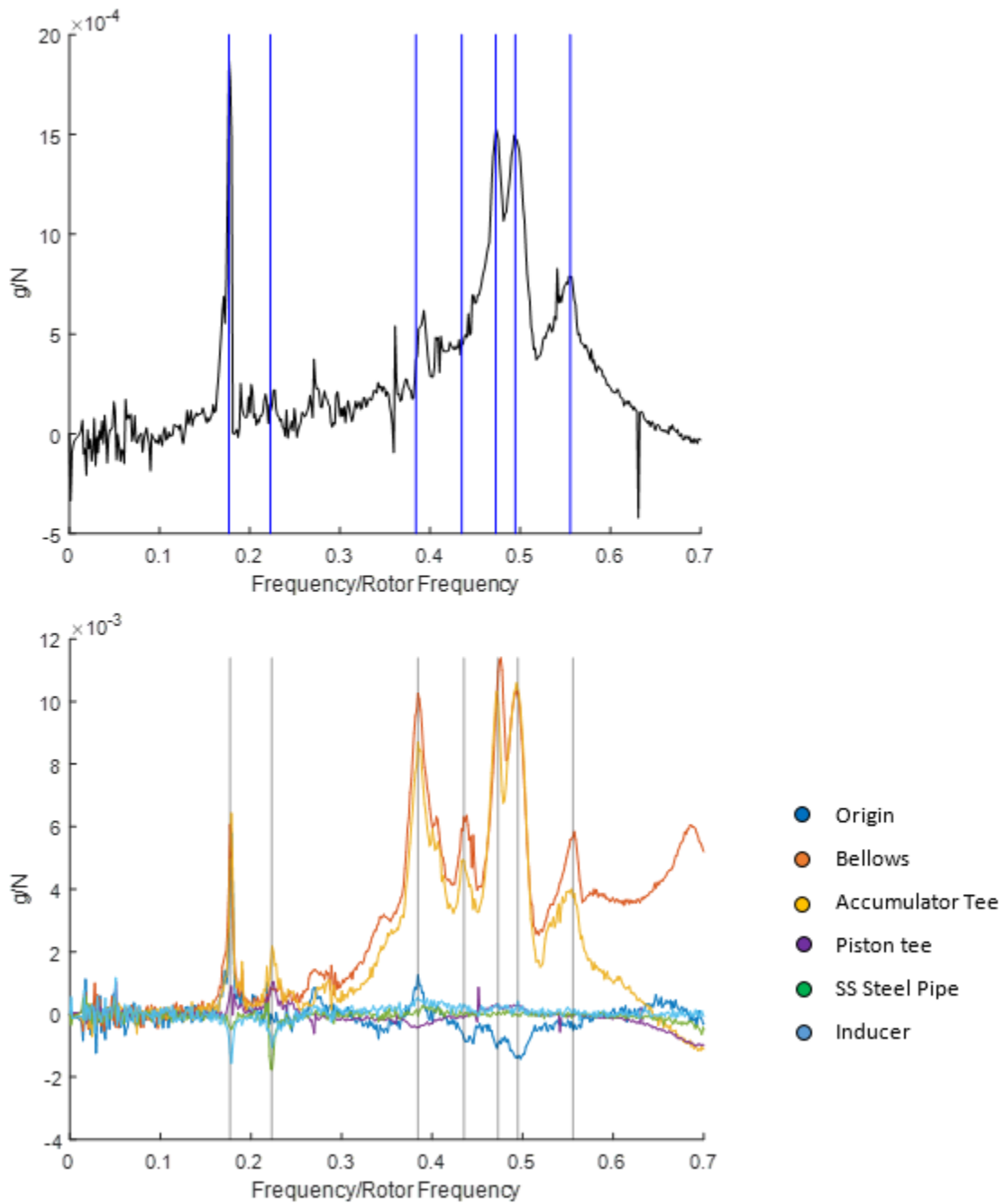


Figure 6-12: The sensor averaged FRF and overlaid sensor FRFs shows resonant frequencies at 0.18, 0.22, 0.38, 0.44, 0.47, 0.50, 0.56 rotor frequency. Hammer location at bellows-accumulator flange

Ducting rigid body mode

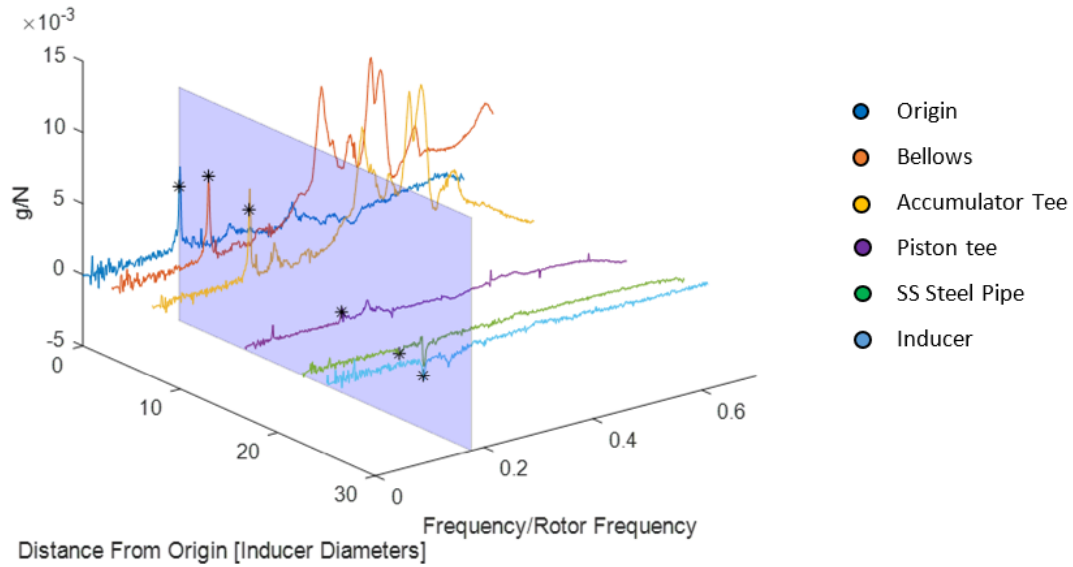


Figure 6-13: The 0.18 rotor frequency mode shape is generated by obtaining the magnitude of the imaginary portion of the FRF at each sensor location

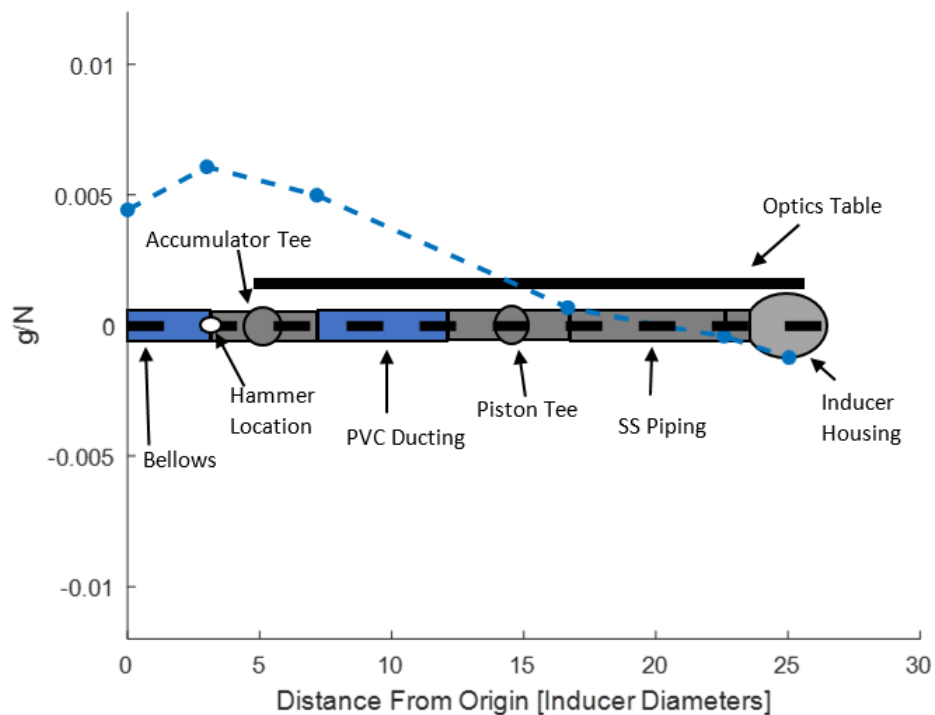


Figure 6-14: Measured mode shape overlaid a cartoon of test facility indicated that the 0.18 rotor frequency is a rigid body mode allowed by the flexibility of the bellows

Ducting bending mode

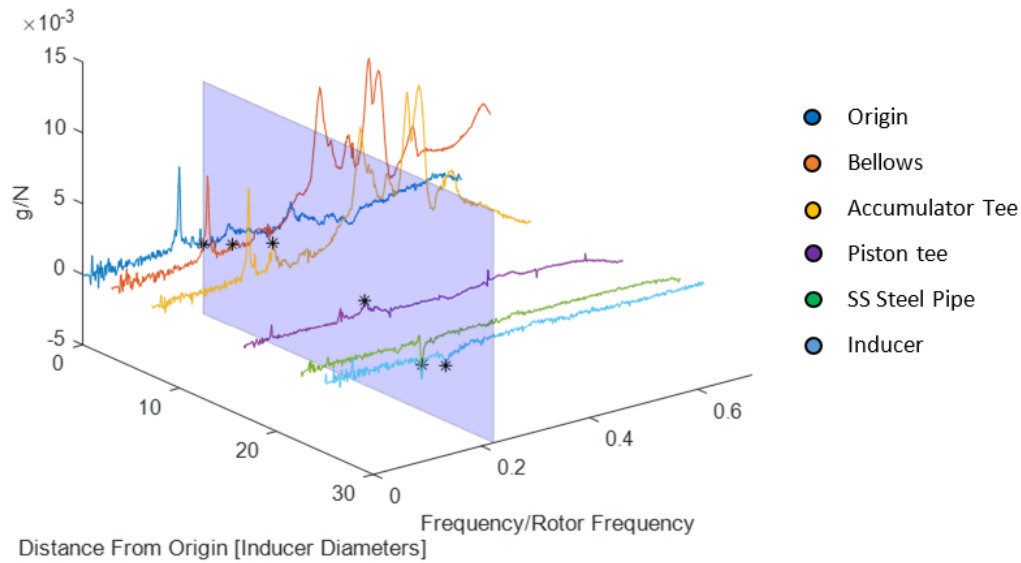


Figure 6-15: The 0.22 rotor frequency mode shape is generated by obtaining the magnitude of the imaginary portion of the FRF at each sensor location

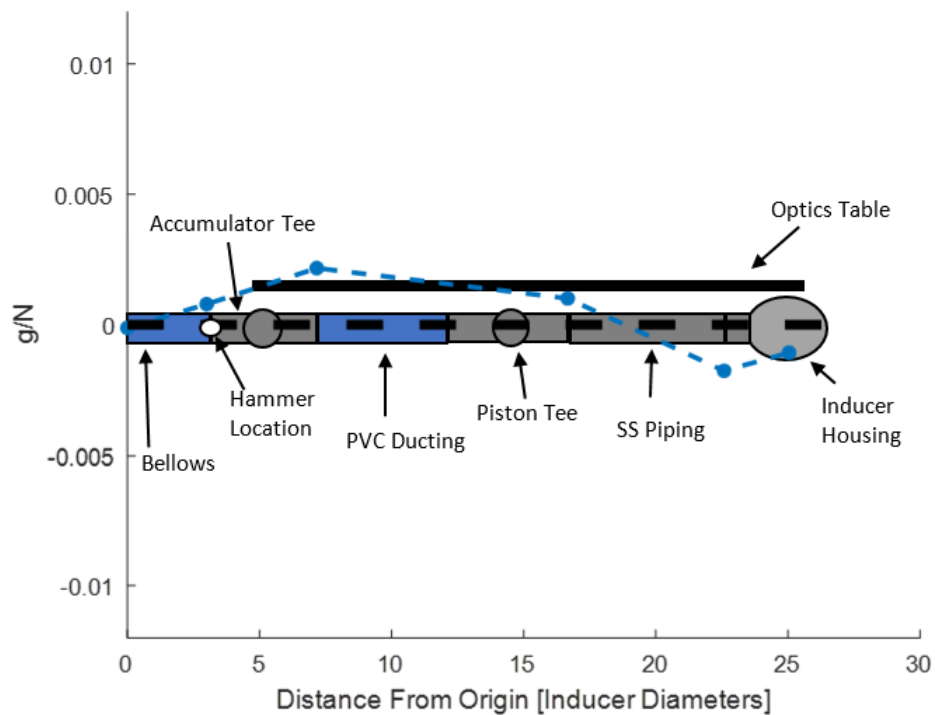


Figure 6-16: Measured mode shape overlaid a cartoon of test facility indicated that the 0.22 rotor frequency is a bending mode of the ducting

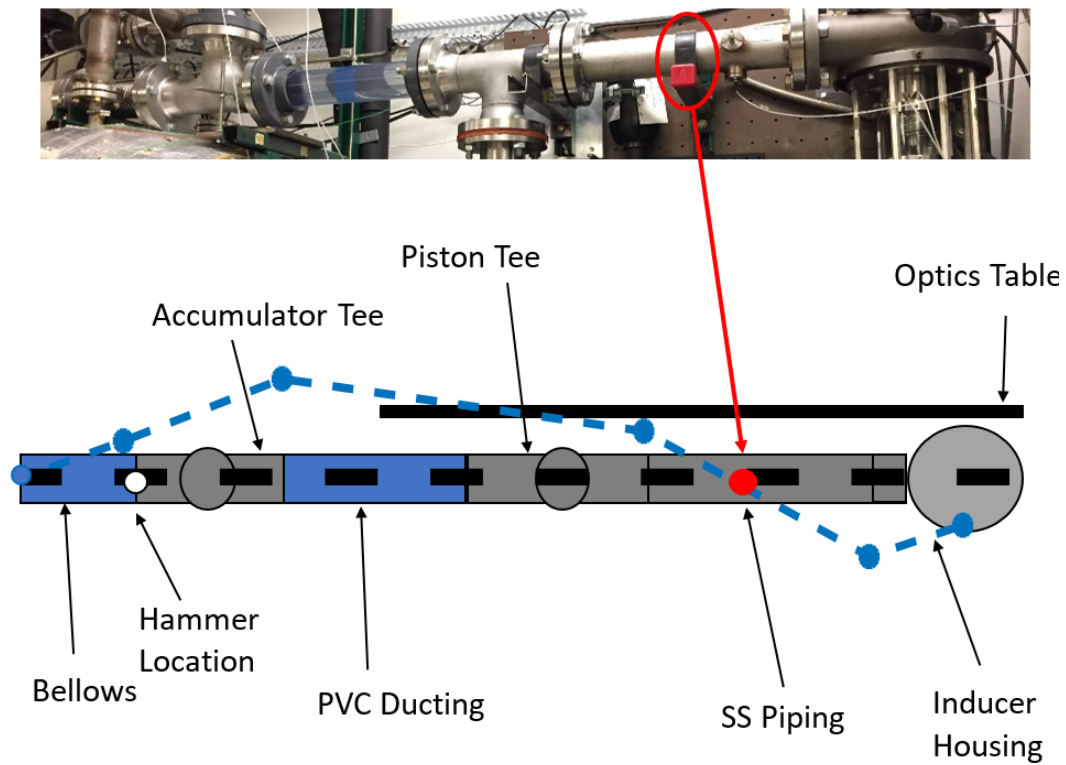


Figure 6-17: Fixed support at center of stainless steel pipe corresponds to node in mode shape

Bellows bending mode

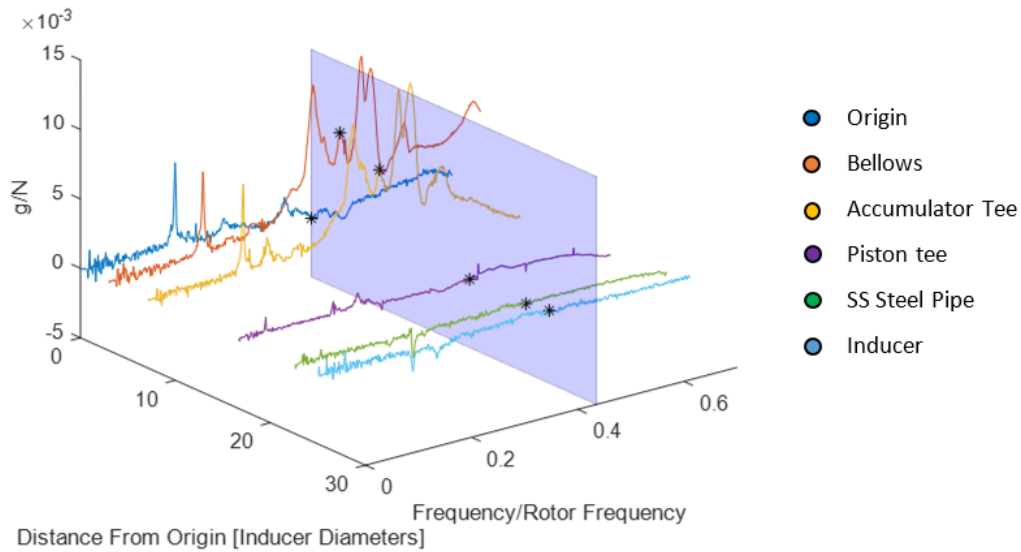


Figure 6-18: The 0.44 rotor frequency mode shape is generated by obtaining the magnitude of the imaginary portion of the FRF at each sensor location

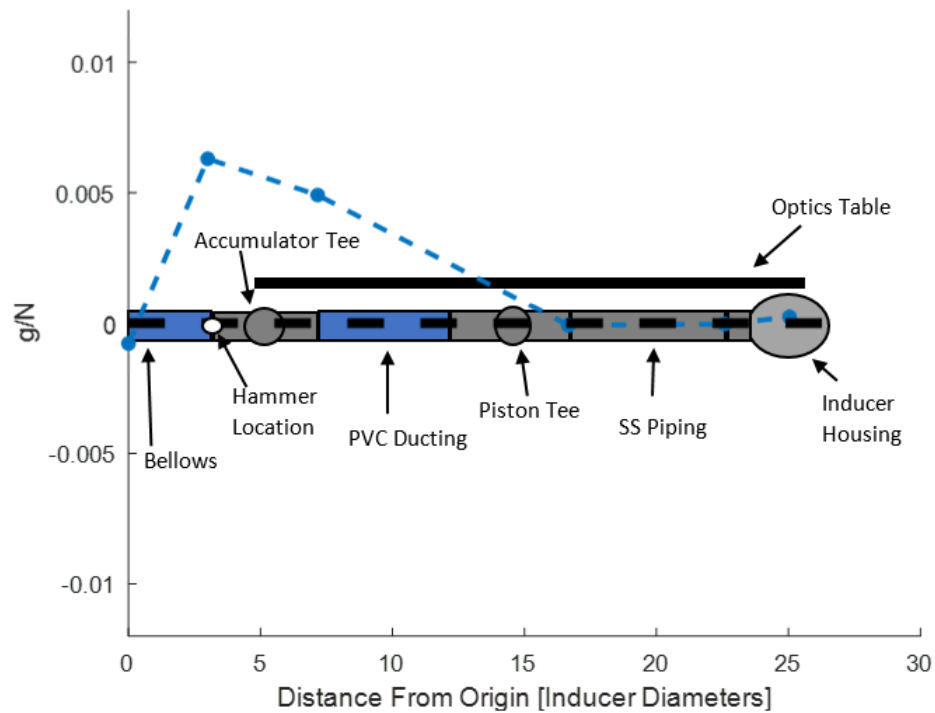


Figure 6-19: Measured mode shape overlaid a cartoon of test facility indicated that the 0.44 rotor frequency mode is a result of the flexibility of the bellows and accumulator tee support structure

Chapter 7

Conclusion

7.1 Summary

The goal of this thesis was to characterize the cavitation surge dynamics using a control theoretical system identification method. Previous work in the GTL [18] had demonstrated success with this method in aero-compressor systems, and this thesis attempted to adapt that methodology to cavitating inducers.

In order to test this methodology, The Aerospace Corporation's inducer test facility need to be modified to support forced response testing. A free response reduced order modeling framework was developed to replicate the measured cavitation surge dynamics captured in [13] and after validation of the free response model, a forced response modeling framework was derived. This model predicted the transfer functions of the pressure and velocity response and was used to design the modifications needed for the test facility.

The forced response model indicated that the perturbation magnitudes of the forced response test would be too large yielding significant non-linear effects. To remedy this an accumulator was added to the test facility. Trade studies conducted with the forced response model determined an adequate location for the accumulator and piston, as well as the required compliance of the accumulator.

After the first set of forced response tests, however, it was not able to characterize the inducer cavitation surge dynamics because challenges with the structural dynam-

ics of the test facility extended the experimental test plan past the timeline of this research project. However, the structural modes were identified through hammer tap testing, and it was recommended to stiffen the structural components so as to isolate the structural dynamics from the dynamic pressure and velocity measurements.

7.2 Recommendation for Future Work

To demonstrate that the control theoretical system identification method is a suitable alternative for characterization of cavitation dynamics, it is recommended that:

- The bellows and PVC pipe of the inducer test facility be replaced with stainless steel piping to prevent the excitation of structural modes.
- A forced response experiment is conducted and used to characterize the dynamics of just the gas accumulator and to verify that the natural frequency of the accumulator matches the simulated values.
- A forced response experiment is conducted with the inducer operating at the same flow conditions as Brennen had tested in [3].
- The unsteady pressure and velocity measurements are used to determine all four transfer functions, and the inducer transmission matrix.
- The inducer lumped parameters (pump gain, resistance, inertance, compliance, mass flow gain factor) are extracted from the measured inducer transmission matrix, by fitting the measured data to the inducer lumped parameter model.

After successful characterization of the cavitation surge dynamics, the longer term recommendation is to apply this methodology to rotating cavitation dynamics by:

- Creating a reduced order model to determine what modifications are needed for the inducer test facility
- Modifying the control theoretical system identification methodology for higher spatial harmonic perturbations to represent rotating cavitation.

- Modifying inducer test facility with a distributed array of pressure transducers, fiber film probes, and bleed valve actuators.
- Conducting a forced response test to characterize the rotating cavitation dynamics

Appendix A

Non-dimensional Compliances and Mass Flow Gain Factors

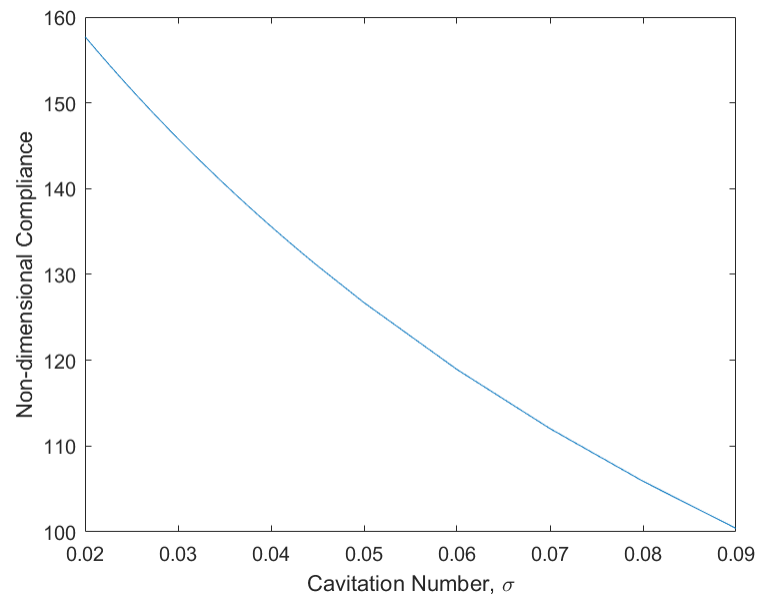


Figure A-1: Non-dimensional compliance of storage tank

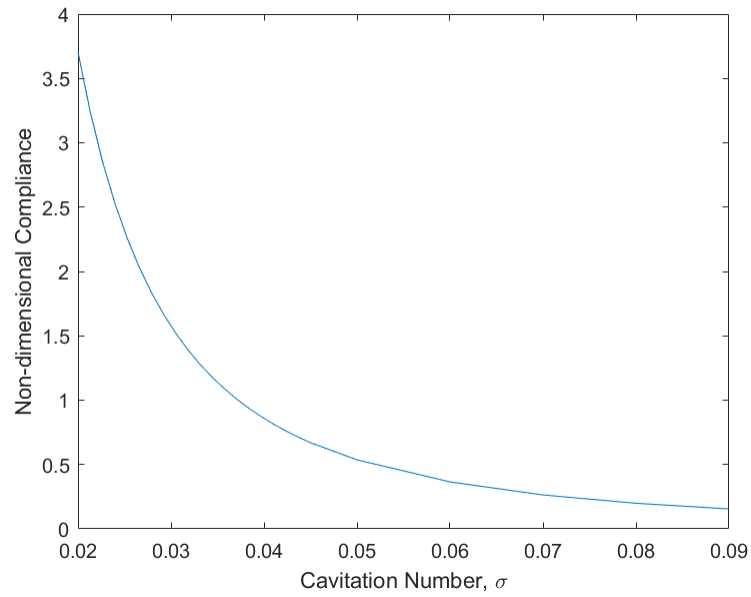


Figure A-2: Non-dimensional compliance of inducer from CFD [10]

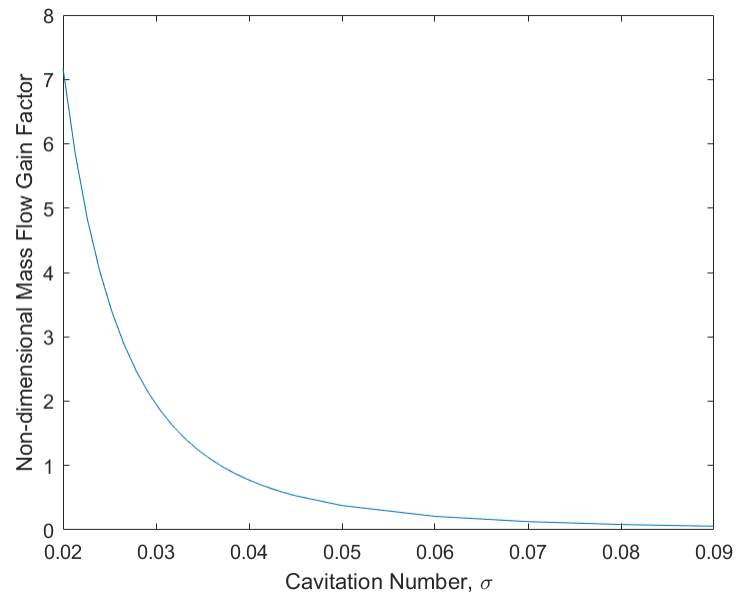


Figure A-3: Non-dimensional mass flow gain factor of inducer from CFD [10]

Appendix B

Inducer Model Selection

The determination of the inducer model was done by comparing the simulated eigenvalues using both inducer models. The eigenvalues were found for the fluid system modeled with the transmission matrix Equation (3.6) and the eigenvalue equation for open-open boundary conditions, Equation (3.7). Using the CFD derived C and M by Jackson et al. [10], both models were inaccurate but exhibit correct trends, so the cavitation compliance and mass flow gain factor was modified to fit the measured dynamic behavior.

Figures B-1, B-2 compares the simulation results using the two inducer models and the same CFD derived cavitation compliance and mass flow gain factor.

Both models showed similar stability trends where between $\sigma = 0.03$ and $\sigma = 0.02$ the critical damping percentage rose, but neither predict the onset of cavitation surge instability. Additionally the frequency trend for both models agreed with the experimental findings, where the cavitation surge frequency increased with increased cavitation number. However, the measured cavitation surge frequencies were bounded by the two models, indicating that the modification of cavitation compliance would need to be increased for the lumped parameter model, and decreased for the 1D cavitation surge model.

As was done in Section 3.3.3 a time lag and scaling coefficient was added to the CFD cavitation compliance and mass flow gain factor. The required C and M to capture the test data with each model are shown in Table B.1.

Table B.1: Modified Cavitation Compliance and Mass Flow Gain Factor for Lumped Parameter and 1D Cavitation Surge Models

	Cavitation Compliance	Mass Flow Gain Factor
Lumped Parameter Model	$\frac{1.3C}{1+0.6s}$	$\frac{2M}{1+0.6s}$
1D Cavitation Surge Model	$\frac{0.3C}{1+0.5s}$	$\frac{M}{1+0.5s}$

Figures B-3, B-4 compare the stability and frequency of the models with the

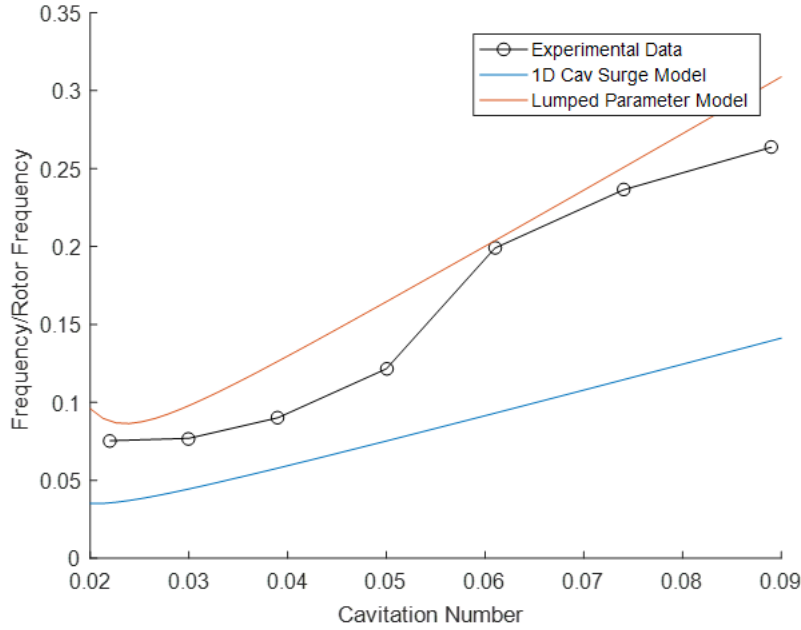


Figure B-1: Cavitation surge frequency found using the lumped parameter inducer model and the 1D cavitation surge model and CFD derived C and M bound the measured cavitation surge frequency

modified C and M values. Even though the lumped model predictions with the modified C and M has closer onset and termination points than the 1D cavitation surge model, the 1D cavitation surge model will be carried forward in this thesis. It was chosen because a gain was not applied to the mass flow gain factor, and so less modifications was done to the input parameters. Additionally Jackson et al. had used their CFD results in their own stability model, and found that a reduction of the mass flow gain factor was needed to more correctly model their system, opposite of what was found in this thesis [10].

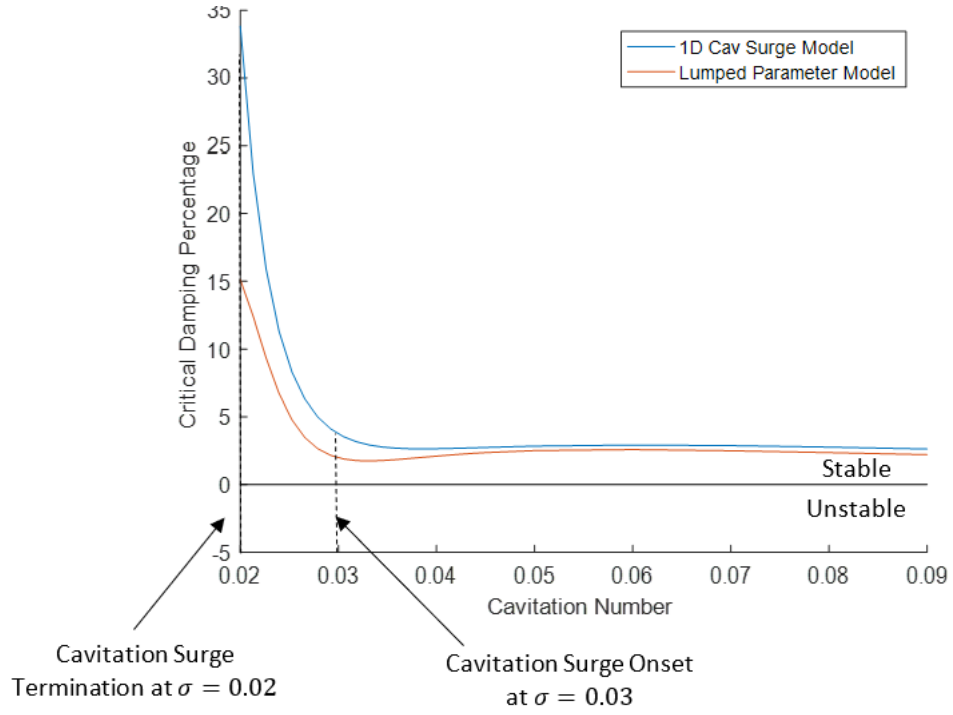


Figure B-2: Neither the lumped parameter model nor the 1D cavitation surge model matched the observed stability behavior. The critical damping percentage is shown; CFD Derived C and M is used

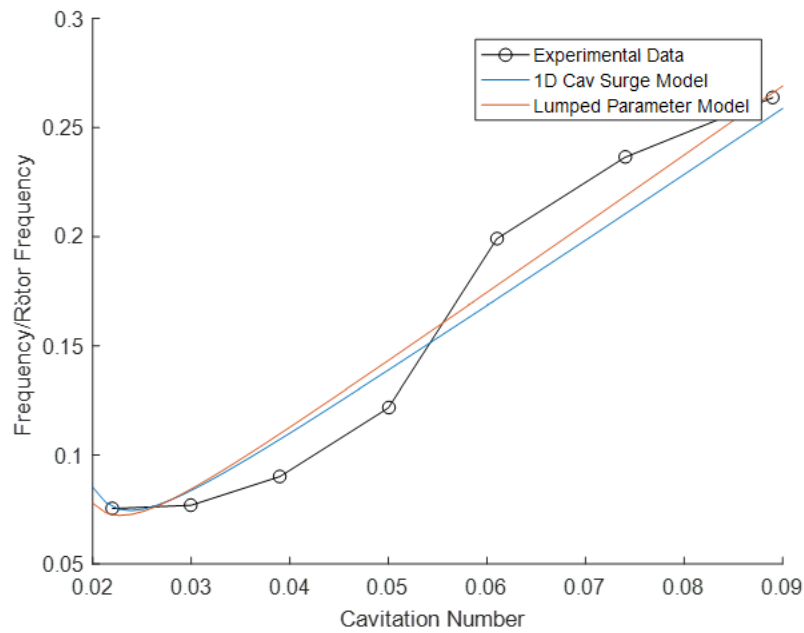


Figure B-3: Modifications to the CFD derived C and M yielded simulated frequency content that matched the observed behavior

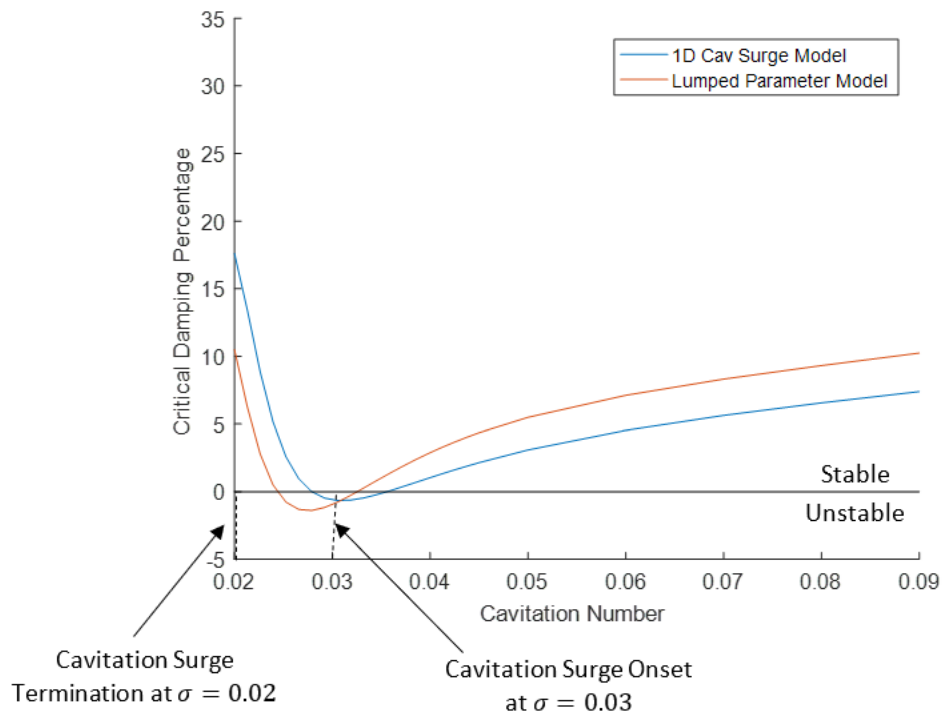


Figure B-4: Modifications to the CFD derived C and M yielded simulated stability trends that matched the observed behavior

Appendix C

Transfer Function Bode Plots

C.1 Piston Location Trade Study

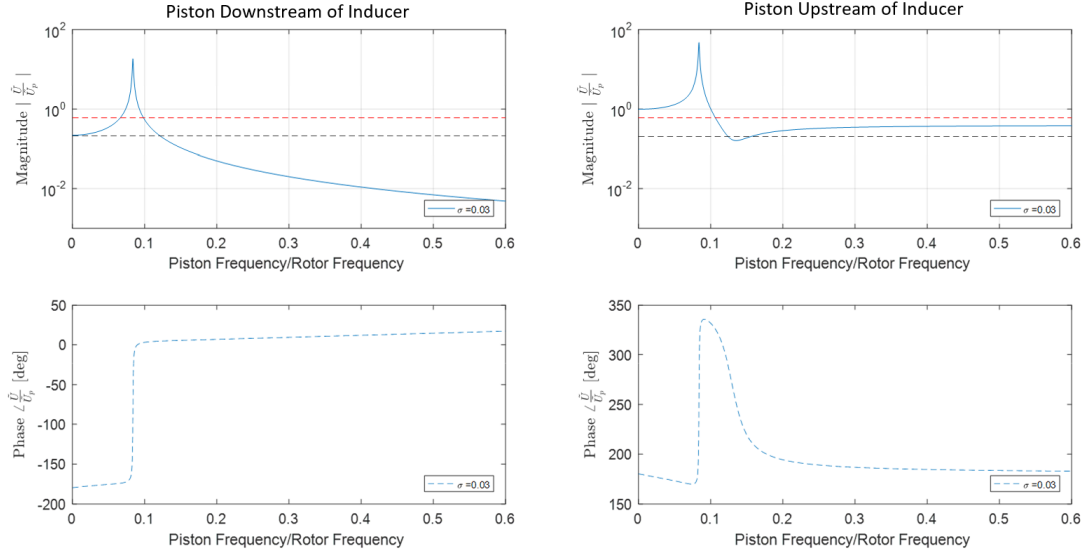


Figure C-1: Comparison of upstream velocity transfer function, at $\phi = 0.06$ and $\sigma = 0.03$, shows when piston is placed upstream of inducer, larger magnitude responses are found. Piston placed downstream of inducer (right), Piston placed upstream of inducer (left)

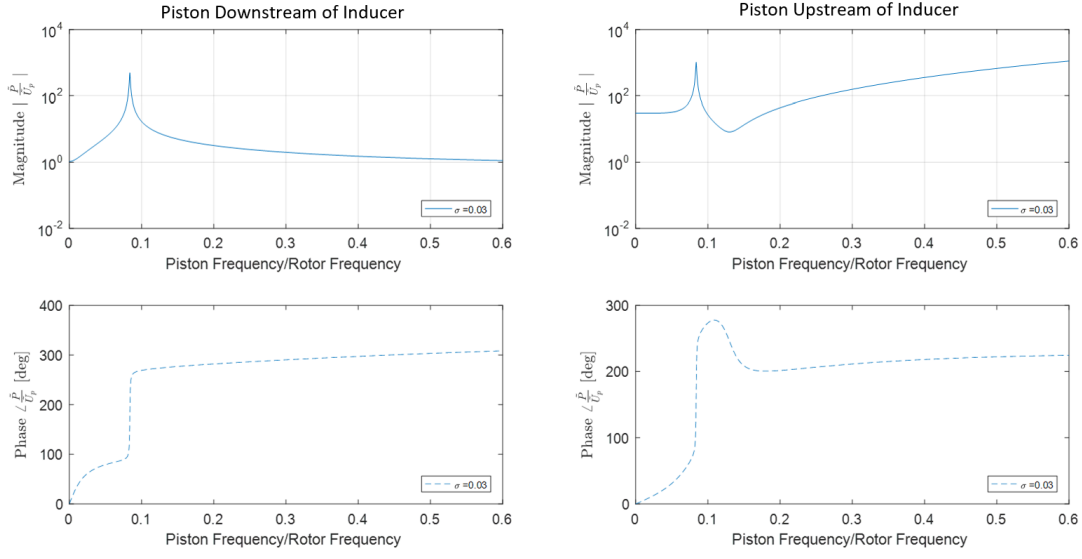


Figure C-2: Comparison of downstream pressure transfer function, at $\phi = 0.06$ and $\sigma = 0.03$, shows when piston is placed upstream of inducer, larger magnitude responses are found. Piston placed downstream of inducer (right), Piston placed upstream of inducer (left)

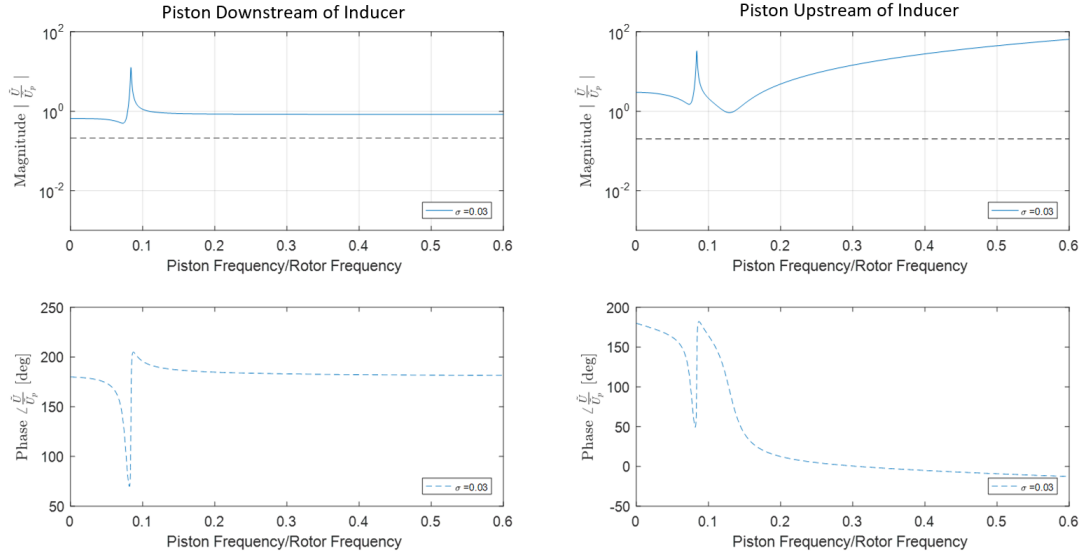


Figure C-3: Comparison of downstream velocity transfer function, at $\phi = 0.06$ and $\sigma = 0.03$, shows when piston is placed upstream of inducer, larger magnitude responses are found. Piston placed downstream of inducer (right), Piston placed upstream of inducer (left)

C.2 Accumulator Location Trade Study

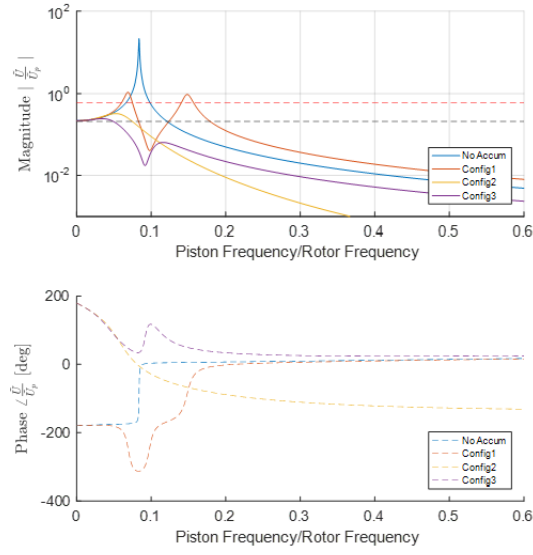


Figure C-4: Comparison of upstream velocity transfer function, at $\phi = 0.06$ and $\sigma = 0.03$, shows when accumulator is placed near the inducer, the two modes overlap. Placing the accumulator downstream of the piston and inducer results in desired smaller perturbation magnitudes

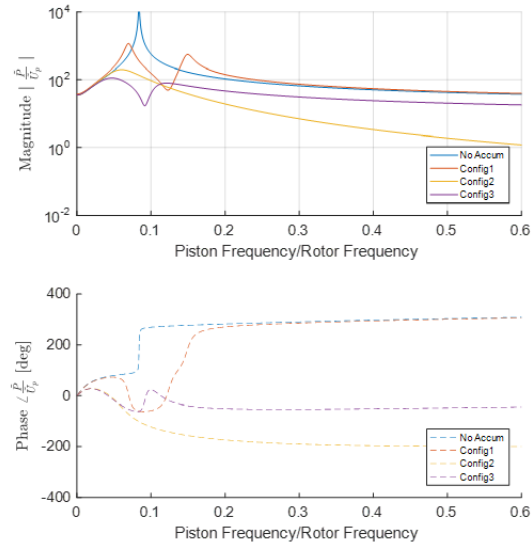


Figure C-5: Comparison of downstream pressure transfer function, at $\phi = 0.06$ and $\sigma = 0.03$, shows when accumulator is placed near the inducer, the two modes overlap. Placing the accumulator downstream of the piston and inducer results in desired smaller perturbation magnitudes

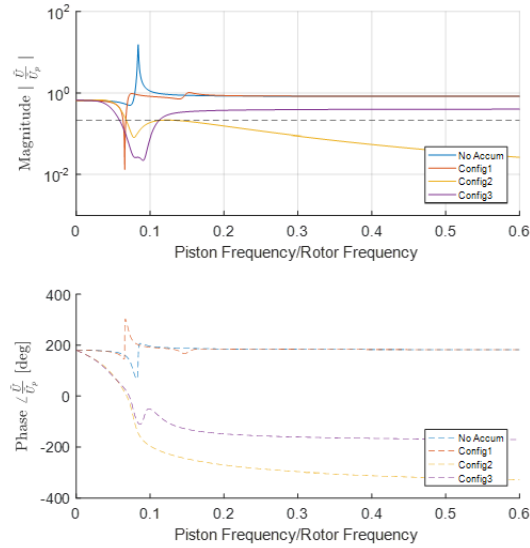


Figure C-6: Comparison of downstream velocity transfer function, at $\phi = 0.06$ and $\sigma = 0.03$, shows when accumulator is placed near the inducer, the two modes overlap. Placing the accumulator downstream of the piston and inducer results in desired smaller perturbation magnitudes

C.3 Accumulator Compliance Trade Study

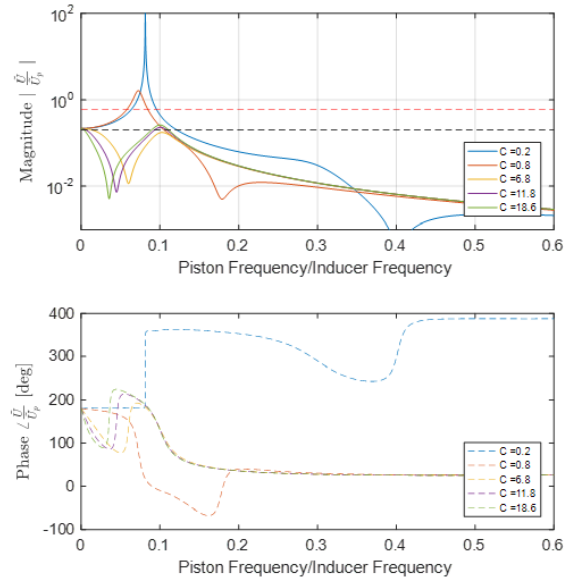


Figure C-7: Accumulator mode natural frequency is inversely proportional to the accumulator compliance: upstream velocity transfer function, $\sigma = 0.03$, $\phi = 0.06$

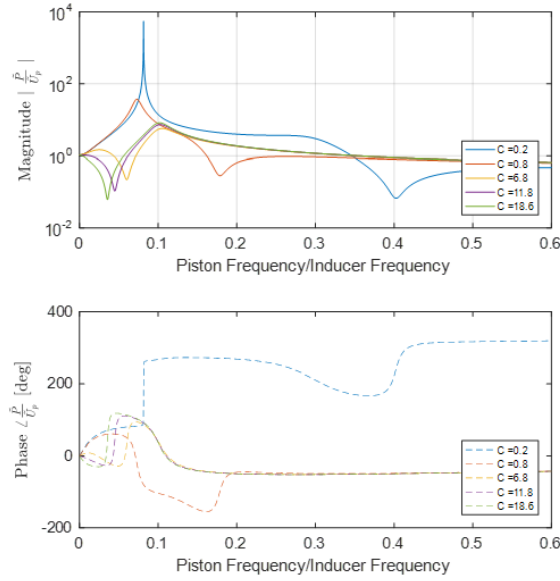


Figure C-8: Accumulator mode natural frequency is inversely proportional to the accumulator compliance: downstream pressure transfer function, $\sigma = 0.03$, $\phi = 0.06$

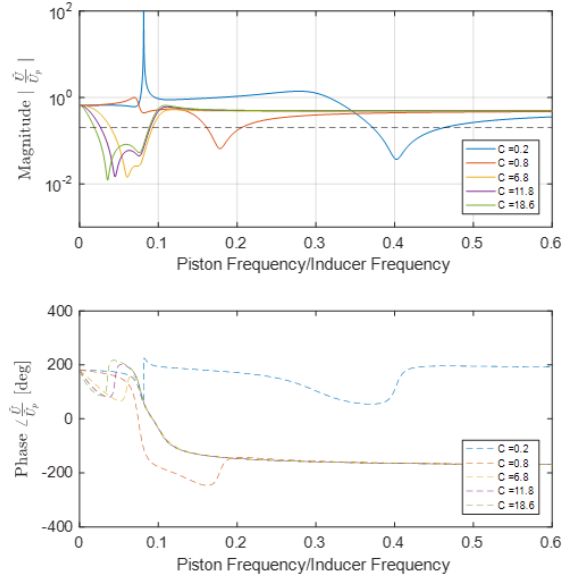


Figure C-9: Accumulator mode natural frequency is inversely proportional to the accumulator compliance: downstream velocity transfer function, $\sigma = 0.03$, $\phi = 0.06$

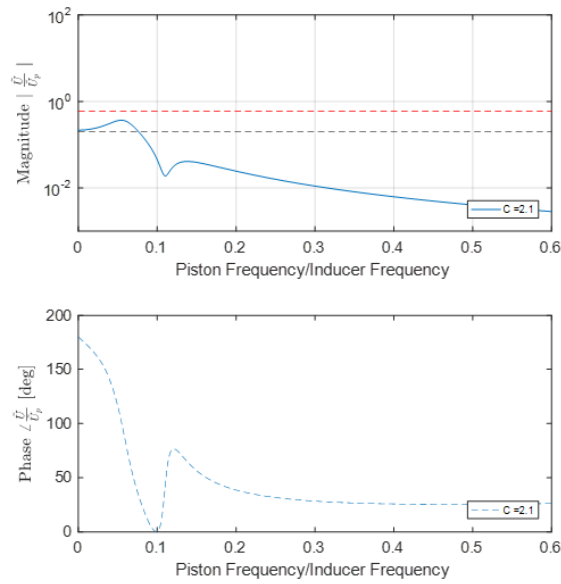


Figure C-10: Accumulator mode is tuned to similar frequency as inducer cavitation surge mode. The poles are difficult to identify from each other: upstream pressure transfer function, $\sigma = 0.03$, $\phi = 0.06$, $C_{accum} = 2.1$

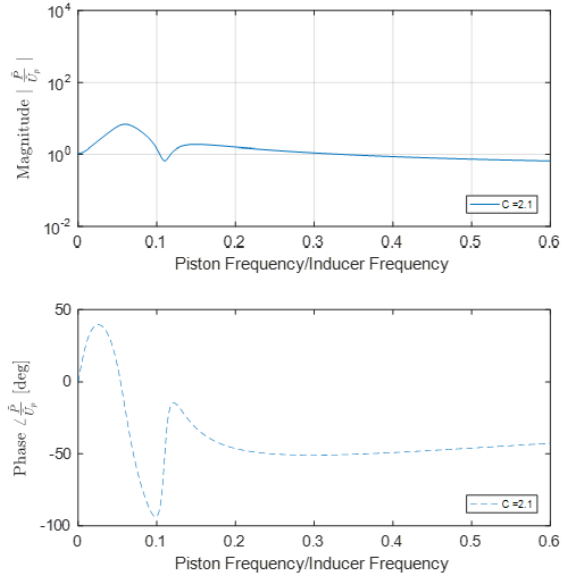


Figure C-11: Accumulator mode is tuned to similar frequency as inducer cavitation surge mode. The poles are difficult to identify from each other: upstream pressure transfer function, $\sigma = 0.03$, $\phi = 0.06$, $C_{accum} = 2.1$

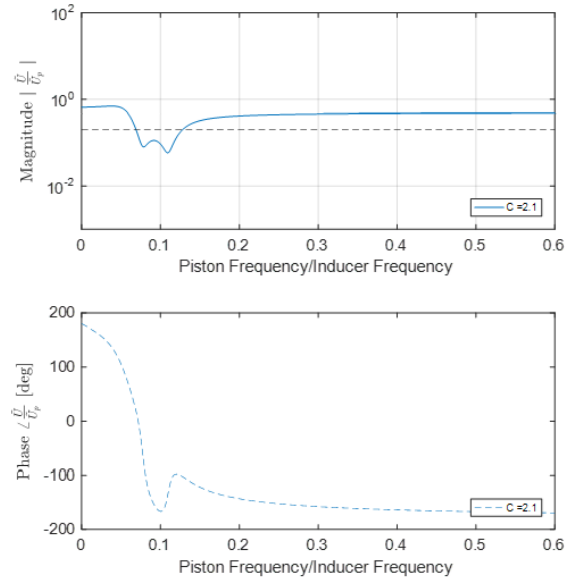


Figure C-12: Accumulator mode is tuned to similar frequency as inducer cavitation surge mode. The poles are difficult to identify from each other: upstream pressure transfer function, $\sigma = 0.03$, $\phi = 0.06$, $C_{accum} = 2.1$

C.4 Accumulator Resistance Trade Study

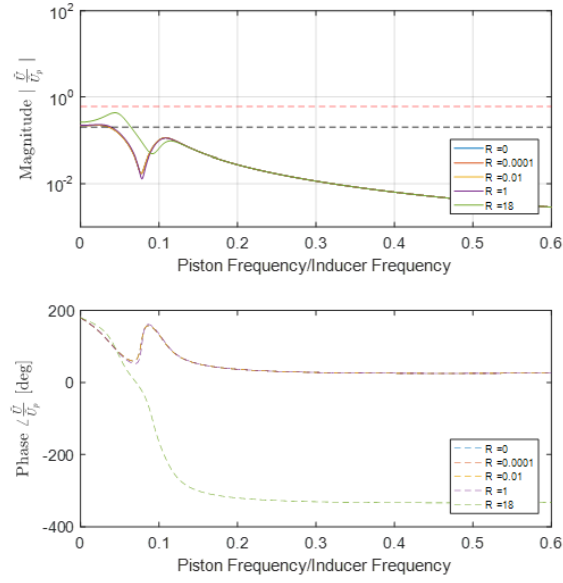


Figure C-13: Accumulator resistance, unless nearing the resistance levels of the porous media valve, has little effect on the upstream velocity perturbation transfer function: $\sigma = 0.03$, $\phi = 0.06$, $C_{accum} = 3$

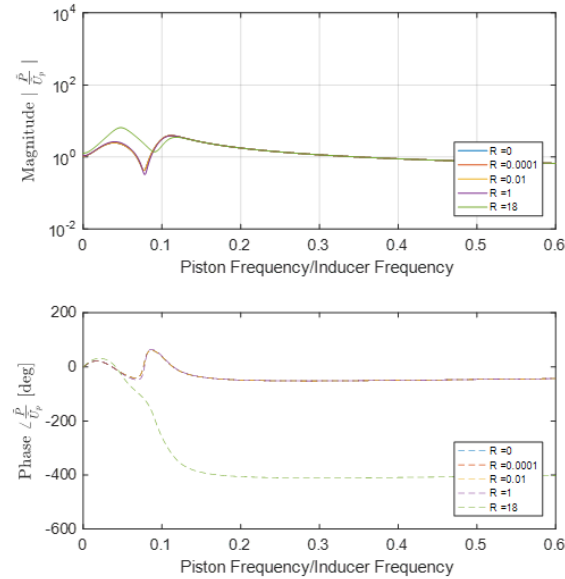


Figure C-14: Accumulator resistance, unless nearing the resistance levels of the porous media valve, has little effect on the downstream pressure perturbation transfer function: $\sigma = 0.03$, $\phi = 0.06$, $C_{accum} = 3$

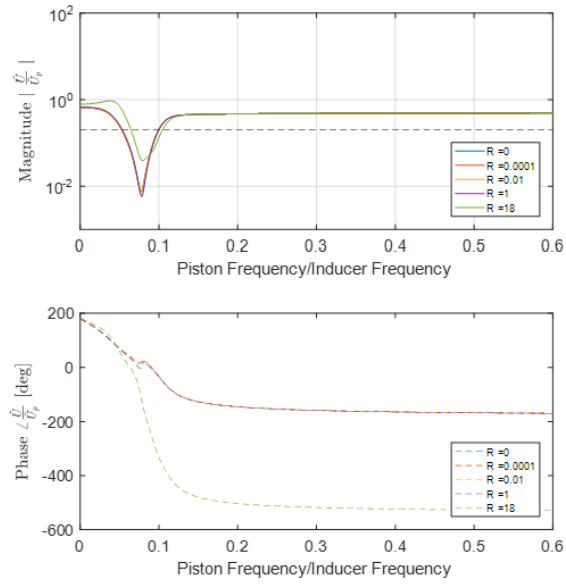


Figure C-15: Accumulator resistance, unless nearing the resistance levels of the porous media valve, has little effect on the downstream velocity perturbation transfer function: $\sigma = 0.03$, $\phi = 0.06$, $C_{accum} = 3$

C.5 Recommended Design

C.5.1 Low Cavitation Design

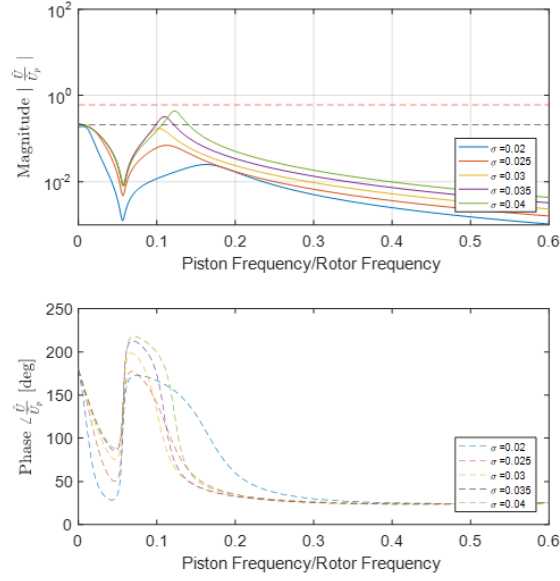


Figure C-16: Bode plots of upstream velocity perturbation transfer functions: Recommended configuration of inducer test facility for low cavitation number flows

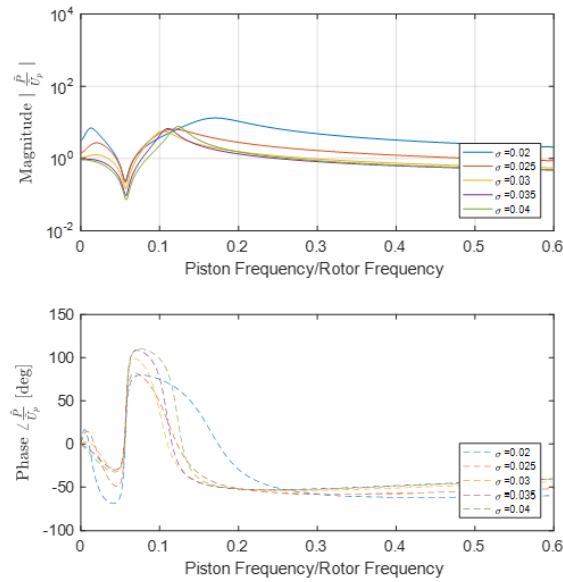


Figure C-17: Bode plots of downstream pressure perturbation transfer functions: Recommended configuration of inducer test facility for low cavitation number flows

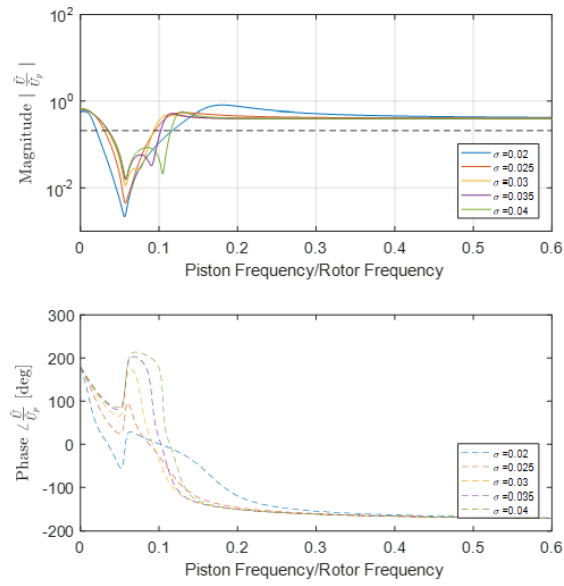


Figure C-18: Bode plots of downstream velocity perturbation transfer functions: Recommended configuration of inducer test facility for low cavitation number flows

C.5.2 High Cavitation Design

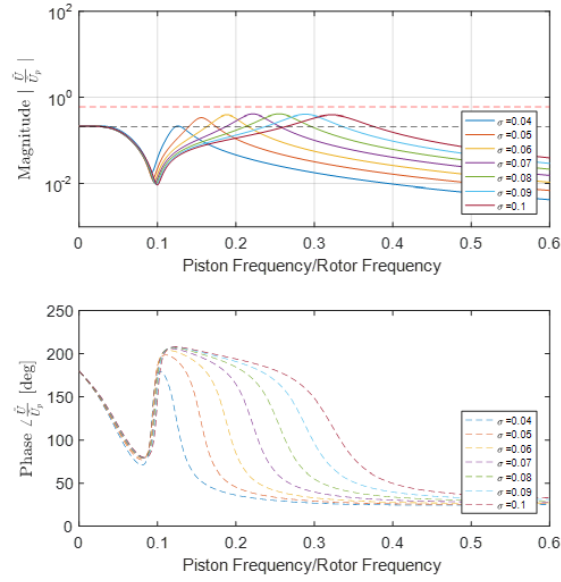


Figure C-19: Bode plots of upstream velocity perturbation transfer functions: Recommended configuration of inducer test facility for high cavitation number flows

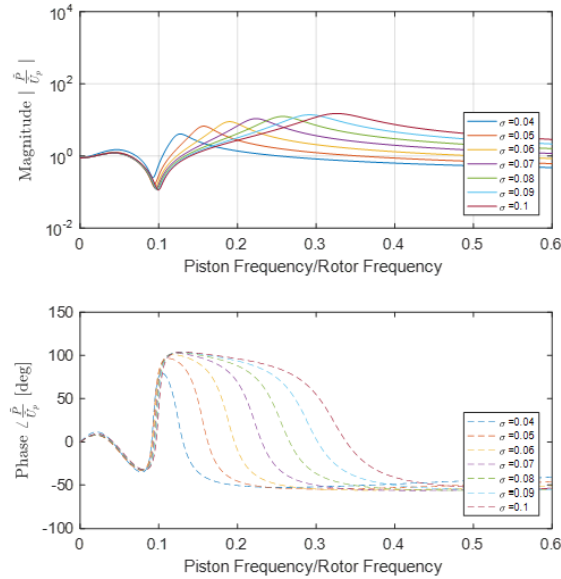


Figure C-20: Bode plots of downstream pressure perturbation transfer functions: Recommended configuration of inducer test facility for high cavitation number flows

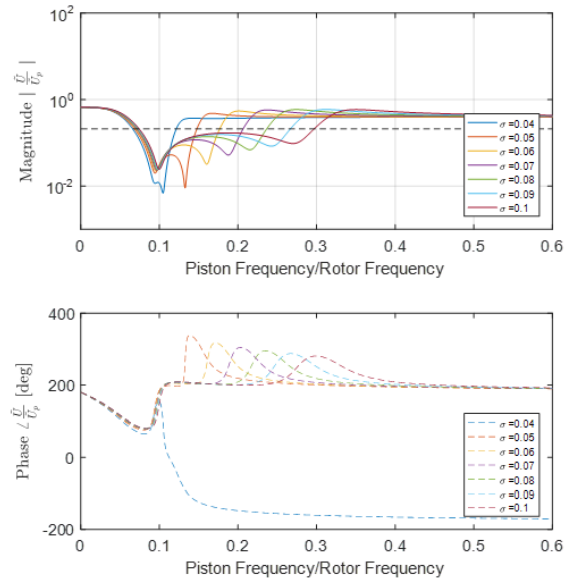


Figure C-21: Bode plots of downstream velocity perturbation transfer functions: Recommended configuration of inducer test facility for high cavitation number flows

Appendix D

Fiber Film Probe Calibration

This section provides a summary of how to calibrate the fiber film probes. A more detailed explanation and analysis can be found in [11]. In order to collect velocity measurements, the fiber film probe needs to be calibrated with a known velocity. Since there was no available water tunnel, the probes were calibrated in-situ with the test. The Aerospace inducer test facility has the capability to measure volumetric flow rate, so the strategy to calibrate the probes was to equate this volumetric flow with an integrated voltage profile measured by traversing the fiber film probe across the duct. The initial estimate for the fiber film calibration coefficients is generated with measurements collected with the probe perpendicular to the flow direction, and is corrected with measurements captured when the probe is parallel with the flow direction.

First, the voltage profile is generated by collecting flow measurements at 5 locations starting from the center of the duct and moving 0.25 radii outward. Due to physical limitations however, the location near the wall was taken at 0.95 radii from the center. These measurements are repeated 4 times at a flow coefficient of 0, 0.07, 0.085, and 0.1. Using each generated voltage profile, the following integral is solved

$$Q = \int_0^R 2\pi r v(E) dr \quad (\text{D.1})$$

where the velocity voltage relation is assumed to be a two term power relation

$$v = A + BE^n. \quad (\text{D.2})$$

In these equations, Q is the volumetric flow rate, R is the duct radius, v is the local velocity as a function of E , the measured voltage, and A , B and n are calibration coefficients.

To calculate the coefficients, a pseudo least-squares fit was performed. An initial value of n was chosen so that A and B could be solved using the data from the flow coefficients of 0 and 0.1. The volumetric flow rate can then be estimated for flow coefficients of 0.07 and 0.08 and are then compared to the measured volumetric flow rate. n is adjusted until the sum of the squares error was minimized.

Because the probes measure velocity based off of heat transfer, the probes will measure a velocity even when the flow is parallel to wire. To correct these measurements Jørgensen's equation is used.

$$\Phi_e = \Phi_N + k^2\Phi_T \quad (\text{D.3})$$

Φ_e is the effective flow coefficient (the measured velocity), Φ_N is the true flow coefficient perpendicular to the flow, and Φ_T is the true flow coefficient parallel to the probe. To calculate k it is assumed that the flow at the centerline is purely axial. This means that $\Phi_T = 0$ and k can be generated from the axial and swirl direction measurements at the centerline.

Appendix E

Hammer Tap Test FRF and Modeshapes

Bellows Bending Modes

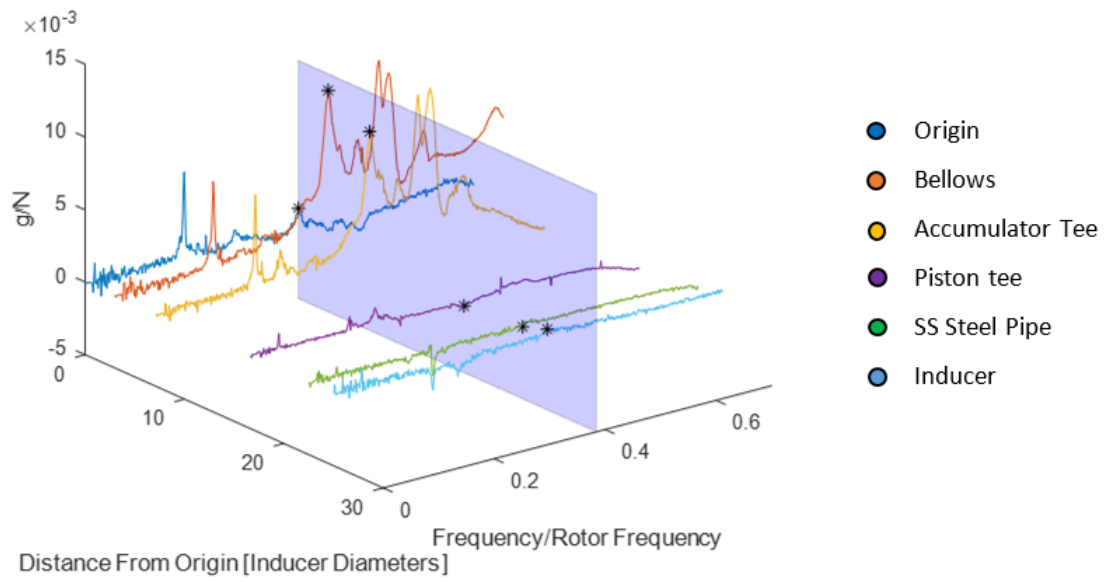


Figure E-1: The 0.38 rotor frequency mode shape is generated by obtaining the magnitude of the imaginary portion of the FRF at each sensor location

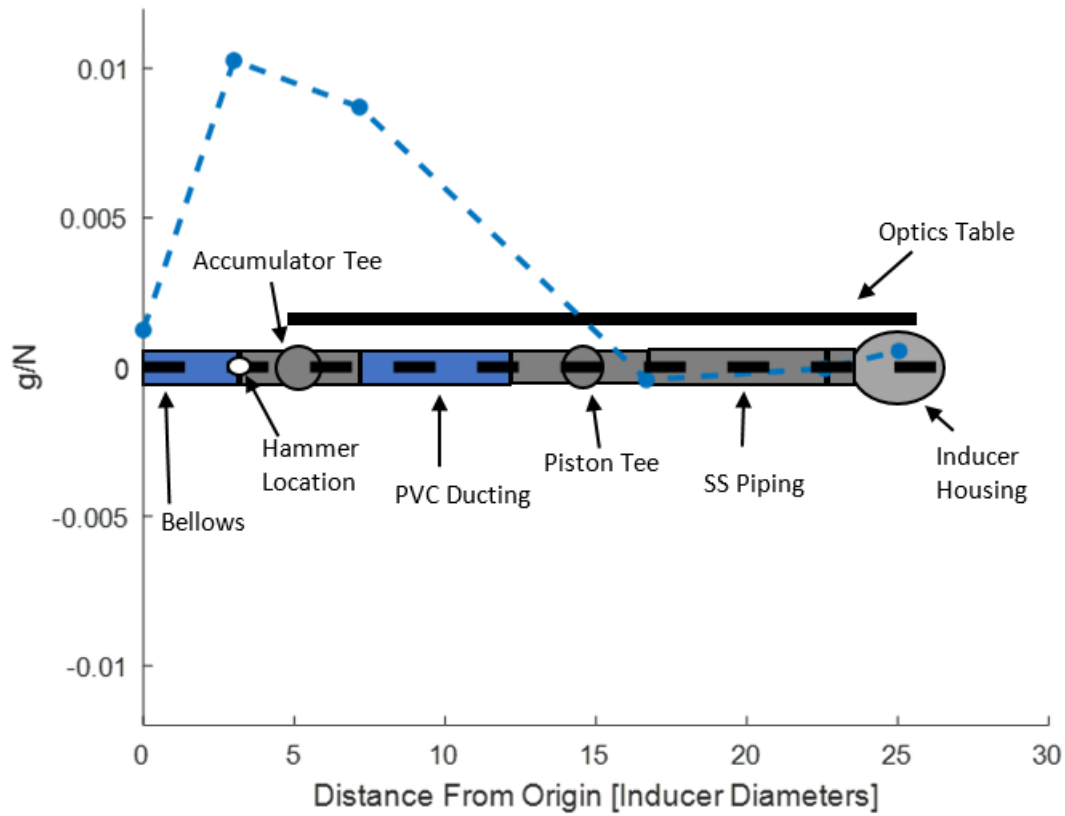


Figure E-2: Measured mode shape overlaid a cartoon of test facility indicated that the 0.38 rotor frequency mode is a result of the flexibility of the bellows and accumulator tee support structure

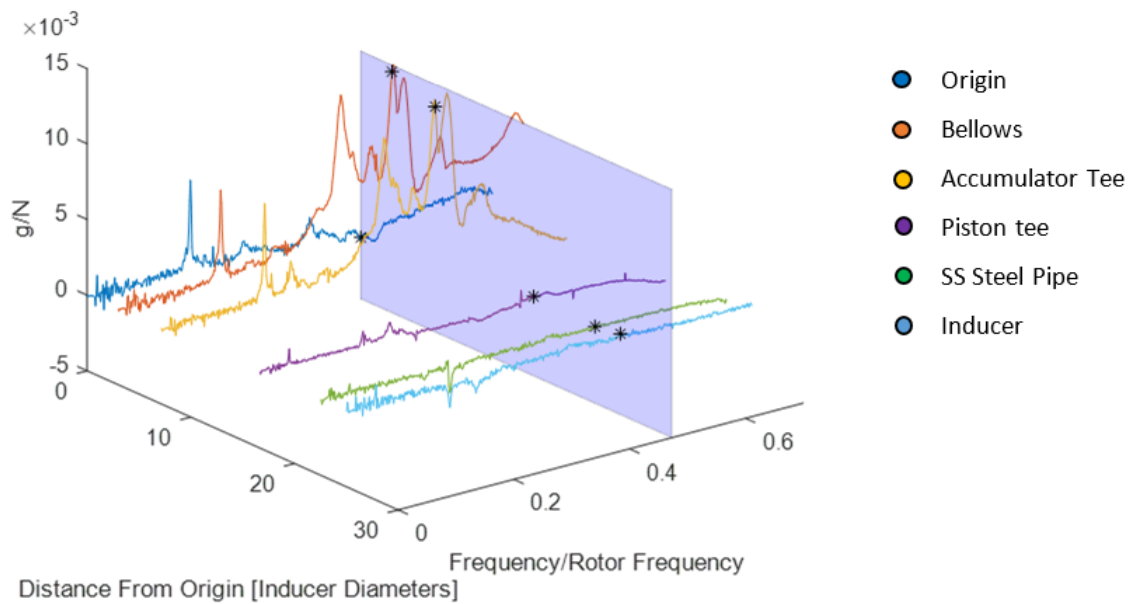


Figure E-3: The 0.47 rotor frequency mode shape is generated by obtaining the magnitude of the imaginary portion of the FRF at each sensor location

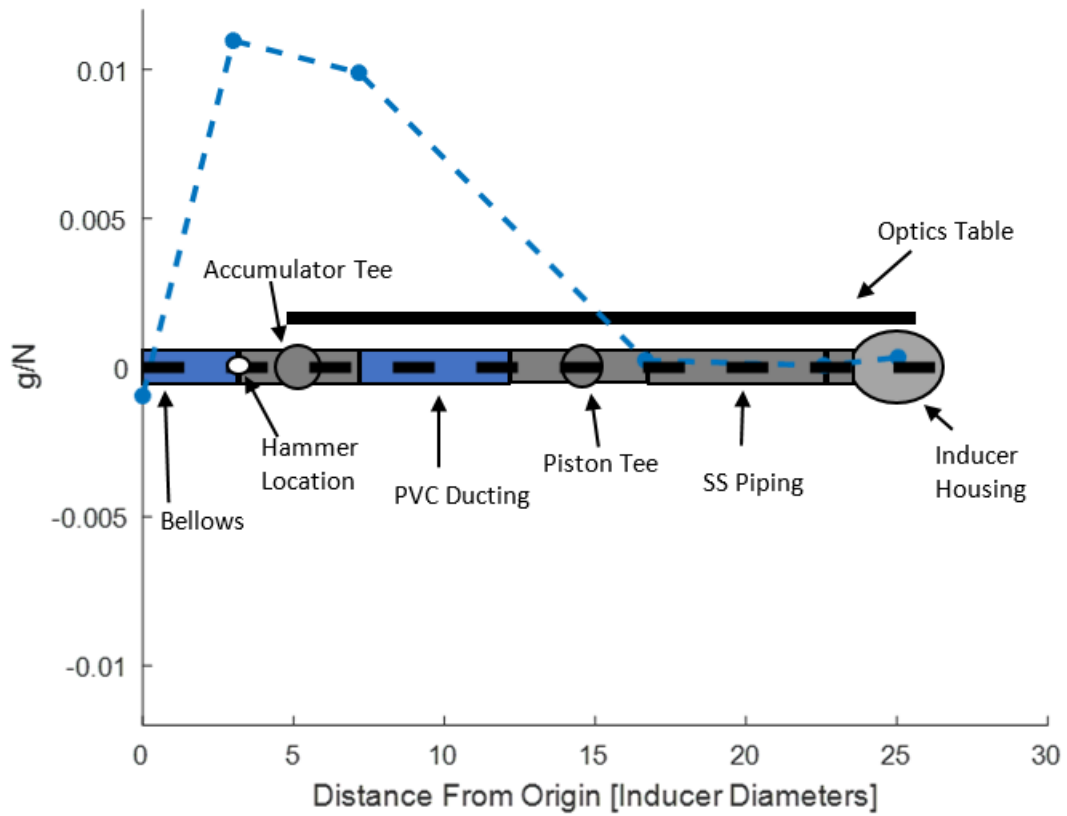


Figure E-4: Measured mode shape overlaid a cartoon of test facility indicated that the 0.47 rotor frequency mode is a result of the flexibility of the bellows and accumulator tee support structure

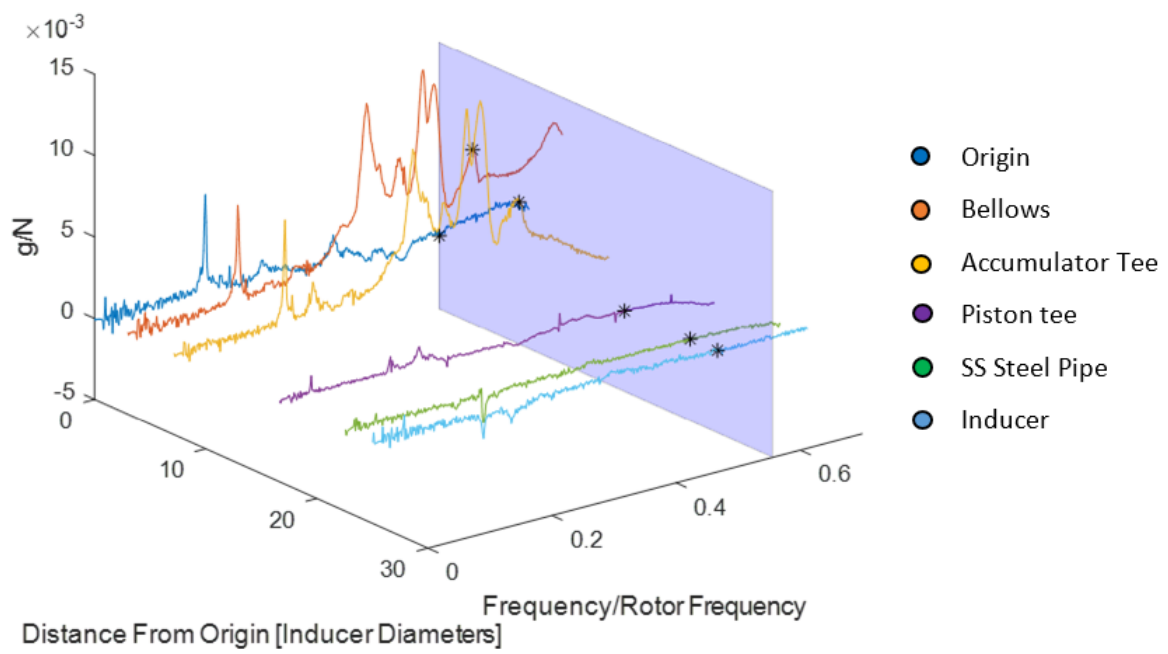


Figure E-5: The 0.56 rotor frequency mode shape is generated by obtaining the magnitude of the imaginary portion of the FRF at each sensor location

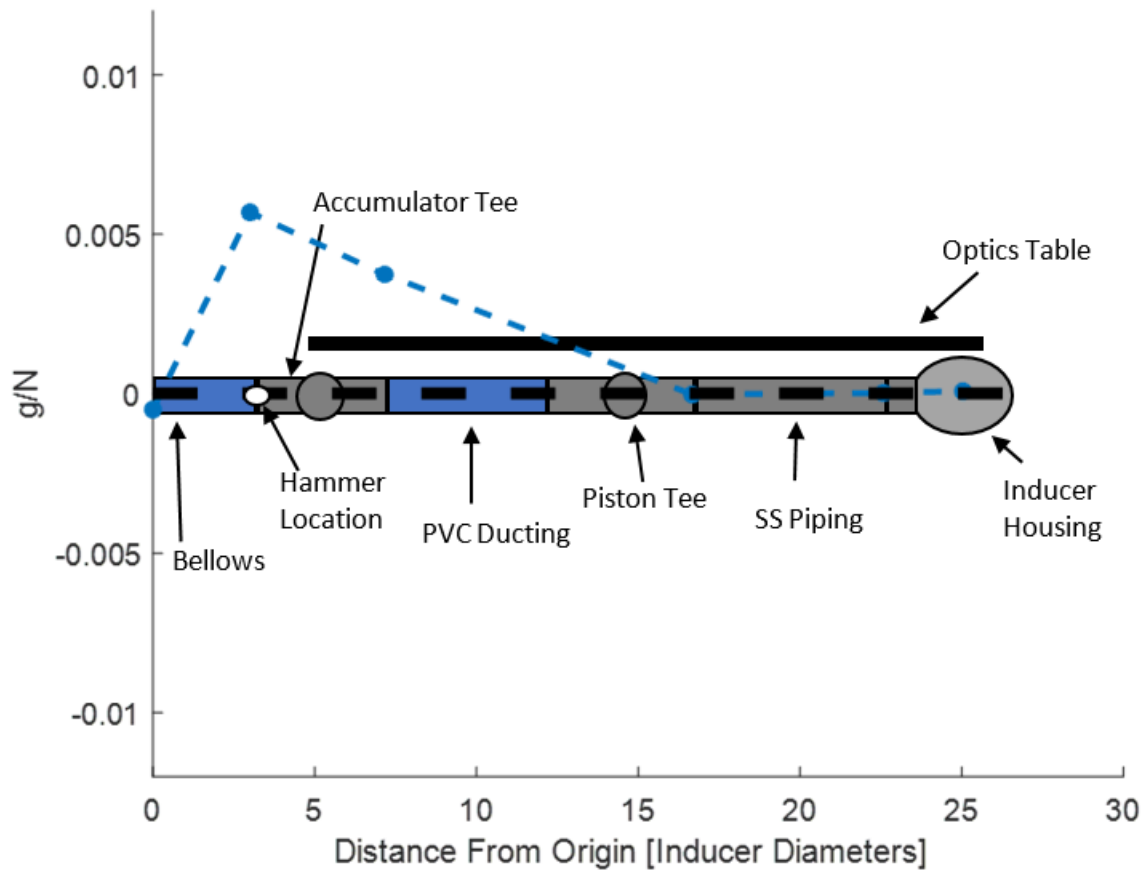


Figure E-6: Measured mode shape overlaid a cartoon of test facility indicated that the 0.56 rotor frequency mode is a result of the flexibility of the bellows and accumulator tee support structure

Bibliography

- [1] C. Brennen. *Hydrodynamics of Pumps*. Cambridge, 1994.
- [2] C. Brennen and A.J. Acosta. The dynamic transfer function of a cavitating inducer. *Journal of Fluids Engineering*, 1976.
- [3] C. Brennen, C. Meissner, E.Y. Lo, and G.S. Hoffman. Scale effects in the dynamic transfer functions of dynamic cavitating inducers. *Journal of Fluids Engineering*, 1982.
- [4] Langley Research Center. Prevention of coupled structure-propulsion instability (pogo). *NASA Special Publication*, pages 52+, October 1970.
- [5] D. A. Ehrlich and J. W. Murdock. A dimensionless scaling parameter for thermal effects on cavitation in turbopump inducers. *Journal of Fluids Engineering*, 2015.
- [6] D. A. Ehrlich, J. Schwille, R. P. Welle, J. W. Murdock, and B. S. Hardy. A water test facility for liquid rocket engine turbopump cavitation testing. *Proceedings of the 7th International Symposium on Cavitation (CAV2009)*, 2009.
- [7] H.P. Hackenberg and A. Hartung. An approach for estimating the effect of transient sweep through a resonance. *Journal of Engineering for Gas Turbines and Power*, 2016.
- [8] D. Jackson. Dynamics transfer function hydraulic pulser requirements internal aerospace corp presentation, 2017.
- [9] D. Jackson. Cavitation rig stability model internal aerospace corp presentation, 2018.
- [10] D. Jackson, J. Schwille, J. Gariffo, Z. Spakovszky, and V. Wang C. Lettieri. The influence of liquid rocket engine inducer compliance and mass flow gain factor on cavitation surge frequencies. *Proceedings of the 10th International Symposium on Cavitation (CAV2018)*, 2018.
- [11] O. Jia-Richards. A feasibility study of fiber-film probes for characterization of cavitation dynamics in a rocket engine turbopump inducer. Technical report, Massachusetts Institute of Technology, 2016.

- [12] C. Larsen. NASA experience with pogo in human spaceflight vehicles. *NATO RTO Symposium*, pages 23+, May 2008.
- [13] C. Lettieri, Z. Spakovszky, D. Jackson, and V. Wang. Characterization of cavitation instabilities in a four bladed turbopump inducer. *Journal of Propulsion and Power*, 2018.
- [14] A. Mulder. Nasa marshall internal documents (restricted).
- [15] S. Ng. *Dynamic Response of Cavitating Turbomachines*. PhD thesis, California Institute of Technology, 1980.
- [16] S. Rubin. Longitudinal instability of liquid rockets due to propulsion feedback (pogo). *Journal of Spacecraft and Rockets*, 1996.
- [17] S. Rubin. An interpretation of transfer function data for cavitating pump. *AIAA/ASME/SAE/ASEE Joint Propulsion Conference and Exhibit*, 2004.
- [18] Z. S. Spakovszky. *Applications of Axial and Radial Compressor Dynamic System Modeling*. PhD thesis, Massachusetts Institute of Technology, 2001.
- [19] Z. S. Spakovszky. A control theoretical approach to forced response system identification of rocket engine inducer cavitation dynamics, July 2016. Workshop, held at the Aerospace Corporaion, El Segundo, CA.
- [20] Y. Tsujimoto. Cavitation instabilities in inducer. *Design and Analysis of High Speed Pumps*, 2006.
- [21] Y. Tsujimoto, K. Kamijo, and C. Brennen. Dynamic model based identification of cavitation compliance and mass flow gain factor in rocket engine turbopump inducers. *Journal of Propulsion and Power*, 2001.
- [22] Y. Tsujimoto, K. Kamijo, and Y. Yoshida. Theoretical analysis of rotating cavitation in rocket pump inducers. *AIAA/ASME/SAE/ASEE Joint Propulsion Conference and Exhibit*, 1992.
- [23] Y. Wan, M. Manfredi, A. Pasini, and Z. S. Spakovszky. Dynamic model based identification of cavitation compliance and mass flow gain factor in rocket engine turbopump inducers. *ASME Turbo Expo Paper GT 2020-15655*, 2020.